Multi-order analytical solving computation of rainstorm causal decomposition during typhoons using a designed key–lock quasi-Newton optimizing derivation

Chien-Lin Huang, Nien-Sheng Hsu [*], Chun-Hao Yao, Wei-Chun Lo

Department of Civil Engineering, National Taiwan University, No. 1, Sec. 4, Roosevelt Road, Taipei, 10617, Taiwan

A R T I C L E   I N F O

A B S T R A C T

To precisely identify multi-dimensional spatiotemporal rain-making parameters, generate an approximate Hessian matrix, and solve the nonlinear ill-posed problem, this study uses composite logical tangent hyperbolic functions to construct the rain-generating simulation model as nonlinear algebraic equations with designed key–lock quasi-Newton optimization for deriving multi-order objective functional derivatives for rainstorm causal decomposition into advanced functional, analytical solution (lock) and Newton's conditional constraints. Specifically, the rank-two approximate structure of the Levenberg–Marquardt and Broyden–Fletcher–Goldfarb–Shanno quasi-Newton algorithms are modified as the symmetric rank-four structure to efficiently calculate a positive definite stable Hessian and solve the constrained nonlinear rain-making threshold. The model projects various rain-making factors into multi-rank loading scores, characterizing rain-generating mechanisms and causal components as associated DNAs. To accelerate/modify directional convergence, avoid local minimum, and detect global optimum, the devised vectorized limited switchable step sizes are optimized using advanced double-bracketing approaches combined with candidate parameters' correction vectors (key) and referenced step-size distributions solved by Newton's constrained analytical solution to reduce heterogeneous differences and eliminate the conventional overestimated Hessian. The identified rain-making DNAs reveal that typhoons with similar DNAs move in similar directions. Specifically, rain-making DNAs in Taipei Category 1 were correlated with wind force/direction and cloud height along PCs 1, 3, 4, and 7, and those in Category 2 were correlated with cloud-cover distribution along PCs 1, 2, and 5. The identified rain-making thresholds of typhoons with constant direction/structure showed a weaker steady state, whereas the unsteady rest produced multi-peak rainfall hydrographs. Rain evolution analysis reveals that cloudy rainbands, carried by the wind field, move along the Tamsui River valley when traveling between northeast and south-southeast of Taipei; converge with gradient and geostrophic winds when traveling between east-northeast and southwest; merge with southwest monsoon when traveling between west-southwest and northeast of Kaohsiung.

* Corresponding author.
E-mail addresses: d98521008@ntu.edu.tw (C.-L. Huang), nsshue@ntu.edu.tw, bruce7472@gmail.com (N.-S. Hsu), d98521027@ntu.edu.tw (C.-H. Yao), r00521314@ntu.edu.tw, weichunlo00314@gmail.com (W.-C. Lo).

1. Introduction

Typhoons and hurricanes are severe weather systems that bring rainstorms with strong destructive force. The processes of their formation, growth, and evolution are rather rapid. During a typhoon's strong winds and torrential rains invading the biosphere due to short early-warning time, high atmospheric evolutional uncertainty, and complex atmosphere-ocean–terrain exchange mechanisms, the conventional hydrometeorological numerical/statistical models for typhoon rainfall-flood forecasting have limitations on the simulated accuracy of invasion time and disastrous area, leading to losses of life, property, industry, commerce, and the biological environment. This can be attributed to the simulation of rainfall spatiotemporal patterns without thoroughly considering various types of atmospheric rain-making causes and rain-generating mechanisms. In addition, because of global warming and climate change, the intensity of wind or rainfall during typhoons has significantly increased in recent years [1–5]. In this context, the rainstorm invasive area must be identified through qualitative and quantitative analyses of the typhoon's rain-making causes to investigate the corresponding evolutionary degree. The analyzed results must be incorporated into simulation models to improve forecasting accuracy and extend the time for disastrous early warning.

Previous studies mainly focused on simulating typhoon moving track [6,7], wind field intensity [8–11], or storm surges [12–14]. However, these studies analyzed the interaction between the atmosphere and oceans to predict the evolving process of track, intensity, and surges, with less emphasis on the monsoon co-accompanying and terrain effect for further rainfall simulation. Due to the complex surface formations, the structure, intensity, and rainbands are primarily affected by topographic interactions following typhoon landfall; thus, the associated simulation ability for spatiotemporal changes is relatively reduced because the inter-evolutional mechanisms are less discussed. Previous methods for rainfall simulation during typhoons can generally be categorized into data-driven soft-computing approaches and atmospheric numerical simulations. Regarding data-driven approaches, Wei [15], Lin, Jhong [16], Yen, Liu [17], Wei [18], and Chen, Yeh [19] respectively applied an adaptive network-based fuzzy inference system with radar reflectivity, a multi-objective genetic algorithm with support vector machines, a deep echo state network, a radial basis function neural network with principal component analysis, and genetic programming combined with a multi-variable satellite dataset to predict typhoon precipitation. However, these methods' effective forecasted lead time is limited to 6 h, and the number of effective prediction stations is restricted.

Furthermore, regarding numerical methods, due to limitations of large-scale atmospheric, ocean, and terrain parametric/observational resolution, computing speed, and insufficient understanding of complex dynamic exchange mechanisms among different systems, accurate rainfall simulation have certain challenges [20]. Moreover, the following important findings have been obtained: (1) the structural distribution and transmission strength of a typhoon's cloudy rainband affects its moving speed and rainfall pattern [21]; (2) incorporating typhoon circulation and monsoon's co-accompanied effect into a simulation model can significantly improve the accuracy of rainfall forecast [22,23]; (3) when cloudy rainband reaches the windward side, torrential rains occur in the area due to the interaction between typhoon circulation and mountainous topography [24,25], with wind direction and speed being the major factors affecting rainfall pattern and intensity [26]; and (4) the spatiotemporal pattern of typhoon-induced heavy rain is dominated by moving track [27,28] and atmospheric environmental field [29]. Therefore, the success of typhoon rainfall modeling depends on whether diverse rain-making causal patterns are identified through spatiotemporal qualitative and quantitative analyses of various moving tracks. Subsequently, incorporating the information on high-resolution topography and cloud cover information can effectively improve torrential rainfall's predictability [30,31].

In the hydrological statistical data-driven soft-computing (machine learning), some previous studies have applied artificial neural networks as tools to predict typhoon rainfall [15–18]. However, very few studies have developed pure mathematical derivation skills for an advanced multi-order optimized analytical solution based on the governing equations of the model for theoretical or methodological research to describe and investigate rain-generating processes and evolutional mechanisms from atmospheric causes. Moreover, the selected optimizing algorithms for identifying multiple simulation parameters and optimization models largely affect prediction accuracy, computing performance, identified correctness, and occurrence of ill-posed problems. In machine-learning calculation, the logistic or tangent hyperbolic function is typically used descriptively because these functions fit well not only to the initial exponential rise and slow linear growth as saturation starts but also to eventual leveling off as the rainfall-generating environmental carrying capacity saturates. These logistic and tangent hyperbolic functions find applications in various fields, including ecology, biomathematics, chemistry, demography, geoscience, probability, and statistics. For instance, the logistic (hyperbolastic) function introduced by Pierre-Francois Verhulst has been devised as an exponential growth dynamic model in which the reproduced rate is proportional to the available resource capacity [32]. Subsequently, the equation was rediscovered for bacterial growth in broth and experimentally tested using a nonlinear parameterized estimation technique [33,34]. In addition, generalized logistic functions have been widely used to model COVID-19 infection trajectories [35]. Since environmental conditions affect rain-making carrying resource capacity, the causative model parameters are expected to vary over time.

Parameter identification is an important step in simulation–optimization, and nonlinear programming has often been used as a model optimization tool. Newton's method of nonlinear programming is a conventional identification algorithm that uses the initial predicted parameter sequence with the sensitivity coefficient (i.e., Jacobian) matrix to search for the root (optimal solution $\mathbf{\eta}^*$) of the first-order partial derivative of the objective function $J'(\mathbf{\eta}^*) = 0$. To improve the convergence speed of parameter identification, the Gauss–Newton method uses the second-order partial derivative composed of a square matrix of the objective function *versus* parameters (Hessian matrix) to describe the local curvature of parameter function and optimize parameters along a shorter and more direct path than Newton's method [36]. However, calculating the inverse of a high-dimensional Hessian matrix is an expensive operation, which can be solved using various decomposition or approximate iterative methods. Moreover, the number of simulations

and memory required to calculate the Hessian matrix equals the squared number of parameters, which is infeasible for high-dimensional functions with multiple parameters [37]. Furthermore, if the Hessian is similar to the irreversible matrix, the inverted Hessian may be numerically unstable, and the solution may diverge. Therefore, certain quasi-Newton algorithms that construct the variant structure of modified gradient for Hessian approximation have been developed, including the Jacobian quasi-Newton, Levenberg–Marquardt algorithm (LMA), and Broyden–Fletcher–Goldfarb–Shanno (BFGS) algorithm. However, the Jacobian quasi-Newton often overestimates the Hessian [37], which may not guarantee convergence and lead to an ill-posed problem; ultimately, the objective function reaches the minimum during optimization, but the identified parameter is not a correct solution. LMA adds a diagonal correction matrix that is more robust than the Jacobian quasi-Newton; however, the solution of LMA slowly converges to the global optimum only when the initial prediction is close to the global minimum [38]. The BFGS algorithm is only suitable for solving unconstrained optimization problems, and unless the function assumes quadratic Taylor expansion characteristics near the optimal position, Newton's method and BFGS algorithm cannot guarantee convergence [37,39]. The primary reasons for the above shortcomings are the scalar nature of the step size of the Jacobian quasi-Newton, Marquardt damping factor of LMA, and the secant scale factor of the BFGS algorithm. Furthermore, the conventional quasi-Newtons minimize the objective function $J = f(\boldsymbol{\eta}^k + \alpha^k \cdot \mathbf{d}^k)$ through the scalar step size $\alpha^k > 0$. The search process first calculates the gradient descent direction $\mathbf{d}^k$ of J to optimize how far the parameter vector $\boldsymbol{\eta}^k$ should move along this direction, thereby ensuring convergence [40]. If the selected computer program must repeatedly calculate the governing equations during optimization, time-saving advanced solving approaches for shrinking the step size interval are key to effective optimization. If the scalar step size is extended to the vector, the direction can be modified to approximate the Hessian better.

The inverse problem includes ill-posed and well-posed. The difference is that ill-posed does not have a stable unique solution and does not satisfy that the solution continuously depends on the definite condition. The reason for this is the inverse problem in large-scale three-dimensional earth science problems; the number of observations is often less than that of identified parameters, causing the inverse problem is ill-posed. The solution is to constrain it with equations that conform to the laws and properties of geophysics, making it well-posed so that a correct and stable unique solution can be obtained. Most of the previously developed heuristic algorithms optimized variables/parameters based on the mathematical approximation method, and the constraints that rarely considered sufficient physical conservation equations were insufficient. Hence, the purpose of this study is to use devised composite logical tangent hyperbolic functions as advanced nonlinear algebraic equations to construct a typhoon rain-generating simulation model, combined with a designed key–lock quasi-Newton approach to derive the analytical solution (lock) of the Hessian matrix, multi-order objective/mock functional derivatives and physical-based Newton's conditional constraints for effectively identifying the causal rain-making quantity. Subsequently, we use vectorized limited switchable step size with the derived multi-order analytical solution to solve the rain-making spatiotemporal thresholds of various atmospheric factors and quantify the corresponding produced precipitation. The analytical derivation solved a few candidate solutions (keys) and referenced step size distribution to establish advanced functional multi-order exact double-bracketing approaches for vectorized step-size optimization configured with various parameters. The considered diverse rain-making variables for causal identification include (1) multi-layer cloudy cover/height; (2) monsoon co-accompanied effect; (3) terrain uplift effect; and (4) ceiling height, among others. In addition, this study specifically (1) identifies the rain-making DNAs of various typhoons and (2) uses fuzzy c-means clustering to characterize the spatiotemporal correlation structures of the identified rain-making causal compositions, moving paths, wind field structures, and cloudy rainbands.

2. Material and methodology

2.1. Overview

This study uses composite logical tangent hyperbolic functions to construct the rain-generating simulation model during typhoons as advanced swarm nonlinear algebraic equations (described in section 2.5.1) with a designed key–lock quasi-Newton optimizing approach to (1) derive an advanced functional, analytical solution (lock) of the Hessian matrix and Newton's conditional constraints of rainstorm causal decomposition (described in section 2.5.2); (2) solve the candidate solutions and referenced step size distribution satisfying Newton's conditions using multi-order key–lock quasi-Newton analytical derivation, and (3) identify spatiotemporal rain-making threshold parameters configured with various typhoon atmospheric rain-making variables and the corresponding induced precipitation associated with vectorized limited switchable step size optimized using the proposed derivative-functionalized precise double-bracketing approach (described in section 2.6). Section 2.3 describes the established optimization model for rain-generating threshold identification, and section 2.4 discusses solving problems of traditional quasi-Newtons. Section 2.7 states the classification principle of rainfall spatiotemporal causal characteristics using singular-value decomposed multi-rank loading scores under dimensionality reduction. Section 2.2 describes the research steps of the developed symmetric rank-four analytical key-lock quasi-Newton.

2.2. Procedures

This work comprises four parts: (1) derivation of the calculation mode of conventional quasi-Newton algorithms for solving the rain-making parameter optimization model; (2) establishment of the typhoon rain-generating simulation model and derivation of the analytical solution of the Hessian matrix and Newton's conditional constraints; (3) calculation of parameter correction direction and optimization of vectorized step size using the key–lock quasi-Newton; and (4) estimation of rainfall multi-rank loading scores to
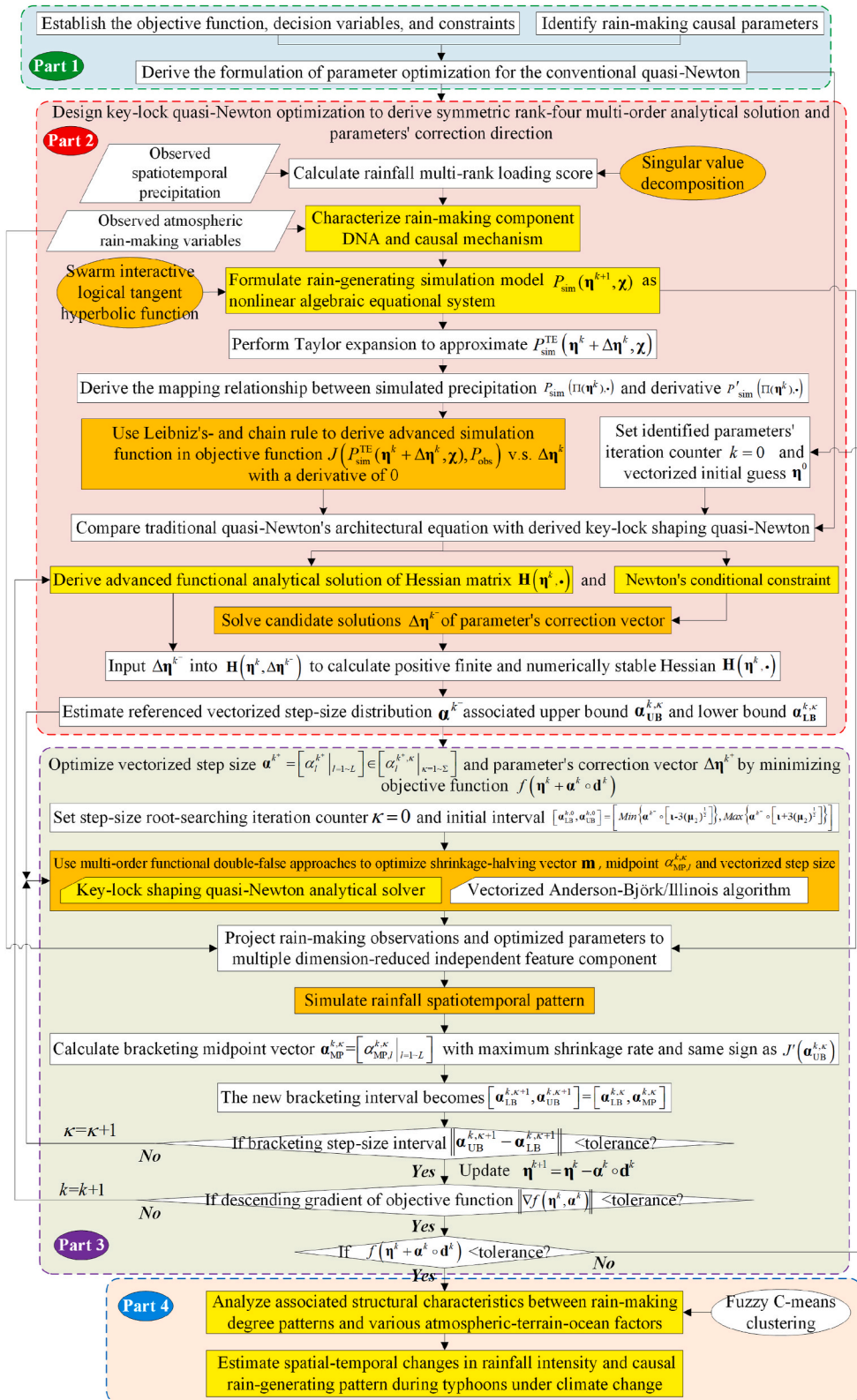
Fig. 1. Flowchart of the methodology.

analyze the spatiotemporal causal characteristic patterns associated with rain-making factors. The flowchart is shown in Fig. 1, and the steps are described below.

Step 1-1. Establish the objective function and constraints of the optimization model for identifying rain-making causal parameters.

Step 1–2. Derive the formulation of parameter optimization for the conventional quasi-Newton.

Step 2. Use the designed key–lock quasi-Newton optimization to derive a symmetric rank-four multi-order derivative analytical solution of the objective function for estimating the parameter's correction direction

$$\mathbf{d}^k = \left\{ \begin{array}{l} \left[(\mathbf{B}-\mathbf{b}) \cdot \left[\frac{\Gamma^{-1}}{w}\right]^{\mathrm{T}} \circ (\mu_2)^{\frac{1}{2}} + \mu_1 \right]_{\mathrm{Lx1}}^{\mathrm{T}} \cdot 2\left[\mathbf{r}^k+\kappa^k\right]^{\mathrm{T}} \cdot N^{-1} \left(\mathbf{a}e_{\mathrm{Mx\Gamma}}^{\theta\gamma^k\Pi(\chi)} \cdot \left[\frac{\iota}{\iota+\alpha e^{-\mathbf{B}\Pi(\chi)}}\right]^{\mathrm{T}} \cdot \left[\frac{\alpha e^{-\mathbf{B}\Pi(\chi)}}{\iota+\alpha e^{-\mathbf{B}\Pi(\chi)}}\right] \cdot \left[(\mu_2)^{\frac{-1}{2}} \cdot \mathbf{w}\right]_{\Gamma \mathrm{x1}}^{\mathrm{T}} \right) \cdot \left[\frac{L^{-1}}{\Delta\eta^k}\right]_{\mathrm{1xL}}^{\mathrm{T}} \cup \\ \left[(\mathbf{B}-\mathbf{b})\left[\frac{\Gamma^{-1}}{w}\right]^{\mathrm{T}} \circ (\mu_2)^{\frac{1}{2}} + \mu_1 \right]_{\mathrm{Lx1}}^{\mathrm{T}} \cdot 2\left[\mathbf{r}^k+\kappa^k\right]^{\mathrm{T}} \cdot N^{-1} \left(\mathbf{a}e_{\mathrm{Mx\Gamma}}^{\theta\gamma^k\Pi(\chi)} \cdot \left(\iota - \left[\frac{e^{\mathbf{B}\Pi(\chi)}-e^{-\mathbf{B}\Pi(\chi)}}{e^{\mathbf{B}\Pi(\chi)}+e^{-\mathbf{B}\Pi(\chi)}}\right]^{\mathrm{T}} \left[\frac{e^{\mathbf{B}\Pi(\chi)}-e^{-\mathbf{B}\Pi(\chi)}}{e^{\mathbf{B}\Pi(\chi)}+e^{-\mathbf{B}\Pi(\chi)}}\right] \right) \cdot \left[(\mu_2)^{\frac{-1}{2}} \cdot \mathbf{w}\right]_{\Gamma \mathrm{x1}}^{\mathrm{T}} \right) \cdot \left[\frac{L^{-1}}{\Delta\eta^k}\right]_{\mathrm{1xL}}^{\mathrm{T}} \end{array} \right\}^{-1}$$
$$\cdot \left(\mathbf{J}_{\mathrm{D}}^{\mathrm{T}}\right)^k \cdot \mathbf{r}(\eta^k)$$

(described in section 2.5).

Step 2–1. Calculate rainfall-observed multi-rank loading scores using singular-value decomposition to characterize the rain-making causal component/mechanism.

Step 2-2. Formulate the rain-generating simulation model $P_{\mathrm{sim}}(\eta^{k+1}, \chi)$ comprising swarm interactive logical tangent hyperbolic function as a nonlinear algebraic system, and subsequently perform Taylor expansion to approximate $P_{\mathrm{sim}}^{\mathrm{TE}}(\eta^k + \Delta\eta^k, \chi)$.

Step 2–3. Derive the relationship between simulated precipitation $P_{\mathrm{sim}}(\Pi(\eta^k), \cdot)$ and its derivative $P_{\mathrm{sim}}^{'}$.

Step 2–4. Use Leibniz's and chain rule to derive the advanced simulation function embedded in the objective function $J(P_{\mathrm{sim}}^{\mathrm{TE}}(\eta^k + \Delta\eta^k, \chi), P_{\mathrm{obs}})$ *versus* $\Delta\eta^k$ with a derivative of 0.

Step 2–5. Compare architectural equation (3a) of the conventional quasi-Newton with the derived equation (22) of the key–lock quasi-Newton to obtain the advanced functional algebraic analytical solution of Hessian matrix $\mathbf{H}(\eta^k, \bullet)$ (lock) and Newton's constraints, as expressed in equations (23)- (24). Subsequently, efficiently solve a few candidate solutions $\Delta\eta^{k^-}$ (key) of parameter correction vectors and input $\Delta\eta^{k^-}$ into $\mathbf{H}(\eta^k, \Delta\eta^{k^-})$ to calculate a positive finite and numerically stable Hessian.

step 2–6. Input $\Delta\eta^{k^-}$ and $\mathbf{H}(\eta^k, \bullet)$ into equation (31) to estimate the referenced vectorized step size α^{k^-} distribution and the corresponding lower/upper bound $[\alpha_{\mathrm{LB}}^{k,\kappa}, \alpha_{\mathrm{UB}}^{k,\kappa}]$, which meet Newton's conditions.

step 3. Optimize the vectorized step size $\alpha^{k^+} \in \left[a_l^{k^+,\kappa} \left| \begin{array}{l} l = 1 \sim L \\ \kappa = 1 \sim \Sigma \end{array} \right. \right]$ by minimizing $J(\eta^k + \alpha^k \circ \mathbf{d}^k)$ (described in section 2.6), and calculate the optimal correction vector $\Delta\eta^{k^+}$ using equation (31).

step 3–1. Set the initial interval for the step size $[\alpha_{\mathrm{LB}}^{k,0}, \alpha_{\mathrm{UB}}^{k,0}] = \left[Min\left\{\alpha^{k^-} \circ \left[\iota - 3(\mu_2)^{\frac{1}{2}}\right]\right\}, Max\left\{\alpha^{k^-} \circ \left[\iota + 3(\mu_2)^{\frac{1}{2}}\right]\right\} \right]$.

step 3–2. Use the multi-order derivative functional precise double-position bracketing approach, i.e., the key–lock quasi-Newton-derived reference step size distribution α^{k^-} with vectorized Anderson–Björk/Illinois algorithm to optimize the shrinking vector and step size.

Step 3-3. Project 11 types of atmospheric rain-making causal observations and optimized parameters to multiple characterized categories, combined with the swarm composite rain-generating function to simulate the rainfall spatiotemporal pattern.

step 3–4. Calculate the bracketing midpoint step-size vector $\alpha_{\mathrm{MP}}^{k,\kappa} = [\alpha_{\mathrm{MP},l}^{k,\kappa}]$ with the maximum shrinkage rate and the same sign as $J^{'}(\alpha_{\mathrm{UB}}^{k,\kappa})$. Then, the new bracketing interval becomes $[\alpha_{\mathrm{LB}}^{k,\kappa+1}, \alpha_{\mathrm{UB}}^{k,\kappa+1}] = [\alpha_{\mathrm{LB}}^{k,\kappa}, \alpha_{\mathrm{MP}}^{k,\kappa}]$. Let $\kappa = \kappa + 1$ and return to steps 3–2 until the bracketing interval $\left\| \alpha_{\mathrm{UB}}^{k,\kappa+1} - \alpha_{\mathrm{LB}}^{k,\kappa+1} \right\| <$ tolerance.

Step 3–5. Update $\eta^{k+1} = \eta^k - \alpha^k \circ \mathbf{d}^k$. Set $k = k + 1$ or parameter's initial prediction η^0 and return to steps 2–5 until the descending gradient of the objective function $\left\| \nabla f(\eta^k, \alpha^k) \right\|$ and $f(\eta^k + \alpha^k \circ \mathbf{d}^k) <$ tolerance.

Step 4. Analyze the associated structural characteristics between rainfall patterns and various atmospheric–terrain–ocean factors using fuzzy c-means clustering. Estimate the spatiotemporal changes in rainfall intensity and the causal rain–generating patterns during typhoons.

2.3. Establishment of an optimization model for identifying typhoon's rain-generating parameters

2.3.1. Objective function

Conventional methods use a limited number of observations to optimize the spatiotemporal pattern of the parameter vector η. Considering that the sensitivity order of the major controlling factors affecting the magnitude of a typhoon's rainfall differs largely, this

study uses the least-squares error (LSE) of the simulated and observed precipitation hyetographs ($P_{ts,s}^{sim}$ and $P_{ts,s}^{obs}$, respectively) as the objective function, as shown in equation (1), combined with the designed composite advanced rainfall simulation functions to
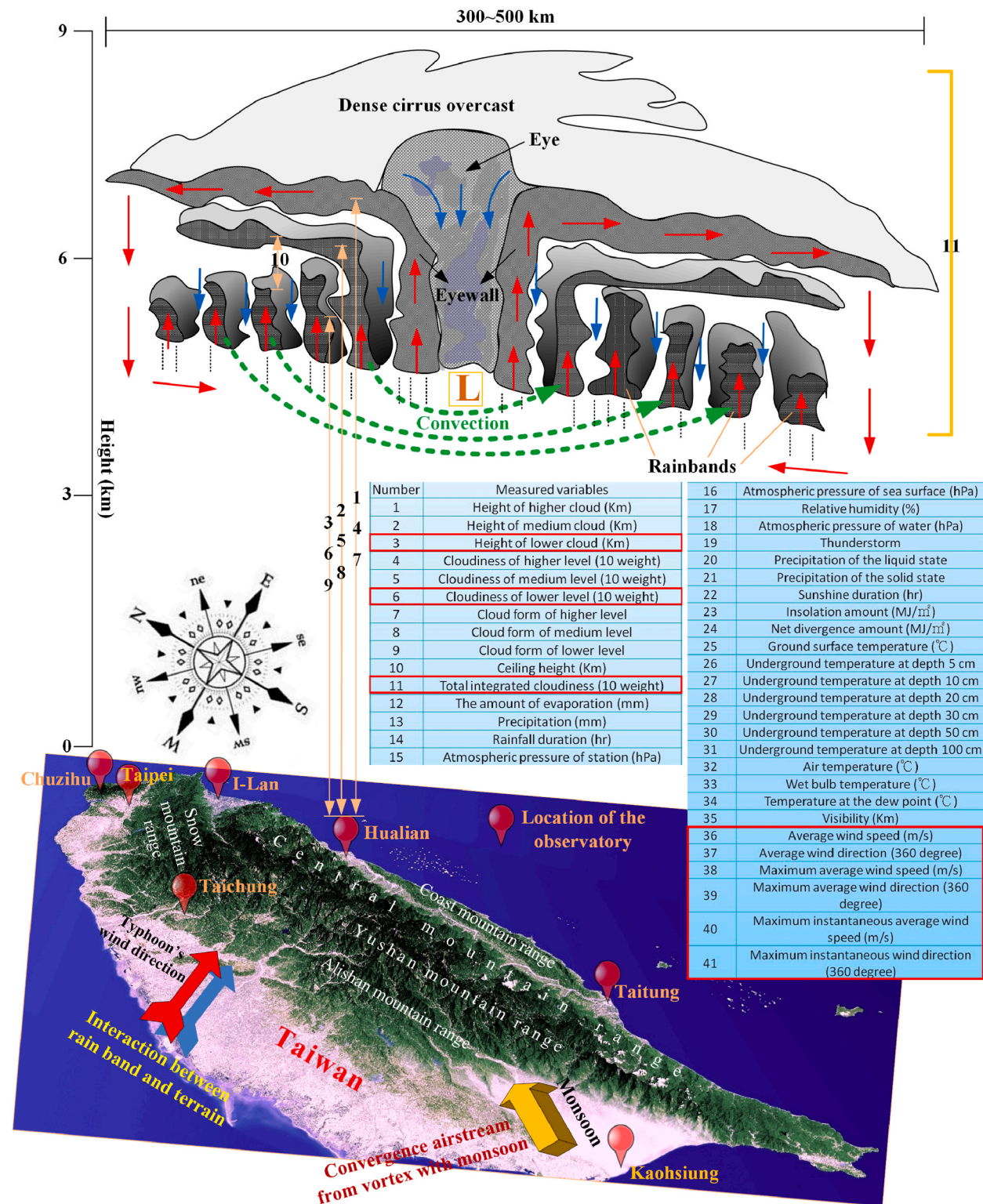

Fig. 2. Schematic diagram of typhoon's atmospheric rain-making variables, as measured by the Central Weather Bureau Observatory in Taiwan.

optimize the rain-generating threshold parameter $\boldsymbol{\eta}$ of various atmospheric rain-making factors.

$$
\begin{aligned}
\underset{\boldsymbol{\eta}}{Minimize} \quad J(\boldsymbol{\eta}) &= \left[P_{t,s}^{\text{sim}}(\boldsymbol{\eta}) - P_{t,s}^{\text{obs}} \right]^{\text{T}} \left[P_{t,s}^{\text{sim}}(\boldsymbol{\eta}) - P_{t,s}^{\text{obs}} \right] = \\
&= \sum_{s=1}^{S} \sum_{t=1}^{T} \left(P_{t,s}^{\text{sim}}(\boldsymbol{\eta}) - P_{t,s}^{\text{obs}} \right)^2 = \sum_{m=1}^{M} \left(\vartheta_m^{\text{sim}}(\boldsymbol{\eta}^k) - \vartheta_m^{\text{obs}} \right)^2 = \sum_{m=1}^{M} r_m^2(\boldsymbol{\eta}^k)
\end{aligned}
\tag{1}
$$

where $P_{t,s}^{\text{sim}}(\boldsymbol{\eta})$ is the simulated precipitation and $P_{t,s}^{\text{obs}}$ is the observed precipitation at the observation station s and time t according to the identified rain-generating threshold $\boldsymbol{\eta}$. Equation (1) assumes that the atmospheric system has S number of surface observation stations and multiple rainfall time intervals (duration) T, which $M = T \times S$.

2.3.2. Decision variables and constraints for rain-making causal optimization

The rain-making factorial decision variables measured by weather stations of the Central Weather Bureau of Taiwan are presented in Fig. 2, in which various spatiotemporal patterns were extracted from the Data Bank for Atmospheric & Hydrologic Research (https://dbar.pccu.edu.tw/). The considered candidate typhoon's atmospheric rain-making factors include (1) the low-layer cloud height (**LCH**) $h_{t,s}^{\text{LC}}$, (2) ceiling height (**CH**) $h_{t,s}^{\text{CCei}}$, (3) low/total cloudy cover (**LCC** $\varphi_{t,s}^{\text{LCC}}$/**TCC** $\varphi_{t,s}^{\text{TCC}}$), (4) atmospheric pressure (AP) $\rho_{t,s}^{\text{AP}}$, (5) monsoon co-accompanied effect, (6) topographic uplift effect, and (7) wind accelerator. The occurrence of monsoon convergent co-accompanied effect depends on the consistency between the typhoon's maximum/average wind direction $\theta_{t,s}^{\text{MAWD}}$ and the monsoon's wind direction $\varphi_{t,s}^{\text{mon}}$; as such, in an area suffering the greater maximum/average wind speed $\nu_{t,s}^{\text{MAWS}}$ above a certain threshold, a more vigorous cloudy rainband is introduced by the co-accompanied effect [41–43]. When the average wind direction $\theta_{t,s}^{\text{AWD}}$ is facing the vertical direction of the mountainous windward slope $\varphi_{t,s}^{\text{ter}}$, the transported cloudy rainband induces heavy rains on the observatory in the windward area, and the stronger average wind speed $\nu_{t,s}^{\text{AWS}}$ introduces more rainbands due to the terrain uplift effect [20,44,45]. Moreover, the stronger maximum/instantaneous wind speed $\nu_{t,s}^{\text{MIWS}}$ and the closer maximum/instantaneous wind direction $\theta_{t,s}^{\text{MIWD}}$ to the windward slope vertical direction $\varphi_{t,s}^{\text{ter}}$ or monsoon direction $\varphi_{t,s}^{\text{mon}}$ bring a stronger driving force at the cloudy rainband transmitted by the increased gradient of wind speed [45,46].

Next, according to the typhoon's windy–cloudy structure, we set the identified rain-generating threshold parameter vector $\boldsymbol{\eta} = [\boldsymbol{\Pi}^{\text{AP}}, \mathbf{V}^{\text{AWS}}, \boldsymbol{\Theta}^{\text{AWD}}, \mathbf{V}^{\text{MAWS}}, \boldsymbol{\Theta}^{\text{MAWD}}, \mathbf{V}^{\text{MIWS}}, \boldsymbol{\Theta}^{\text{MIWD}}, \mathbf{H}^{\text{LC}}, \boldsymbol{\Phi}^{\text{LCC}}, \mathbf{H}^{\text{CCei}}, \boldsymbol{\Phi}^{\text{TCC}}]$, including measured air pressure (hPa) $\boldsymbol{\Pi}^{\text{AP}} = \left\{ \rho_{t,s}^{\text{AP}} \middle| \begin{matrix} t = 1, ..., T \\ s = 1, ..., S \end{matrix} \right\}$, average wind speed (m/s) $\mathbf{V}^{\text{AWS}} = \left\{ \nu_{t,s}^{\text{AWS}} \middle| \begin{matrix} t = 1, ..., T \\ s = 1, ..., S \end{matrix} \right\}$, the angle between average wind direction and mountainous vertical direction $\boldsymbol{\Theta}^{\text{AWD-ter}} = \left\{ \left| \theta_{t,s}^{\text{AWD}} - \varphi_{t,s}^{\text{ter}} \right| \middle| \begin{matrix} t = 1, ..., T \\ s = 1, ..., S \end{matrix} \right\}$, maximum average wind speed $\mathbf{V}^{\text{MAWS}} = \{\nu_{t,s}^{\text{MAWS}}\}$, angle between the maximum average wind direction and monsoon direction $\boldsymbol{\Theta}^{\text{MAWD-mon}} = \{|\theta_{t,s}^{\text{MAWD}} - \varphi_{t,s}^{\text{mon}}|\}$, maximum instantaneous wind speed $\mathbf{V}^{\text{MIWS}} = \{\nu_{t,s}^{\text{MIWS}}\}$, angle between the maximum instantaneous wind direction and monsoon/mountainous direction $\boldsymbol{\Theta}^{\text{MIWD}} = \left\{ \left| \theta_{t,s}^{\text{MIWD}} - \left(\frac{\omega \cdot \varphi_{t,s}^{\text{mon}} + \varpi \cdot \varphi_{t,s}^{\text{ter}}}{\omega + \varpi} \right) \right| \right\}$, low-layer cloud height (Km) $\mathbf{H}^{\text{LC}} = \{h_{t,s}^{\text{LC}}\}$, low-layer cloud cover (10 components) $\boldsymbol{\Phi}^{\text{LCC}} = \{\varphi_{t,s}^{\text{LCC}}\}$, ceiling height (Km) $\mathbf{H}^{\text{CCei}} = \{h_{t,s}^{\text{CCei}}\}$, and total cloud cover (10 components) $\boldsymbol{\Phi}^{\text{TCC}} = \{\varphi_{t,s}^{\text{TCC}}\}$, totaling 11 parameters (=N). The vector $\boldsymbol{\eta}$ contains $L = T \times S \times N$ number of parameters.

This optimization model contains the following constraints: (1) the spatiotemporal distribution of the water cycle between the typhoon's rainbands, absorbed seawater, and rainfall should follow the conservation of mass and energy; and (2) the upper and lower bounds of cloudy structural and the wind-related rain-making threshold (e.g., cloud height/cover, ceiling height, wind speed, wind directional convergence angles) should conform to the on-site atmospheric–hydrological–topographic conditions. Typically, identifying spatiotemporally distributed causal rain-making parameters under interdisciplinary exchange is a large-scale and highly nonlinear optimization problem.

2.4. Difficulties and problems of nonlinear simulation–optimization solving

In nonlinear programming, Newton's method attempts to find the root of J' from the initial prediction $\boldsymbol{\eta}^0$ by constructing a sequence $\boldsymbol{\eta}^k$, which converges to a certain parameter value $\boldsymbol{\eta}^*$ under the condition that $J'(\boldsymbol{\eta}^*) = 0$. Here, $\boldsymbol{\eta}^*$ is the stationary point of J, where the second-order Taylor expansion $J_{\text{T}}(\boldsymbol{\eta}^*)$ of the objective function J around $\boldsymbol{\eta}^k$ is shown in equation (2):

$$
J_{\text{T}}(\boldsymbol{\eta}^{k+1}) = J_{\text{T}}(\boldsymbol{\eta}^k + \Delta\boldsymbol{\eta}^k) \approx J(\boldsymbol{\eta}^k) + J'(\boldsymbol{\eta}^k)^{\text{T}} \cdot \Delta\boldsymbol{\eta}^k + \frac{1}{2}(\Delta\boldsymbol{\eta}^k)^{\text{T}} J''(\boldsymbol{\eta}^k) \cdot \Delta\boldsymbol{\eta}^k + \text{HOT}
\tag{2}
$$

Ideally, $\Delta\boldsymbol{\eta}^k$ should be optimized such that $\boldsymbol{\eta}^k + \Delta\boldsymbol{\eta}^k$ is the stationary point of J. Then, using this Taylor expansion as an approximation, the root of the expanded derivative corresponding to $\Delta\boldsymbol{\eta}^k$ can be solved as follows:

$$0 = \frac{d}{d\Delta\boldsymbol{\eta}^k}\left(J(\boldsymbol{\eta}^k) + J'(\boldsymbol{\eta}^k)^{\mathrm{T}} \cdot \Delta\boldsymbol{\eta}^k + \frac{1}{2}(\Delta\boldsymbol{\eta}^k)^{\mathrm{T}} J''(\boldsymbol{\eta}^k) \cdot \Delta\boldsymbol{\eta}^k\right) = J'(\boldsymbol{\eta}^k) + J''(\boldsymbol{\eta}^k) \cdot \Delta\boldsymbol{\eta}^k \tag{3a}$$

$$\Rightarrow \Delta\boldsymbol{\eta}^k = -\left[J''(\boldsymbol{\eta}^k)\right]^{-1} J'(\boldsymbol{\eta}^k) \tag{3b}$$

By replacing $J'(\boldsymbol{\eta}^k)$ with the gradient $\nabla J(\boldsymbol{\eta}^k)$ and the reciprocal of the second-order derivative $[J''(\boldsymbol{\eta}^k)]^{-1}$ with the inverse of the Hessian matrix $\mathbf{H}^{-1}(\boldsymbol{\eta}^k)$, the above iterative method can be derived to multiple parameter dimensions, as shown in equation (4):

$$\boldsymbol{\eta}^{k+1} = \boldsymbol{\eta}^k - \mathbf{H}^{-1}(\boldsymbol{\eta}^k)\nabla J(\boldsymbol{\eta}^k), k \in \mathbb{N} \tag{4}$$

If all second-order partial derivatives of J are present and are continuous in the functional domain, the Hessian matrix $\mathbf{H}$ can be defined in equation (5):

$$\mathbf{H}(\boldsymbol{\eta}^k) = \begin{bmatrix} \frac{\partial^2 J}{\partial\eta_1^2} & \frac{\partial^2 J}{\partial\eta_1\partial\eta_2} & \cdots & \frac{\partial^2 J}{\partial\eta_1\partial\eta_L} \\ \frac{\partial^2 J}{\partial\eta_2\partial\eta_1} & \frac{\partial^2 J}{\partial\eta_2^2} & \cdots & \frac{\partial^2 J}{\partial\eta_2\partial\eta_L} \\ \vdots & \vdots & \ddots & \vdots \\ \frac{\partial^2 J}{\partial\eta_L\partial\eta_1} & \frac{\partial^2 J}{\partial\eta_L\partial\eta_2} & \cdots & \frac{\partial^2 J}{\partial\eta_L^2} \end{bmatrix} \tag{5}$$

At the local minimum of J, the Hessian matrix is positive and semi-definite. Each iteration of the Gauss–Newton method, $J_{\mathrm{T}}(\boldsymbol{\eta}^k)$, is approximated by a quadratic function around $\boldsymbol{\eta}^k$ using the scalar step size $\alpha \in (0, 1)$ to move toward the functional minimal value, as shown in equation (6). The Jacobian quasi-Newton uses the Jacobian matrix $\mathbf{J}_{\mathrm{D}}$ to iteratively approximate the Hessian matrix $\mathbf{H} \approx 2\mathbf{J}_{\mathrm{D}}^{\mathrm{T}}\mathbf{J}_{\mathrm{D}}$, as shown in equation (6). LMA adds an identity matrix $\mathbf{I}$ to the Hessian matrix $\mathbf{H} \approx \mathbf{J}_{\mathrm{D}}^{\mathrm{T}}\mathbf{J}_{\mathrm{D}} + \lambda\mathbf{I}$ and adjusts the scale ratio between iterations such that the incremental vector rotates toward the steepest slope, as shown in equation (6). Fletcher (1971) scaled gradient components according to the curvature (i.e., replaced the identity matrix with the diagonal matrix $\mathbf{J}_{\mathrm{D}}^{\mathrm{T}}\mathbf{J}_{\mathrm{D}}$), which can avoid the slow convergence of small gradient direction, increase larger movement [37], and reduce the adverse effects of larger damping factor λ to solve the ill-posed problems, as shown in equation (6). The BFGS algorithm sets the searching direction $\mathbf{d}^k = -\mathbf{H}^{-1}(\boldsymbol{\eta}^k)\nabla J(\boldsymbol{\eta}^k) \approx -\mathbf{A}^{-1}(\boldsymbol{\eta}^k)\nabla J(\boldsymbol{\eta}^k)$ using the simulation solution of Newton's equation to the unconstrained optimization problem, where $\mathbf{A}(\boldsymbol{\eta}^k)$ is the approximate Hessian matrix, as shown in equation (6).

$$\begin{cases} \text{Gauss} - \text{Newton}: \boldsymbol{\eta}^{k+1} = \boldsymbol{\eta}^k - \alpha^k\left[\mathbf{H}(\boldsymbol{\eta}^k)J(\boldsymbol{\eta}^k)\right]^{-1}\nabla J(\boldsymbol{\eta}^k), k \in \mathbb{N} \\[6pt] \text{Jacobian quasi} - \text{Newton}: \boldsymbol{\eta}^{k+1} = \boldsymbol{\eta}^k - \alpha^k\left[2\mathbf{J}_{\mathrm{D}}^{\mathrm{T}}\mathbf{J}_{\mathrm{D}}\right]^{-1}\mathbf{J}_{\mathrm{D}}^{\mathrm{T}}\mathbf{r}(\boldsymbol{\eta}^k), k \in \mathbb{N} \\[6pt] \mathbf{J}_{\mathrm{D}}^{\mathrm{T}}(\boldsymbol{\eta}^k) = \begin{bmatrix} \frac{\partial\vartheta_1^{\mathrm{sim}}}{\partial\eta_1} & \frac{\partial\vartheta_2^{\mathrm{sim}}}{\partial\eta_1} & \cdots & \frac{\partial\vartheta_m^{\mathrm{sim}}}{\partial\eta_1} & \cdots & \frac{\partial\vartheta_M^{\mathrm{sim}}}{\partial\eta_1} \\ \vdots & \vdots & & \vdots & & \vdots \\ \frac{\partial\vartheta_1^{\mathrm{sim}}}{\partial\eta_L} & \frac{\partial\vartheta_2^{\mathrm{sim}}}{\partial\eta_L} & \cdots & \frac{\partial\vartheta_m^{\mathrm{sim}}}{\partial\eta_L} & \cdots & \frac{\partial\vartheta_M^{\mathrm{sim}}}{\partial\eta_L} \end{bmatrix}_{L\times M} \\[6pt] \text{Levenberg} - \text{Marquardt} \\[4pt] \text{algorithm}: \boldsymbol{\eta}^{k+1} = \boldsymbol{\eta}^k - \left[\mathbf{J}_{\mathrm{D}}^{\mathrm{T}}\mathbf{J}_{\mathrm{D}} + \lambda\mathbf{I}\right]^{-1}\mathbf{J}_{\mathrm{D}}^{\mathrm{T}}\mathbf{r}(\boldsymbol{\eta}^k), k \in \mathbb{N} \\[6pt] \text{Fletcher} - \text{modified LMA}: \boldsymbol{\eta}^{k+1} = \boldsymbol{\eta}^k - \left[\mathbf{J}_{\mathrm{D}}^{\mathrm{T}}\mathbf{J}_{\mathrm{D}} + \lambda\mathrm{diag}(\mathbf{J}_{\mathrm{D}}^{\mathrm{T}}\mathbf{J}_{\mathrm{D}})\right]^{-1}\mathbf{J}_{\mathrm{D}}^{\mathrm{T}}\mathbf{r}(\boldsymbol{\eta}^k), k \in \mathbb{N} \\[6pt] \text{BFGS quasi} - \text{Newton}: \boldsymbol{\eta}^k = \boldsymbol{\eta}^{k-1} + \mathbf{A}^{-1}(\boldsymbol{\eta}^k) \cdot \left[\nabla J(\boldsymbol{\eta}^k) - \nabla J(\boldsymbol{\eta}^{k-1})\right] \\[6pt] \mathbf{A}(\boldsymbol{\eta}^k) = \mathbf{A}(\boldsymbol{\eta}^{k-1}) + \chi^k\boldsymbol{\mu}^{k-1}(\boldsymbol{\mu}^{k-1})^{\mathrm{T}} + \gamma^k\boldsymbol{\nu}^{k-1}(\boldsymbol{\nu}^{k-1})^{\mathrm{T}} \\[6pt] \chi^k = \frac{1}{(\mathbf{y}^{k-1})^{\mathrm{T}}\mathbf{s}^{k-1}}, \gamma^k = -\frac{1}{(\mathbf{s}^{k-1})^{\mathrm{T}} \cdot \mathbf{A}(\boldsymbol{\eta}^{k-1}) \cdot \mathbf{s}^{k-1}}, \mathbf{y}^{k-1} = \nabla J(\boldsymbol{\eta}^k) - \nabla J(\boldsymbol{\eta}^{k-1}), \mathbf{s}^{k-1} = \boldsymbol{\eta}^k - \boldsymbol{\eta}^{k-1} \end{cases} \tag{6}$$

here $\mathbf{J}_{\mathrm{D}}^{\mathrm{T}}(\boldsymbol{\eta}^k)$ is the Jacobian sensitivity coefficient matrix of $\vartheta_m^{\mathrm{sim}}$, as defined in equation (6). In the BFGS algorithm, the Hessian approximate matrix $\mathbf{A}(\boldsymbol{\eta}^k)$ must conform to symmetry and positive definiteness, in which $\chi^k\boldsymbol{\mu}^{k-1}(\boldsymbol{\mu}^{k-1})^{\mathrm{T}}$ and $\gamma^k\boldsymbol{\nu}^{k-1}(\boldsymbol{\nu}^{k-1})^{\mathrm{T}}$ are both symmetric rank-one matrices and their sum is a rank-two updated matrix.

The simulation time of a large-scale typhoon's rain-generating model significantly increases as the number of atmospheric–hydrogeographic parameters and controlled volumes increase. The multi-parameters of geomorphology, cloudy rainband, and wind field must be refined to imitate the complex rain-generating mechanism and precipitation. Therefore, direct calculation and storage of the complete Hessian matrix cannot be achieved, and the cost is very high. The Jacobian quasi-Newton often overestimates the

approximate state $\left|r_m \frac{\partial^2 r_m}{\partial \eta_i \partial \eta_j}\right| \ll \left|\frac{\partial r_m}{\partial \eta_i}\frac{\partial r_m}{\partial \eta_j}\right|$ and cannot guarantee its convergence [37]. In the case of multiple minima, LMA only converges to the global minimum when the initial prediction is close to the final solution [38], and its calculation speed is often slightly slower than that of the Jacobian quasi-Newton. The BFGS algorithm approximation must satisfy $\mathbf{A}(\mathbf{\eta}^{k+1})$ and curvature condition $(\mathbf{s}^{k-1})^T \mathbf{y}^{k-1} > 0$ to be positive and definite. The reasons for the above shortcomings are the scalar properties of the step size of the Jacobian quasi-Newton α^k, the damping factor λ of LMA, and the secant scale factors β^k and γ^k of the BFGS algorithm.

2.5. Rain-making causal analytical solving derivation of the hessian and Newton's constraint

2.5.1. Establishment of the rain-generating simulation model

This study uses composite advanced atmospheric–hydrogeographic-related functions to design the typhoon's rain-generating simulation model and embed it into the optimization model. First, the definite integral is extended to the designed multivariate rain-making causal composite function $f(\mathbf{\eta}) \circ g(\mathbf{\eta})$, where $g(\mathbf{\eta})$ is the unit rain-generating function and $f(\mathbf{\eta})$ is the reactive scaling function under the interaction between atmospheric factors. Let the domain $\mathbf{D}$ of the decision variable $\mathbf{\eta}$ in the function $f(\mathbf{\eta}) \circ g(\mathbf{\eta})$ conform to $f \circ g : \mathbf{D} \rightarrow \mathbb{R}$ and consider the so-called half-open half-closed Υ-dimensional rectangle area ($\Upsilon \in \mathbb{N} > 1$), then the domain $\mathbf{D}$ can be divided into:

$$
\begin{aligned}
\mathbf{D} = C_1 \cup C_2 \cup \cdots \cup C_i \cup \cdots \cup C_\Upsilon = \left[\rho_{t,s}^{AP}, \chi_{t,s}^{AP}\right) \times \left[\nu_{t,s}^{AWS}, \chi_{t,s}^{AWS}\right) \times \left[\left|\theta_{t,s}^{AWD} - \varphi_{t,s}^{ter}\right|, \left|\chi_{t,s}^{AWD} - \varphi_{t,s}^{ter}\right|\right) \times \\
\left[\nu_{t,s}^{MAWS}, \chi_{t,s}^{MAWS}\right) \times \left[\left|\theta_{t,s}^{MAWD} - \varphi_{t,s}^{mon}\right|, \left|\chi_{t,s}^{MAWD} - \varphi_{t,s}^{mon}\right|\right) \times \left[\nu_{t,s}^{MIWS}, \chi_{t,s}^{MIWS}\right) \times \left[\left|\theta_{t,s}^{MIWD} - \left(\frac{\omega \cdot \varphi_{t,s}^{mon} + \varpi \cdot \varphi_{t,s}^{ter}}{\omega + \varpi}\right)\right|, \\
\left|\chi_{t,s}^{MIWD} - \left(\frac{\omega \cdot \varphi_{t,s}^{mon} + \varpi \cdot \varphi_{t,s}^{ter}}{\omega + \varpi}\right)\right|\right) \times \left[h_{t,s}^{LC}, \chi_{t,s}^{LC}\right) \times \left[\varphi_{t,s}^{LCC}, \chi_{t,s}^{LCC}\right) \times \left[h_{t,s}^{CCei}, \chi_{t,s}^{CCei}\right) \times \left[\varphi_{t,s}^{TCC}, \chi_{t,s}^{TCC}\right) \quad \subset \mathbb{R}^\Upsilon
\end{aligned}
\tag{7}
$$

This study devises the three-variable (t, s, η) triple integral for the composite constant function $f(\mathbf{\eta}_{\cdot,t,s}) \circ g(\mathbf{\eta}_{\cdot,t,s}) = 1$ between the above-curved surface to calculate the rainfall depth $P(\mathbf{\eta}_{\cdot,t,s})$ at station s and time t while discretizing the multi-type rainfall causes $\mathbf{\eta}_{\cdot,t,s}$ to solve the multivariate functional definite integral. Since multiple integrals possess the properties of linearization, additivity, and monotonicity, among others, the definite integral of the Riemann integrable $f(\mathbf{\eta}) \circ g(\mathbf{\eta})$ in the interval of $\mathbf{D}$ can be given by equation (7) using functional Riemann sum, as expressed in equation (8a). Considering the wind direction-related rain-making causes, this study uses an expanded multi-level modeling framework (i.e., hierarchical nonlinear mixed-effects model) with the designed composite growth functions, that is, the swarm logistic tangent hyperbolic function $\mathrm{G}(\zeta_j^i, x_j^i)$ associated with the modified Malthusian atmospheric inter-reactive scaler $\mathrm{F}(\zeta_j^i, x_j^i)$ to estimate the rain-generating trajectories from multiple causes/geneses $\mathbf{\eta}$, in which the measured rain-making independent variable is converted to a hyperbolic angle, as shown in equation (8 b). In particular, the above calculations realize nonlinear/linear transformations by reducing/rotating the observed spatial(s)–temporal(t) variables $\chi_{t,s}^i$ and the rain-making threshold $\eta_{i,t,s}$ to activate the unit rain-generating function, as shown in equations (10). The hyperbolic angle surrounding the mapping area associated with the designed superimposed-mixed linear-nonlinear composite function is used to simulate the complex, highly nonlinear rain-generating mechanism and approximate the high-order irregular objective functional solution space, as expressed in equation (9).

$$
\begin{aligned}
P\left(\mathbf{\eta}_{\cdot,t,s}, \mathbf{\chi}_{t,s}\right) = \int_{t-\varepsilon_1}^{t} \int_{\varphi_1(s)}^{\psi_1(s)} \int_{\rho_{t,s}^{AP}}^{\chi_{t,s}^{AP}} \left[f\left(\eta_{1,t,s}\right) \circ g\left(\eta_{1,t,s}\right)\right] d\eta_{1,t,s} ds dt + \int_{t-\varepsilon_2}^{t} \int_{\varphi_2(s)}^{\psi_2(s)} \int_{\nu_{t,s}^{AWS}}^{\chi_{t,s}^{AWS}} \left[f\left(\eta_{2,t,s}\right) \circ g\left(\eta_{2,t,s}\right)\right] d\eta_{2,t,s} ds dt
\end{aligned}
$$

$$
+ \int_{t-\varepsilon_3}^{t} \int_{\varphi_3(s)}^{\psi_3(s)} \int_{\left|\theta_{t,s}^{AWD} - \varphi_{t,s}^{ter}\right|}^{\left|\chi_{t,s}^{AWD} - \varphi_{t,s}^{ter}\right|} f\left(\eta_{3,t,s}\right) \circ g\left(\eta_{3,t,s}\right) d\eta_{3,t,s} ds dt + \int_{t-\varepsilon_4}^{t} \int_{\varphi_4(s)}^{\psi_4(s)} \int_{\nu_{t,s}^{MAWS}}^{\chi_{t,s}^{MAWS}} f\left(\eta_{4,t,s}\right) \circ g\left(\eta_{4,t,s}\right) d\eta_{4,t,s} ds dt +
$$

$$
\int_{t-\varepsilon_5}^{t} \int_{\varphi_5(s)}^{\psi_5(s)} \int_{\left|\theta_{t,s}^{MAWD} - \varphi_{t,s}^{mon}\right|}^{\left|\chi_{t,s}^{MAWD} - \varphi_{t,s}^{mon}\right|} f\left(\eta_{5,t,s}\right) \circ g\left(\eta_{5,t,s}\right) d\eta_{5,t,s} ds dt + \int_{t-\varepsilon_6}^{t} \int_{\varphi_6(s)}^{\psi_6(s)} \int_{\nu_{t,s}^{MIWS}}^{\chi_{t,s}^{MIWS}} f\left(\eta_{6,t,s}\right) \circ g\left(\eta_{6,t,s}\right) d\eta_{6,t,s} ds dt +
$$

$$
\int_{t-\varepsilon_7}^{t} \int_{\varphi_7(s)}^{\psi_7(s)} \int_{\left|\theta_{t,s}^{MIWD} - \left(\frac{\omega \cdot \varphi_{t,s}^{mon} + \varpi \cdot \varphi_{t,s}^{ter}}{\omega + \varpi}\right)\right|}^{\left|\chi_{t,s}^{MIWD} - \left(\frac{\omega \cdot \varphi_{t,s}^{mon} + \varpi \cdot \varphi_{t,s}^{ter}}{\omega + \varpi}\right)\right|} f\left(\eta_{7,t,s}\right) \circ g\left(\eta_{7,t,s}\right) d\eta_{7,t,s} ds dt +
$$

$$
\int_{t-\varepsilon_8}^{t} \int_{\varphi_8(s)}^{\psi_8(s)} \int_{h_{t,s}^{LC}}^{\chi_{t,s}^{LC}} f\left(\eta_{8,t,s}\right) \circ g\left(\eta_{8,t,s}\right) d\eta_{8,t,s} ds dt + \int_{t-\varepsilon_9}^{t} \int_{\varphi_9(s)}^{\psi_9(s)} \int_{\varphi_{t,s}^{LCC}}^{\chi_{t,s}^{LCC}} f\left(\eta_{9,t,s}\right) \circ g\left(\eta_{9,t,s}\right) d\eta_{9,t,s} ds dt +
$$

$$
\int_{t-\varepsilon_{10}}^{t} \int_{\varphi_{10}(s)}^{\psi_{10}(s)} \int_{h_{t,s}^{CCei}}^{\chi_{t,s}^{CCei}} f\left(\eta_{10,t,s}\right) \circ g\left(\eta_{10,t,s}\right) d\eta_{10,t,s} ds dt + \int_{t-\varepsilon_{11}}^{t} \int_{\varphi_{11}(s)}^{\psi_{11}(s)} \int_{\varphi_{t,s}^{TCC}}^{\chi_{t,s}^{TCC}} f\left(\eta_{11,t,s}\right) \circ g\left(\eta_{11,t,s}\right) d\eta_{11,t,s} ds dt
\tag{8a}
$$

$$\approx N^{-1}\left\{\sum_{j=1}^{\Gamma} \mathrm{F}\left(\sum_{i=1}^{\Upsilon}\zeta_{i,j}, \sum_{i=1}^{\Upsilon}x_j^i\right)\cdot \mathrm{G}\left(\sum_{i=1}^{\Upsilon}\zeta_{i,j}, \sum_{i=1}^{\Upsilon}x_j^i\right)\right\} \tag{8b}$$

$$\cong\left\{\begin{array}{l} N^{-1}\left\{\sum_{j=1}^{\Gamma}\left[a_j\circ e^{\theta_j\circ\gamma_j\circ\sum_{i=1}^{\Upsilon}x_j^i}\cdot\dfrac{K_j}{1+\alpha_j\circ e^{-B_j\circ\sum_{i=1}^{\Upsilon}x_j^i}} - a_j\circ e^{\theta_j\circ\gamma_j\circ\sum_{i=1}^{\Upsilon}\zeta_{i,j}}\cdot\dfrac{K_j}{1+\alpha_j\circ e^{-B_j\circ\sum_{i=1}^{\Upsilon}\zeta_{i,j}}}\right]\right\} \\[2em] N^{-1}\left\{\sum_{j=1}^{\Gamma}\left[a_j\circ e^{\theta_j\circ\gamma_j\circ\sum_{i=1}^{\Upsilon}x_j^i}\cdot\dfrac{e^{B_j\sum_{i=1}^{\Upsilon}x_j^i}-e^{-B_j\sum_{i=1}^{\Upsilon}x_j^i}}{e^{B_j\sum_{i=1}^{\Upsilon}x_j^i}+e^{-B_j\sum_{i=1}^{\Upsilon}x_j^i}} - a_j\circ e^{\theta_j\circ\gamma_j\circ\sum_{i=1}^{\Upsilon}\zeta_{i,j}}\cdot\dfrac{e^{B_j\sum_{i=1}^{\Upsilon}\zeta_{i,j}}-e^{-B_j\sum_{i=1}^{\Upsilon}\zeta_{i,j}}}{e^{B_j\sum_{i=1}^{\Upsilon}\zeta_{i,j}}+e^{-B_j\sum_{i=1}^{\Upsilon}\zeta_{i,j}}}\right]\right\} \end{array}\right. \tag{9}$$

$$s.t.\left\{\begin{array}{l} \Pi\left(\chi_{t,s}^i\right)=\sum_{i=1}^{\Upsilon}w_{i,j}\cdot N\left(\chi_{t,s}^i\right)+b_j=\sum_{i=1}^{\Upsilon}x_j^i, \quad \Pi(\eta_{i,t,s})=\sum_{i=1}^{\Upsilon}w_{i,j}\cdot N(\eta_{i,t,s})+b_j=\sum_{i=1}^{\Upsilon}\zeta_{i,j} \\[1.5em] N\left(\chi_{t,s}^i\right)=\left\{\dfrac{\chi_{t,s}^i-\mu_1^{i,s}}{\left(\mu_2^{i,s}\right)^{\frac12}}=\dfrac{\chi_{t,s}^i-\mathrm{E}\left[\chi_{t,s}^i\right]}{\left(\mathrm{E}\left[\left(\chi_{t,s}^i-\mu_1^{i,s}\right)^2\right]\right)^{\frac12}}\right\vert\begin{array}{l}\mu_2^{i,s}=\sigma^2\equiv\mathrm{E}\left[\left(\chi_{t,s}^i-\mu_1^{i,s}\right)^2\right]\\[0.8em]\mu_1^{i,s}\equiv\mathrm{E}\left[\chi_{t,s}^i\right]\end{array}\right\} \\[2em] N^{-1}\{\bullet\}=\left\{\mathrm{F}\left(\sum_{i=1}^{\Upsilon}\zeta_{i,j},\sum_{i=1}^{\Upsilon}x_j^i\right)\mathrm{G}\left(\sum_{i=1}^{\Upsilon}\zeta_{i,j},\sum_{i=1}^{\Upsilon}x_j^i\right)\right\}\cdot\left(\mu_2^{j,s}\right)^{\frac12}+\mu_1^{j,s}\left\vert\begin{array}{l}\mu_2^{j,s}\equiv\mathrm{E}\left[\left(\varsigma_{t,j}\varphi_{j,s}^{\mathrm{T}}D_s-\mu_1^{j,s}\right)^2\right]\\[0.8em]\mu_1^{j,s}\equiv\mathrm{E}\left[\varsigma_{t,j}\varphi_{j,s}^{\mathrm{T}}D_s\right],\quad P_{\mathrm{obs}}(t,s)=\sum_{j=1}^{\Gamma}\varsigma_{t,j}\varphi_{j,s}^{\mathrm{T}}D_s\end{array}\right. \end{array}\right. \tag{10}$$

$$\boldsymbol{\chi}_{t,s}\in\left\{\begin{array}{l}\chi_{t,s}^1,\chi_{t,s}^2,\chi_{t,s}^3,\chi_{t,s}^4,\chi_{t,s}^5,\chi_{t,s}^6,\\[0.5em]\chi_{t,s}^7,\chi_{t,s}^8,\chi_{t,s}^9,\chi_{t,s}^{10},\chi_{t,s}^{11}\end{array}\right\}=\left[\begin{array}{l}\chi_{t,s}^{\mathrm{AP}},\chi_{t,s}^{\mathrm{AWS}},\left\vert\chi_{t,s}^{\mathrm{AWD}}-\varphi_{t,s}^{\mathrm{ter}}\right\vert,\chi_{t,s}^{\mathrm{MAWS}},\left\vert\chi_{t,s}^{\mathrm{MAWD}}-\varphi_{t,s}^{\mathrm{mon}}\right\vert,\chi_{t,s}^{\mathrm{MIWS}},\\[0.8em]\left\vert\chi_{t,s}^{\mathrm{MIWD}}-\left(\dfrac{\omega\cdot\varphi_{t,s}^{\mathrm{mon}}+\varpi\cdot\varphi_{t,s}^{\mathrm{ter}}}{\omega+\varpi}\right)\right\vert,\chi_{t,s}^{\mathrm{LC}},\chi_{t,s}^{\mathrm{LCC}},\chi_{t,s}^{\mathrm{CCei}},\chi_{t,s}^{\mathrm{TCC}}\end{array}\right] \tag{11}$$

here $\boldsymbol{\chi}$ is the atmospheric observed rain-making causal spatiotemporal vector composed of the 11 items in $\chi_{t,s}^i(i=1,2,...,11)$, known as explanatory variables considering multiple inputs, as shown in equation (11); ε_i is the travel time for measured precipitation during rain-growth process from rain-generation to falling on the ground surface; $\varphi_i(s)$ and $\psi_i(s)$ are the spatial rain-making bounds of the ith cause at sth station; $\eta_{i,t,s}$ is the rain-generating threshold of the ith rain-making cause at time t and station s; Υ and Γ are the total number of rain-making causes and dimension-reduced spatiotemporal components through SVD, respectively; a_j, θ_j, w_{ji}, and b_j are model parameters to be fitted; K_j is the carrying capacity generated by the ith rain-making cause at the spatiotemporal component j; B_j is the logistic growth rate or curve steepness; α_j is related to atmospheric preconditions and initial conditions of cause i down-dimensionally at component j; x_j^i and ζ_j^i are the mapping dimension-reduced variables projected from the ith observed spatiotemporal variable $\chi_{t,s}^i$ and the rain-making threshold parameter $\eta_{i,t,s}$, respectively, through rotation, scaling, and linear and nonlinear transformation; $N(\bullet)$ is the nonlinearly normalized function for $\chi_{t,s}^i$ or $\eta_{i,t,s}$ calculated using the first-order moment $\mu_1^{i,s}=\underset{t}{\mathrm{E}}[\chi_{t,s}^i]$ and the second-order moment $\mu_2^{i,s}=\underset{t}{\mathrm{E}}[(\chi_{t,s}^i-\mu_1^{i,s})^2]$; and $N^{-1}\{\bullet\}$ is the de-normalizing function for the simulated model output $\mathrm{F}(\zeta_j^i,x_j^i)\mathrm{G}(\zeta_j^i,x_j^i)$ using the first-order moment $\mu_1^{j,s}\equiv\underset{t}{\mathrm{E}}[\widetilde{c_{t,j}}F_{j,s}^{\mathrm{T}}D_s]$ and the second-order moment $\mu_2^{j,s}\equiv\underset{t}{\mathrm{E}}[(\widetilde{c_{t,j}}F_{j,s}^{\mathrm{T}}D_s-\mu_1^{j,s})^2]$, where $\widetilde{c_{t,j}}F_{j,s}^{\mathrm{T}}D_s$ is the dimension-reduced rainfall feature component j calculated through SVD of spatiotemporal precipitation observations $P_{\mathrm{obs}}(t,s)$.

The integrals of all continuous non-negative convex functions are sigmoid (with an "S" shape), which are also called the "two-focus curve functions." Therefore, the cumulative distribution function (e.g., error function) of many common probability distributions (e.g., normal distribution) is an S-shaped curve. Common sigmoid functions include generalized logistic, hyperbolic tangent, arctangent, Goodman, and smooth step functions, among others. Hyperbolic functions appear in the solutions of some important linear differential equations (e.g., define catenary and Laplace equation). However, few previous studies have used the generalized composite logistic and hyperbolic functions, which allow for generating more flexible sigmoid curves, to construct rain-generating simulation models. The causal rain-generating function in equation (9) is designed as a swarm hyperbolic tangent function, that is $\mathrm{G}(\zeta_{i,j},x_j^i)\in\left\{\dfrac{e^{B_j\sum_i x_j^i}-e^{-B_j\sum_i x_j^i}}{e^{B_j\sum_i x_j^i}+e^{-B_j\sum_i x_j^i}},\dfrac{e^{B_j\sum_i\zeta_{i,j}}-e^{-B_j\sum_i\zeta_{i,j}}}{e^{B_j\sum_i\zeta_{i,j}}+e^{-B_j\sum_i\zeta_{i,j}}}\right\}=\{\tanh(B_j\sum_{i=1}^{\Upsilon}x_j^i),\tanh(B_j\sum_{i=1}^{\Upsilon}\zeta_{i,j})\}$. If $K_j=\alpha_j=B_j=1$ in equation (9), the logistic function becomes an offset and scaled hyperbolic tangent function, yielding $\mathrm{G}(\zeta_{i,j},x_j^i)=\left\{\dfrac{1}{1+e^{-\sum_i x_j^i}},\dfrac{1}{1+e^{-\sum_i\zeta_{i,j}}}\left\vert\begin{array}{l}K_j=1\\\alpha_j=1\\B_j=1\end{array}\right.\right\}=\left\{\dfrac12+\dfrac12\tanh\left(\dfrac{\sum_i x_j^i}{2},\dfrac{\sum_i\zeta_{i,j}}{2}\right)\right\}$.

Quantitatively, the logistic curve shows early exponential growth for cause values near the threshold to trigger rainfall, indicating linear growth for an argument near the midpoint between the threshold and maximum, and then approaches K with an exponentially decaying gap. In addition, equation (10) first computes a linear combination of its input signals and applies a bounded logistic or hyperbolic tangent function as the simulator to the precipitation. Hence, this simulation model can be considered a "smoothed" variant approximating the complex, highly nonlinear rainfall mechanism and a high-order irregular objective function solution space.

2.5.2. Key-lock quasi-Newton for solving model parameter optimization

Next, we use mathematical analysis to derive the analytical solution of rain-generating parameter optimization, which embeds a simulation model. To optimize the rain-making threshold of each rainfall cause, we first converted the atmospheric factorial measurement $\boldsymbol{\chi}$ in equation (12) to a linear algebraic combination of the identified threshold solution $\boldsymbol{\eta}^k$, correction vector $\Delta\boldsymbol{\eta}^k$, and observed steering vector $\mathbf{c}^k$ of iteration (k), that is $\boldsymbol{\chi}_{t,s} = \boldsymbol{\eta}^k_{\cdot,t,s} + \Delta\boldsymbol{\eta}^k_{\cdot,t,s} + \mathbf{c}^k_{\cdot,t,s}\Big|_{\cdot \to i=1\sim\Upsilon}^{\mathbf{c}^k_{\cdot,t,s}\in\mathbb{R}}$. The calculation methods of model-independent variable $\Pi(\boldsymbol{\chi}_{t,s}) = \mathbf{x}_*$ after nonlinear normalization $N(\boldsymbol{\chi}_{t,s})$ and spatiotemporal linear conversion are shown in equations (15), respectively, where $N(\boldsymbol{\chi}_{t,s})$ uses entry-wise products for matrix operations. $F(\zeta^i_j, x^i_j)$ is the increase/decrease effect caused by the factorial inter-exchange reaction $j = * = 1 \sim \Gamma$ (as reflected by parameters a and γ) during rain generation, which can be regarded as the induced scaling factor for the rain-making cause i. As the inter-causal rain-generating reactive interaction is related to the atmospheric factorial intensity and gradient, this study designs explicitly γ^k_* as the rain-generating increase/decrease rate vector that is triggered by various rain-making causal reactions and devises $\boldsymbol{\theta}_* \in (-\boldsymbol{\sigma}, +\boldsymbol{\sigma})$ as the positive/negative small supplement vector. Accordingly, by substituting the above-mentioned derivation into equation (12), the rain-generating spatiotemporal precipitation simulation can be derived using equation (13). However, according to the definition of sensitivity coefficient [47], the simulated precipitation $P\left(\boldsymbol{\eta}^{k+1}_{\cdot,\bullet,s}, \boldsymbol{\chi}_{\bullet,s}\Big|_{\bullet\to t=1\sim T}^{\cdot\to i=1\sim\Upsilon}\right)$ will be approximately equal to its sensitivity (first-order derivative) $\frac{\partial P^{k+1}_{\text{sim}}}{\partial\boldsymbol{\eta}^{k+1}_{\cdot,\bullet,s}}$ multiplied by $\mathbf{c}^k_{\cdot,\bullet,s}$, which can be calculated by subtracting the atmospheric rain-making causal measurement variable $\boldsymbol{\chi}_{\cdot,\bullet,s}$ from the rain-generating threshold $\boldsymbol{\eta}^k_{\cdot,\bullet,s}$ and correction vector $\Delta\boldsymbol{\eta}^k_{\cdot,\bullet,s}$, satisfying Newton's conditional constraints (i.e., $\mathbf{c}^k_{\cdot,\bullet,s} = \boldsymbol{\chi}_{\bullet,s} - \boldsymbol{\eta}^k_{\cdot,\bullet,s} - \Delta\boldsymbol{\eta}^k_{\cdot,\bullet,s}$), as shown in equation (14).

$$P\left(\boldsymbol{\eta}_{\cdot,\bullet,s}, \boldsymbol{\chi}_{\bullet,s}\right) = N^{-1}\left\{P_{\text{sim}}\left(\Pi\left(\boldsymbol{\eta}^{k+1}_{\cdot,\bullet,s}\right), \Pi\left(\boldsymbol{\chi}_{\bullet,s}\right)\right)\right\} = N^{-1}\left\{P_{\text{sim}}\left(\mathbf{w}^{\mathrm{T}}_{\cdot,*}\cdot N\left(\boldsymbol{\eta}^{k+1}_{\cdot,\bullet,s}\right) + \mathbf{b}_*, \mathbf{w}^{\mathrm{T}}_{\cdot,*} N\left(\boldsymbol{\chi}_{\bullet,s}\right) + \mathbf{b}_* \Bigg|_{\bullet\to t=1\sim T}^{\substack{\cdot\to i=1\sim\Upsilon \\ *\to j=1\sim\Gamma}}\right)\right\}$$

$$= N^{-1}\left\{P_{\text{sim}}\left(\Pi\left(\boldsymbol{\eta}^{k+1}_{\cdot,\bullet,s}\right), \Pi\left(\boldsymbol{\eta}^k_{\cdot,\bullet,s} + \Delta\boldsymbol{\eta}^k_{\cdot,\bullet,s} + \mathbf{c}^k_{\cdot,\bullet,s}\right)\right)\right\} = \tag{12}$$

$$\begin{cases} N^{-1}\left\{\left[\mathbf{a}_* \circ e^{\boldsymbol{\theta}_*\circ\gamma^k_*\circ\Pi\left(\boldsymbol{\eta}^k+\Delta\boldsymbol{\eta}^k+\mathbf{c}^k\right)}_{\mathrm{M}\times\Gamma}\cdot\left(\frac{\mathbf{K}_*}{\iota+\boldsymbol{\alpha}_*\circ e^{-\mathbf{B}_*\circ\Pi\left(\boldsymbol{\eta}^k+\Delta\boldsymbol{\eta}^k+\mathbf{c}^k\right)}}\right)^{\mathrm{T}}_{\Gamma\times\mathrm{M}}\right]\cdot\boldsymbol{\upsilon} - \mathbf{a}_* e^{\boldsymbol{\theta}_*\gamma^k_*\Pi\left(\boldsymbol{\eta}^{k+1}\right)}_{\mathrm{M}\times\Gamma}\cdot\left(\frac{\mathbf{K}_*}{\iota+\boldsymbol{\alpha}_*\circ e^{-\mathbf{B}_*\Pi\left(\boldsymbol{\eta}^{k+1}\right)}}\right)^{\mathrm{T}}\boldsymbol{\upsilon}\right\} \\ N^{-1}\left\{\mathbf{a}_* \circ e^{\boldsymbol{\theta}_*\circ\gamma^k_*\Pi\left(\boldsymbol{\eta}^k+\Delta\boldsymbol{\eta}^k+\mathbf{c}^k\right)}\cdot\left(\frac{\mathbf{B}_* e^{\Pi\left(\boldsymbol{\eta}^k+\Delta\boldsymbol{\eta}^k+\mathbf{c}^k\right)} - \mathbf{B}_* e^{-\Pi\left(\boldsymbol{\eta}^k+\Delta\boldsymbol{\eta}^k+\mathbf{c}^k\right)}}{\mathbf{B}_* e^{\Pi\left(\boldsymbol{\eta}^k+\Delta\boldsymbol{\eta}^k+\mathbf{c}^k\right)} + \mathbf{B}_* e^{-\Pi\left(\boldsymbol{\eta}^k+\Delta\boldsymbol{\eta}^k+\mathbf{c}^k\right)}}\right)^{\mathrm{T}}\cdot\boldsymbol{\upsilon} - \mathbf{a}_* e^{\boldsymbol{\theta}_*\gamma^k_*\Pi\left(\boldsymbol{\eta}^{k+1}\right)}\cdot\left(\frac{\mathbf{B}_* e^{\Pi\left(\boldsymbol{\eta}^{k+1}\right)} - \mathbf{B}_* e^{-\Pi\left(\boldsymbol{\eta}^{k+1}\right)}}{\mathbf{B}_* e^{\Pi\left(\boldsymbol{\eta}^{k+1}\right)} + \mathbf{B}_* e^{-\Pi\left(\boldsymbol{\eta}^{k+1}\right)}}\right)^{\mathrm{T}}\boldsymbol{\upsilon}\right\} \end{cases} \tag{13}$$

$$\approx \left[\frac{\partial P^{k+1}_{\text{sim}}}{\partial\boldsymbol{\eta}^{k+1}_{\cdot,\bullet,s}}\right]_{\mathrm{M}\times\mathrm{L}}\left[\mathbf{c}^k_{\cdot,\bullet,s}\right]_{\mathrm{L}\times1}\Bigg|_{\bullet\to t=1\sim T}^{\substack{\cdot\to i=1\sim\Upsilon \\ j=1\sim\Gamma}}, \quad \boldsymbol{\eta}^k_{\cdot,\bullet,s} + \Delta\boldsymbol{\eta}^k_{\cdot,\bullet,s} = \boldsymbol{\eta}^{k+1}_{\cdot,\bullet,s}, \quad \mathbf{c}^k_{\cdot,\bullet,s} = \boldsymbol{\chi}_{\cdot,s} - \boldsymbol{\eta}^k_{\cdot,\bullet,s} - \Delta\boldsymbol{\eta}^k_{\cdot,\bullet,s} \tag{14}$$

$$s.t.\begin{cases} N\left(\boldsymbol{\chi}_{t,s}\right) = \left\{\dfrac{\boldsymbol{\chi}_{t,s} - \boldsymbol{\mu}^{\cdot,s}_1}{(\boldsymbol{\mu}^{\cdot,s}_2)^{\frac{1}{2}}} = \dfrac{\boldsymbol{\chi}_{t,s} - \mathrm{E}_t\left[\boldsymbol{\chi}_{t,s}\right]}{\left(\mathrm{E}_t\left[\left(\boldsymbol{\chi}_{t,s} - \boldsymbol{\mu}^{\cdot,s}_1\right)^2\right]\right)^{\frac{1}{2}}}\Bigg| \begin{array}{l}\boldsymbol{\mu}^{\cdot,s}_2 \equiv \mathrm{E}_t\left[\left(\boldsymbol{\chi}_{t,s} - \boldsymbol{\mu}^{\cdot,s}_1\right)^2\right] \\ \boldsymbol{\mu}^{\cdot,s}_1 \equiv \mathrm{E}_t\left[\boldsymbol{\chi}_{t,s}\right]\end{array}\right\} \\[4mm] \Pi\left(\boldsymbol{\chi}_{t,s}\right) = \Pi\left(\boldsymbol{\eta}^k_{\cdot,t,s} + \Delta\boldsymbol{\eta}^k_{\cdot,t,s} + \mathbf{c}^k_{\cdot,t,s}\right) = \mathbf{w}^{\mathrm{T}}_{\cdot,*}\cdot\left[\left(\boldsymbol{\eta}^k_{\cdot,t,s} + \Delta\boldsymbol{\eta}^k_{\cdot,t,s} + \mathbf{c}^k_{\cdot,t,s}\right) - \boldsymbol{\mu}^{\cdot,s}_1\right]\cdot(\boldsymbol{\mu}^{\cdot,s}_2)^{-\frac{1}{2}} + \mathbf{b}_* = \mathbf{x}_* \\[4mm] \boldsymbol{\upsilon} \in \left\{\boldsymbol{\upsilon}_\bullet\Bigg|_{M=T\times S=T,S=1}^{\bullet\to t=1\sim T}\right\}_{\mathrm{M}\times1} = \begin{bmatrix} u_1 \\ \vdots \\ u_t \\ \vdots \\ u_T \end{bmatrix}\begin{array}{l} u_t = 1, \quad if \quad t = \bullet \\ u_t = 0, \quad if \quad t \neq \bullet \\ u_t \in (0,1) \\ \displaystyle\sum_{t=1}^T u_t = 1 \end{array}\Bigg]_{\mathrm{T}\times1} \end{cases} \tag{15}$$

where $\mathbf{c}^k_{\cdot,t,s} \in [c^k_{i,t,s}]$ represents the potential induced precipitation caused by the ith atmospheric causal rain-making measured values exceeding the rain-generating threshold and $\boldsymbol{\upsilon}_\bullet$ is the unit vector of the $m = \cdot^{\text{th}}$ observed/simulated precipitation. To achieve the most

efficient convergence, the optimization procedure is expected to search for an optimal solution in the next iteration $(k+1)^{\text{th}}$. If $\boldsymbol{\eta}_{\cdot,t,s}^{k+1}$ is equal to the true (optimal) causal rain-making threshold (i.e., $\boldsymbol{\eta}_{\cdot,t,s}^{k+1} = \boldsymbol{\eta}_{\cdot,t,s}^{@}$), the rain-generating function in equation (13) is expected to be equal to 0 (i.e., $\frac{e^{B_j \Pi(\eta_{i,t,s}^{k+1})} - e^{-B_j \Pi(\eta_{i,t,s}^{k+1})}}{e^{B_j \Pi(\eta_{i,t,s}^{k+1})} + e^{-B_j \Pi(\eta_{i,t,s}^{k+1})}} = 0$ and $\frac{K_j}{1 + \alpha_j e^{-B_j \Pi(\eta_{i,t,s}^{k+1})}} = 0$). Similarly, according to the definition, if the iteratively identified rain-making threshold $\boldsymbol{\eta}_{\cdot,\bullet,s}^{k}$ is approaching the real value (i.e., $\boldsymbol{\eta}_{\cdot,t,s}^{k} \approx \boldsymbol{\eta}_{\cdot,t,s}^{@}$), then the rain-generating function $\boldsymbol{\eta}_{\cdot,\bullet,s}^{k}$ is expected to approximate 0 (i.e., $\frac{e^{B_j \Pi(\eta_{i,t,s}^{k})} - e^{-B_j \Pi(\eta_{i,t,s}^{k})}}{e^{B_j \Pi(\eta_{i,t,s}^{k})} + e^{-B_j \Pi(\eta_{i,t,s}^{k})}} \approx 0$ and $\frac{K_j}{1 + \alpha_j e^{-B_j \Pi(\eta_{i,t,s}^{k})}} \approx 0$). Therefore, based on equations (13)–(15), $P(\boldsymbol{\eta}_{\cdot,\bullet,s}, \boldsymbol{\chi}_{\bullet,s})$ can be re-written as follows:

$$
\begin{aligned}
P\left(\boldsymbol{\eta}_{\cdot,\bullet,s}, \boldsymbol{\chi}_{\bullet,s}\right) &\approx N^{-1}\left\{P_{\text{sim}}\left(\Pi\left(\boldsymbol{\eta}_{\cdot,\bullet,s}^{k}\right), \Pi\left(\boldsymbol{\chi}_{\bullet,s}\right)\right)\right\} = N^{-1}\left\{P_{\text{sim}}\left(\Pi\left(\boldsymbol{\eta}_{\cdot,\bullet,s}^{k}\right), \Pi\left(\boldsymbol{\eta}_{\cdot,\bullet,s}^{k} + \Delta\boldsymbol{\eta}_{\cdot,\bullet,s}^{k} + \mathbf{c}_{\cdot,\bullet,s}^{k}\right)\right)\right\} \\
&\approx \left[\frac{\partial P_{\text{sim}}^{k}}{\partial \boldsymbol{\eta}_{\cdot,\bullet,s}^{k}}\right]_{M \times L} \left[\Delta\boldsymbol{\eta}_{\cdot,\bullet,s}^{k} + \mathbf{c}_{\cdot,\bullet,s}^{k}\right]_{L \times 1} = \left[\frac{\partial P_{\text{sim}}^{k}}{\partial \boldsymbol{\eta}_{\cdot,\bullet,s}^{k}}\right]_{M \times L} \left[\boldsymbol{\chi}_{\bullet,s} - \boldsymbol{\eta}_{\cdot,\bullet,s}^{k}\right]_{L \times 1}, \quad \mathbf{c}_{\cdot,\bullet,s}^{k} = \boldsymbol{\chi}_{\bullet,s} - \boldsymbol{\eta}_{\cdot,\bullet,s}^{k} - \Delta\boldsymbol{\eta}_{\cdot,\bullet,s}^{k}
\end{aligned}
\tag{16}
$$

Equation (2) uses the second-order Taylor expansion technique to approximate the objective function J around $\boldsymbol{\eta}^{k}$, differentiates the objective expansion $J_{\text{T}}(P_{\text{sim}}(\boldsymbol{\eta}^{k+1}, \boldsymbol{\chi}), P_{\text{obs}})$ regarding $\Delta\boldsymbol{\eta}^{k}$, and solves the expanded derivative roots to expect the identified parameters $\boldsymbol{\eta}^{k+1} = \boldsymbol{\eta}^{k} + \Delta\boldsymbol{\eta}^{k}$ as the stationary point of J at the next iteration $k+1$ (i.e., optimal solution), as shown in equations (3a) and (3b). This front-door direct-solving approach assumes the structure and type of the correction vector $\Delta\boldsymbol{\eta}^{k}$ composed of the first- and second-order derivatives of J can be identified. However, since J and the multi-variate variables $P_{\text{sim}}(\boldsymbol{\eta}^{k+1}, \boldsymbol{\chi})$ are multi-dimensional and highly nonlinear composite functions, when the number of parameters is large, and the simulated computation model is complex, the second derivative of J (i.e., the Hessian matrix) $\mathbf{H}(J_{\text{T}}(P_{\text{sim}}(\boldsymbol{\eta}^{k}, \boldsymbol{\chi}), P_{\text{obs}}))$ cannot be directly calculated. To solve this problem, this study designs a backdoor feedback contrast derivation method. First, $P_{\text{sim}}(\boldsymbol{\eta}^{k+1}, \boldsymbol{\chi})$ is expressed as a systematic nonlinear algebraic equation, as shown in equations (12)–(13). Second, the roots of $0 = \frac{dJ^{k+1}}{d\Delta\boldsymbol{\eta}^{k}}$ are solved to derive algebraic formulation using calculus, as shown in equation (17). Third, the simulated precipitation $P_{\text{sim}}(\boldsymbol{\eta}^{k+1}, \boldsymbol{\chi})$ with the composite rain-generating function is used to approximate $P_{\text{sim}}^{\text{TE}}(\boldsymbol{\eta}^{k} + \Delta\boldsymbol{\eta}^{k}, \boldsymbol{\chi})$ using second-order Taylor expansion around $\boldsymbol{\eta}^{k}$ and $\Delta\boldsymbol{\eta}^{k}$; the differential derivation for $\boldsymbol{\eta}^{k}$ is expressed in equation (17). Fourth, using equations (12)–(16), the relationship between simulated precipitation $P_{\text{sim}}(\Pi(\boldsymbol{\eta}^{k}), \cdot)$ and its derivative $P'_{\text{sim}}(\Pi(\boldsymbol{\eta}^{k}), \cdot) = \frac{dP_{\text{sim}}(\Pi(\boldsymbol{\eta}^{k}), \cdot)}{d\boldsymbol{\eta}^{k}}$ is derived according to the composite function type and substituted into equation (18) to obtain an algebraic equation with replacement variables, as shown in equation (19). Fifth, using Leibniz's and chain rules, the advanced functions of the derivative equaling 0 of the rain-generating simulation models $P_{\text{sim}}(\Pi(\boldsymbol{\eta}^{k}), \cdot)$ composited by a logistic function (14a) or a tangent hyperbolic function (14 b) is derived, as shown in equations (20), respectively. Sixth, the variables of term 1 in equation (19) are replaced according to the multi-order derivative relationship derived from equations (12)–(16), and the definition in equation (24) is substituted with the higher-order Taylor's expanded functional form $J(P_{\text{sim}}^{\text{TE}}(\boldsymbol{\eta}^{k+1}, \boldsymbol{\chi}), P_{\text{obs}})$, as expressed in equation (20). Seventh, the structural equation (3a) of the front-door direct-solving method is compared with the derived equation (22) of the backdoor feedback contrast method to derive the advanced algebraic analytical solution of the Hessian matrix, as expressed in equations (23), and the constrained equations (23) that satisfy Newton's conditions to efficiently solve a finite number of candidate solutions for parameter correction vectors $\Delta\boldsymbol{\eta}^{k^-}$.

$$
\begin{aligned}
0 = \frac{dJ^{k+1}}{d\Delta\boldsymbol{\eta}^{k}} &= \frac{d}{d\Delta\boldsymbol{\eta}_{\cdot,t,s}^{k}}\left[N^{-1}\left\{P_{\text{sim}}\left(\Pi\left(\boldsymbol{\eta}_{\cdot,t,s}^{k+1}\right), \Pi\left(\boldsymbol{\chi}_{t,s}\right)\right)\right\} - P_{\text{obs}}(t,s)\right]^{\text{T}}\left[N^{-1}\left\{P_{\text{sim}}\left(\Pi\left(\boldsymbol{\eta}_{\cdot,t,s}^{k+1}\right), \Pi\left(\boldsymbol{\chi}_{t,s}\right)\right)\right\} - P_{\text{obs}}(t,s)\right] \\
&= 2\left[N^{-1}\left\{P_{\text{sim}}\left(\Pi\left(\boldsymbol{\eta}_{\cdot,t,s}^{k+1}\right), \Pi\left(\boldsymbol{\chi}_{t,s}\right)\right)\right\} - P_{\text{obs}}(t,s)\right]^{\text{T}} \frac{dN^{-1}\left\{P_{\text{sim}}\left(\Pi\left(\boldsymbol{\eta}_{\cdot,t,s}^{k+1}\right), \Pi\left(\boldsymbol{\chi}_{t,s}\right)\right)\right\}}{d\Delta\boldsymbol{\eta}_{\cdot,t,s}^{k}}
\end{aligned}
\tag{17}
$$

Use Taylor expansion for the simulated precipitation P_{sim}

$$
\begin{aligned}
&= 2\left[N^{-1}\left\{P_{\text{sim}}^{\text{TE}}\left(\Pi\left(\boldsymbol{\eta}_{\cdot,t,s}^{k} + \Delta\boldsymbol{\eta}_{\cdot,t,s}^{k}\right), \Pi\left(\boldsymbol{\chi}_{t,s}\right)\right)\right\} - P_{\text{obs}}\right]^{\text{T}} \frac{dN^{-1}\left\{P_{\text{sim}}\left(\Pi\left(\boldsymbol{\eta}_{\cdot,t,s}^{k} + \Delta\boldsymbol{\eta}_{\cdot,t,s}^{k}\right), \Pi\left(\boldsymbol{\eta}_{\cdot,t,s}^{k} + \Delta\boldsymbol{\eta}_{\cdot,t,s}^{k} + \mathbf{c}_{\cdot,t,s}^{k}\right)\right)\right\}}{d\Delta\boldsymbol{\eta}_{\cdot,t,s}^{k}} \\
&\approx 2\left[N^{-1}\left\{P_{\text{sim}}\left(\Pi(\boldsymbol{\eta}^{k}), \cdot\right) + P'_{\text{sim}}\left(\Pi(\boldsymbol{\eta}^{k}), \cdot\right) \cdot \overline{\Delta\boldsymbol{\eta}}^{k} + \frac{1}{2}(\overline{\Delta\boldsymbol{\eta}}^{k})^{\text{T}} \frac{d}{d\boldsymbol{\eta}^{k}}\left(\frac{dP_{\text{sim}}(\Pi(\boldsymbol{\eta}^{k}), \cdot)}{d\boldsymbol{\eta}^{k}}\right) \cdot \overline{\Delta\boldsymbol{\eta}}^{k}\right\} - P_{\text{obs}}\right]^{\text{T}} \\
&\quad \frac{dN^{-1}\left\{P_{\text{sim}}(\Pi(\boldsymbol{\eta}^{k} + \Delta\boldsymbol{\eta}^{k}), \Pi(\boldsymbol{\eta}^{k} + \Delta\boldsymbol{\eta}^{k} + \mathbf{c}^{k}))\right\}}{d\Delta\boldsymbol{\eta}^{k}}
\end{aligned}
\tag{18}
$$

According to the derived
conditions expressed in Equation (16) for P'_{sim}

$$\approx 2\left[\left\{N^{-1}\left[P_{\text{sim}}\left(\Pi(\boldsymbol{\eta}^k),\cdot\right)\right]+N^{-1}\left[P_{\text{sim}}\left(\Pi(\boldsymbol{\eta}^k),\cdot\right)\right]\left[\frac{1}{\chi^i_{t,s}-\eta^k_{i,t,s}}\right]^T_{1\times L}\Delta\boldsymbol{\eta}^k+\frac{1}{2}(\Delta\boldsymbol{\eta}^k)^T\frac{d}{d\boldsymbol{\eta}^k}\right.\right.$$

$$\left.\left.\left(N^{-1}\left[P_{\text{sim}}\left(\Pi(\boldsymbol{\eta}^k),\cdot\right)\right]\left[\frac{1}{\Delta\eta^k_{i,t,s}+c^k_{i,t,s}}\right]^T_{1\times L}\right)\Delta\boldsymbol{\eta}^k-P_{\text{obs}}\right\}\frac{dN^{-1}\{P_{\text{sim}}(\Pi(\boldsymbol{\eta}^k+\Delta\boldsymbol{\eta}^k),\Pi(\boldsymbol{\chi}))\}}{d\Delta\boldsymbol{\eta}^k}\right]$$

$$\approx 2\left[N^{-1}\left\{P_{\text{sim}}\left(\Pi(\boldsymbol{\eta}^k),\bullet\right)+P'_{\text{sim}}\left(\Pi(\boldsymbol{\eta}^k),\bullet\right)\cdot\overline{\Delta\boldsymbol{\eta}}^k+\frac{1}{2}\left(\overline{\Delta\boldsymbol{\eta}}^k\right)^T\frac{d}{d\boldsymbol{\eta}^k}\left(\frac{dP_{\text{sim}}(\Pi(\boldsymbol{\eta}^k),\bullet)}{d\boldsymbol{\eta}^k}\right)\cdot\overline{\Delta\boldsymbol{\eta}}^k\right\}-P_{\text{obs}}\right]\frac{dN^{-1}\{P_{\text{sim}}(\Pi(\boldsymbol{\eta}^k+\Delta\boldsymbol{\eta}^k),\Pi(\boldsymbol{\eta}^k+\Delta\boldsymbol{\eta}^k+\mathbf{c}^k))\}}{d\Delta\boldsymbol{\eta}^k} \tag{19}$$

Use Leibniz's rule and chain rule for P'_{sim} being composite logistic function (14a) or tangent hyperbolic function (14b) under derivative $= 0$

$$\approx \begin{cases} \text{1. Compound type of generalized} & \left\{2\left[\mathbf{r}^k+\boldsymbol{\kappa}^k\right]^T_{1\times M}\cdot N^{-1}\left[\left[(\boldsymbol{\mu}^{*,s}_2)^{\frac{-1}{2}}\cdot\mathbf{w}_{\bullet,\bullet}\right]_{1\times\Gamma}\boldsymbol{\theta}^T_{\Gamma\times1}\cdot\left(\mathbf{a}_*e^{\boldsymbol{\theta}\boldsymbol{\gamma}^k}\Pi(\boldsymbol{\chi})\right)\left(\frac{\boldsymbol{\iota}}{\boldsymbol{\iota}+\boldsymbol{\alpha}_*e^{-\mathbf{B}_*}\Pi(\boldsymbol{\chi})}\right)^T\boldsymbol{\upsilon}\right]\cdot N^{-1}(\boldsymbol{\gamma}^k)_{1\times L}\right\}^T+ \\[2em] \text{logistic function (GLF)} & \left\{N^{-1}(\mathbf{B})^T_{L\times1}\cdot2\left[\mathbf{r}^k+\boldsymbol{\kappa}^k\right]^T\cdot N^{-1}\left(\mathbf{a}_*e^{\boldsymbol{\theta}\boldsymbol{\gamma}^k}\Pi(\boldsymbol{\chi})\cdot\left[\frac{\boldsymbol{\iota}}{\boldsymbol{\iota}+\boldsymbol{\alpha}_*e^{-\mathbf{B}_*}\Pi(\boldsymbol{\chi})}\right]^T\left[\frac{\boldsymbol{\alpha}_*e^{-\mathbf{B}_*}\Pi(\boldsymbol{\chi})}{\boldsymbol{\iota}+\boldsymbol{\alpha}_*e^{-\mathbf{B}_*}\Pi(\boldsymbol{\chi})}\right]\left[(\boldsymbol{\mu}^{*,s}_2)^{\frac{-1}{2}}\cdot\mathbf{w}_{\bullet,\bullet}\right]^T_{\Gamma\times1}\right)\left[\frac{L^{-1}}{\Delta\boldsymbol{\eta}^k}\right]^T_{1\times L}\cdot\Delta\boldsymbol{\eta}^k\right|\mathbf{K}_*=\boldsymbol{\iota} \end{cases} \tag{20a}$$

$$\approx \begin{cases} \text{2. Compound type of tangent hyperbolic} & \left\{2\left[\mathbf{r}^k+\boldsymbol{\kappa}^k\right]^T_{1\times M}\cdot N^{-1}\left[\left[(\boldsymbol{\mu}^{*,s}_2)^{\frac{-1}{2}}\cdot\mathbf{w}_{\bullet,\bullet}\right]_{1\times\Gamma}\boldsymbol{\theta}^T_{\Gamma\times1}\cdot\left(\mathbf{a}_*e^{\boldsymbol{\theta}\boldsymbol{\gamma}^k}\Pi(\boldsymbol{\chi})\right)\left(\frac{e^{\mathbf{B}_*\Pi(\boldsymbol{\chi})}-e^{-\mathbf{B}_*\Pi(\boldsymbol{\chi})}}{e^{\mathbf{B}_*\Pi(\boldsymbol{\chi})}+e^{-\mathbf{B}_*\Pi(\boldsymbol{\chi})}}\right)^T\boldsymbol{\upsilon}\right]\cdot N^{-1}(\boldsymbol{\gamma}^k)_{1\times L}\right\}^T+ \\[2em] \text{function (THF)} & \left\{N^{-1}(\mathbf{B})^T_{L\times1}\cdot2\left[\mathbf{r}^k+\boldsymbol{\kappa}^k\right]^T\cdot N^{-1}\left(\mathbf{a}_*e^{\boldsymbol{\theta}\boldsymbol{\gamma}^k}\Pi(\boldsymbol{\chi})\cdot\left(\boldsymbol{\iota}-\left[\frac{e^{\mathbf{B}_*\Pi(\boldsymbol{\chi})}-e^{-\mathbf{B}_*\Pi(\boldsymbol{\chi})}}{e^{\mathbf{B}_*\Pi(\boldsymbol{\chi})}+e^{-\mathbf{B}_*\Pi(\boldsymbol{\chi})}}\right]^T\left[\frac{e^{\mathbf{B}_*\Pi(\boldsymbol{\chi})}-e^{-\mathbf{B}_*\Pi(\boldsymbol{\chi})}}{e^{\mathbf{B}_*\Pi(\boldsymbol{\chi})}+e^{-\mathbf{B}_*\Pi(\boldsymbol{\chi})}}\right]\right)\left[(\boldsymbol{\mu}^{*,s}_2)^{\frac{-1}{2}}\cdot\mathbf{w}_{\bullet,\bullet}\right]^T_{\Gamma\times1}\right)\left[\frac{L^{-1}}{\Delta\boldsymbol{\eta}^k}\right]^T_{1\times L}\cdot\Delta\boldsymbol{\eta}^k\right\} \end{cases} \tag{20b}$$

According to the derived order − relationship expressed in Equation (12) − (16) and
definition Equation

$$\approx \begin{cases} \text{1. Derivatives=0 for GLF} & \left\{2\left[\mathbf{r}^k+\boldsymbol{\kappa}^k\right]^T_{1\times M}\cdot N^{-1}\left[\left[(\boldsymbol{\mu}^{*,s}_2)^{\frac{-1}{2}}\cdot\mathbf{w}_{\bullet,\bullet}\right]_{1\times\Gamma}\boldsymbol{\theta}^T_{\Gamma\times1}\left[\frac{\partial P^k_{\text{sim}}}{\partial\boldsymbol{\eta}^k_{\bullet,\bullet,s}}\right]_{M\times L}\left[\Delta\boldsymbol{\eta}^k_{\bullet,\bullet,s}+\mathbf{c}^k_{\bullet,\bullet,s}\right]_{L\times1}\right]\left[(\boldsymbol{\gamma}^k_*-\mathbf{b}_*)\cdot\left[\frac{\Gamma^{-1}}{w_{i,j}}\right]^T\circ(\boldsymbol{\mu}^{*,s}_2)^{\frac{1}{2}}+\boldsymbol{\mu}^{*,s}_1\right]_{1\times L}\right\}^T+ \\[2em] & \left\{\left[(\mathbf{B}_*-\mathbf{b}_*)\cdot\left[\frac{\Gamma^{-1}}{w_{i,j}}\right]^T\circ(\boldsymbol{\mu}^{*,s}_2)^{\frac{1}{2}}+\boldsymbol{\mu}^{*,s}_1\right]^T_{L\times1}\cdot2\left[\mathbf{r}^k+\boldsymbol{\kappa}^k\right]^T\cdot N^{-1}\left(\mathbf{a}_*e^{\boldsymbol{\theta}\boldsymbol{\gamma}^k}\Pi(\boldsymbol{\chi})\cdot\left[\frac{\boldsymbol{\iota}}{\boldsymbol{\iota}+\boldsymbol{\alpha}_*e^{-\mathbf{B}_*}\Pi(\boldsymbol{\chi})}\right]^T\left[\frac{\boldsymbol{\alpha}_*e^{-\mathbf{B}_*}\Pi(\boldsymbol{\chi})}{\boldsymbol{\iota}+\boldsymbol{\alpha}_*e^{-\mathbf{B}_*}\Pi(\boldsymbol{\chi})}\right]\left[(\boldsymbol{\mu}^{*,s}_2)^{\frac{-1}{2}}\cdot\mathbf{w}_{\bullet,\bullet}\right]^T_{\Gamma\times1}\right)\left[\frac{L^{-1}}{\Delta\boldsymbol{\eta}^k}\right]^T_{1\times L}\right\}\cdot\Delta\boldsymbol{\eta}^k \\[2em] \text{2. Derivatives=0 for THF} & \left\{2\left[\mathbf{r}^k+\boldsymbol{\kappa}^k\right]^T_{1\times M}\cdot N^{-1}\left[\left[(\boldsymbol{\mu}^{*,s}_2)^{\frac{-1}{2}}\cdot\mathbf{w}_{\bullet,\bullet}\right]_{1\times\Gamma}\boldsymbol{\theta}^T_{\Gamma\times1}\left[\frac{\partial P^k_{\text{sim}}}{\partial\boldsymbol{\eta}^k_{\bullet,\bullet,s}}\right]_{M\times L}\left[\Delta\boldsymbol{\eta}^k_{\bullet,\bullet,s}+\mathbf{c}^k_{\bullet,\bullet,s}\right]_{L\times1}\right]\left[(\boldsymbol{\gamma}^k_*-\mathbf{b}_*)\cdot\left[\frac{\Gamma^{-1}}{w_{i,j}}\right]^T\circ(\boldsymbol{\mu}^{*,s}_2)^{\frac{1}{2}}+\boldsymbol{\mu}^{*,s}_1\right]_{1\times L}\right\}^T+ \\[2em] & \left\{\left[(\mathbf{B}_*-\mathbf{b}_*)\cdot\left[\frac{\Gamma^{-1}}{w_{i,j}}\right]^T\circ(\boldsymbol{\mu}^{*,s}_2)^{\frac{1}{2}}+\boldsymbol{\mu}^{*,s}_1\right]^T_{L\times1}\cdot2\left[\mathbf{r}^k+\boldsymbol{\kappa}^k\right]^T\cdot N^{-1}\left(\mathbf{a}_*e^{\boldsymbol{\theta}\boldsymbol{\gamma}^k}\Pi(\boldsymbol{\chi})\cdot\left(\boldsymbol{\iota}-\left[\frac{e^{\mathbf{B}\Pi(\boldsymbol{\chi})}-e^{-\mathbf{B}\Pi(\boldsymbol{\chi})}}{e^{\mathbf{B}\Pi(\boldsymbol{\chi})}+e^{-\mathbf{B}\Pi(\boldsymbol{\chi})}}\right]^T\left[\frac{e^{\mathbf{B}\Pi(\boldsymbol{\chi})}-e^{-\mathbf{B}\Pi(\boldsymbol{\chi})}}{e^{\mathbf{B}\Pi(\boldsymbol{\chi})}+e^{-\mathbf{B}\Pi(\boldsymbol{\chi})}}\right]\right)\left[(\boldsymbol{\mu}^{*,s}_2)^{\frac{-1}{2}}\cdot\mathbf{w}_{\bullet,\bullet}\right]^T_{\Gamma\times1}\right)\left[\frac{L^{-1}}{\Delta\boldsymbol{\eta}^k}\right]^T_{1\times L}\right\}\cdot\Delta\boldsymbol{\eta}^k \end{cases} \tag{21}$$

Derive
conditional constraints to compute correction vector and Hessian matrix of optimized parameter $\boldsymbol{\eta}^k$ by comparing Eq.(3a) with Eq.(21)

$$\Rightarrow \quad s.t. \begin{cases} \text{All conditions:} & \left[\boldsymbol{\kappa}^k\right]^T_{1\times M}=\left\{N^{-1}\left[P_{\text{sim}}(\Pi(\boldsymbol{\eta}^k),\bullet)\right]\left[\frac{1}{\chi^i_{t,s}-\eta^k_{i,t,s}}\right]^T\Delta\boldsymbol{\eta}^{k^-}+\frac{1}{2}(\Delta\boldsymbol{\eta}^k)^T\left[\frac{1}{\Delta\eta^{k^-}_{i,t,s}+c^k_{i,t,s}}\right]N^{-1}\left[P_{\text{sim}}(\Pi(\boldsymbol{\eta}^k),\bullet)\right]\left[\frac{1}{\Delta\eta^{k^-}_{i,t,s}+c^k_{i,t,s}}\right]^T\Delta\boldsymbol{\eta}^{k^-}\right\}^T_{1\times M}\approx[0,0,\ldots,0]_{1\times M} \\[2em] \text{All conditions:} & N^{-1}\left[\left[(\boldsymbol{\mu}^{*,s}_2)^{\frac{-1}{2}}\cdot\mathbf{w}_{\bullet,\bullet}\right]_{1\times\Gamma}\boldsymbol{\theta}^T_{\Gamma\times1}\cdot\left[\Delta\boldsymbol{\eta}^{k^-}_{\bullet,\bullet,s}+\mathbf{c}^k_{\bullet,\bullet,s}\right]_{L\times1}\right]\left[(\boldsymbol{\gamma}^k_*-\mathbf{b}_*)\cdot\left[\frac{\Gamma^{-1}}{w_{i,j}}\right]^T\circ(\boldsymbol{\mu}^{*,s}_2)^{\frac{1}{2}}+\boldsymbol{\mu}^{*,s}_1\right]_{1\times L}\approx\begin{bmatrix}1&\cdots&1\\\vdots&\ddots&\vdots\\1&\cdots&1\end{bmatrix}_{1\times L} \\[2em] \text{For GLF:} & \left[(\mathbf{B}_*-\mathbf{b}_*)\cdot\left[\frac{\Gamma^{-1}}{w_{i,j}}\right]^T\circ(\boldsymbol{\mu}^{*,s}_2)^{\frac{1}{2}}+\boldsymbol{\mu}^{*,s}_1\right]^T_{L\times1}\cdot2\left[\mathbf{r}^k+\boldsymbol{\kappa}^k\right]^T\cdot N^{-1}\left(\mathbf{a}_*e^{\boldsymbol{\theta}\boldsymbol{\gamma}^k}\Pi(\boldsymbol{\chi})\cdot\left[\frac{\boldsymbol{\iota}}{\boldsymbol{\iota}+\boldsymbol{\alpha}_*e^{-\mathbf{B}_*}\Pi(\boldsymbol{\chi})}\right]^T\left[\frac{\boldsymbol{\alpha}_*e^{-\mathbf{B}_*}\Pi(\boldsymbol{\chi})}{\boldsymbol{\iota}+\boldsymbol{\alpha}_*e^{-\mathbf{B}_*}\Pi(\boldsymbol{\chi})}\right]\left[(\boldsymbol{\mu}^{*,s}_2)^{\frac{-1}{2}}\cdot\mathbf{w}_{\bullet,\bullet}\right]^T_{\Gamma\times1}\right)\left[\frac{L^{-1}}{\Delta\boldsymbol{\eta}^{k^-}}\right]^T_{1\times L}=\mathbf{H}(\boldsymbol{\eta}^k) \\[2em] \text{For THF:} & \left[(\mathbf{B}_*-\mathbf{b}_*)\left[\frac{\Gamma^{-1}}{w_{i,j}}\right]^T\circ(\boldsymbol{\mu}^{*,s}_2)^{\frac{1}{2}}+\boldsymbol{\mu}^{*,s}_1\right]^T_{L\times1}\cdot2\left[\mathbf{r}^k+\boldsymbol{\kappa}^k\right]^T\cdot N^{-1}\left(\mathbf{a}e^{\boldsymbol{\theta}\boldsymbol{\gamma}^k}\Pi(\boldsymbol{\chi})\cdot\left(\boldsymbol{\iota}-\left[\frac{e^{\mathbf{B}\Pi(\boldsymbol{\chi})}-e^{-\mathbf{B}\Pi(\boldsymbol{\chi})}}{e^{\mathbf{B}\Pi(\boldsymbol{\chi})}+e^{-\mathbf{B}\Pi(\boldsymbol{\chi})}}\right]^T\left[\frac{e^{\mathbf{B}\Pi(\boldsymbol{\chi})}-e^{-\mathbf{B}\Pi(\boldsymbol{\chi})}}{e^{\mathbf{B}\Pi(\boldsymbol{\chi})}+e^{-\mathbf{B}\Pi(\boldsymbol{\chi})}}\right]\right)\left[(\boldsymbol{\mu}^{*,s}_2)^{\frac{-1}{2}}\cdot\mathbf{w}_{\bullet,\bullet}\right]^T_{\Gamma\times1}\right)\left[\frac{L^{-1}}{\Delta\boldsymbol{\eta}^{k^-}}\right]^T_{1\times L}=\mathbf{H}(\boldsymbol{\eta}^k) \end{cases} \tag{22}$$

where $\overline{\Delta\boldsymbol{\eta}}$ in equation (18) is the parameter correction vector after first- and second-order moment nonlinear normalization, and its calculation is shown in equation (23); the permutated calculation methods of matrices $\left[\frac{1}{\chi^i_{t,s}-\eta^k_{i,t,s}}\right]^T_{1\times L}$ and $\left[\frac{1}{\Delta\eta^k_{i,t,s}+c^k_{i,t,s}}\right]^T_{1\times L}$ in equation (19) are expressed in equation (22); $[\mathbf{r}^k]^T_{1\times M}$ in equations (20)–(22) is the spatiotemporal permutated matrix of simulated rainfall error, and its calculation algebra is expressed in equation (23); equation (23) sets the total percentage of rain-generated capacity $\mathbf{K}_*$ after inputting each rain-making causal observation into the model with dimensionality-reduced spatiotemporal feature element ($* = j = 1 \sim \Gamma$) as matrix $\boldsymbol{\iota}$ composed of $1 = 100\%$; $N^{-1}\{\mathbf{B}_*\}_{1\times L}$ and $N^{-1}(\boldsymbol{\gamma}^k_*)_{1\times L}$ in equations (20) and (21) are computational algebraic matrices of the component element parameters of the model input after dimensionality-reduced projection, de-linearization, and de-normalization, as shown in equation (23); and the layout calculation methods of $\left[\frac{\Gamma^{-1}}{w_{ij}}\right]^T_{\Gamma\times\Gamma}$ and $\left[\frac{L^{-1}}{\Delta\boldsymbol{\eta}^k}\right]^T_{1\times L}$ in equations (20)–(23) are expressed in equation (23).

$$
\left\{
\begin{aligned}
&\overline{\Delta\boldsymbol{\eta}} = \left| \frac{\Delta\boldsymbol{\eta}^k_{\bullet,t,s} - \boldsymbol{\mu}^{\bullet,s}_1}{\left(\boldsymbol{\mu}^{\bullet,s}_2\right)^{\frac{1}{2}}} \quad \frac{\Delta\boldsymbol{\eta}^k_{\bullet,t,s} - \mathrm{E}_t\left[\Delta\boldsymbol{\eta}^k_{\bullet,t,s}\right]}{\left(\mathrm{E}_t\left[(\Delta\boldsymbol{\eta}^k_{\bullet,t,s} - \boldsymbol{\mu}^{\bullet,s}_1)^2\right]\right)^{\frac{1}{2}}} \quad \left| \begin{aligned} \boldsymbol{\mu}^{\bullet,s}_2 &\equiv \boldsymbol{\sigma}^2 \equiv \mathrm{E}_t\left[(\Delta\boldsymbol{\eta}^k_{\bullet,t,s} - \boldsymbol{\mu}^{\bullet,s}_1)^2\right] \\ \boldsymbol{\mu}^{\bullet,s}_1 &\equiv \mathrm{E}_t\left[\Delta\boldsymbol{\eta}^k_{\bullet,t,s}\right] \end{aligned} \right. \right|\\[4pt]
&\left[\frac{1}{\chi^t_{l,t,s} - \eta^k_{l,t,s}}\right]^{\mathrm{T}}_{1\times L} = \left[\frac{1}{\chi^1_{1,s} - \eta^k_{1,1,s}} \quad \frac{1}{\chi^2_{1,s} - \eta^k_{2,1,s}} \cdots \frac{1}{\chi^\Upsilon_{1,s} - \eta^k_{\Upsilon,1,s}} \cdots \frac{1}{\chi^1_{t,s} - \eta^k_{1,t,s}} \quad \frac{1}{\chi^2_{t,s} - \eta^k_{2,t,s}} \cdots \frac{1}{\chi^\Upsilon_{t,s} - \eta^k_{\Upsilon,t,s}} \cdots \frac{1}{\chi^1_{T,s} - \eta^k_{1,T,s}} \cdots \frac{1}{\chi^\Upsilon_{T,s} - \eta^k_{\Upsilon,T,s}}\right]^{l=1\sim T}\\[4pt]
&\left[\frac{1}{\Delta\eta^k_{l,t,s} + c^k_{l,t,s}}\right]^{\mathrm{T}}_{1\times L} = \left[\frac{1}{\Delta\eta^k_{1,1,s} + c^k_{1,1,s}} \quad \frac{1}{\Delta\eta^k_{2,1,s} + c^k_{2,1,s}} \cdots \frac{1}{\Delta\eta^k_{\Upsilon,1,s} + c^k_{\Upsilon,1,s}} \cdots \frac{1}{\Delta\eta^k_{1,t,s} + c^k_{1,t,s}} \quad \frac{1}{\Delta\eta^k_{2,t,s} + c^k_{2,t,s}} \cdots \frac{1}{\Delta\eta^k_{\Upsilon,t,s} + c^k_{\Upsilon,t,s}} \cdots \frac{1}{\Delta\eta^k_{1,T,s} + c^k_{1,T,s}} \cdots \frac{1}{\Delta\eta^k_{\Upsilon,T,s} + c^k_{\Upsilon,T,s}}\right]\\[4pt]
&\left[\mathbf{r}^k\right]^{\mathrm{T}}_{1\times M} = N^{-1}\left\{P_{\mathrm{sim}}\left(\Pi(\boldsymbol{\eta}^k),\bullet\right)\right\} - P_{\mathrm{obs}}\\[4pt]
&\mathbf{K}_{\bullet} = \boldsymbol{\iota} = [1,1,\dots,1]_{1\times\Gamma}\\[4pt]
&N^{-1}\{\mathbf{B}_{\bullet}\}_{1\times L} = (\mathbf{B}_{\bullet} - \mathbf{b}_{\bullet}) \circ \left[\frac{\Gamma^{-1}}{w_{i,j}}\right]^{\mathrm{T}} \circ \left(\boldsymbol{\mu}^{\bullet,s}_2\right)^{\frac{1}{2}} + \boldsymbol{\mu}^{\bullet,s}_1 \Big|^{L=\Upsilon\cdot T\cdot S}, \quad N^{-1}\{\boldsymbol{\gamma}^k_{\bullet}\}_{1\times L} = (\boldsymbol{\gamma}^k_{\bullet} - \mathbf{b}_{\bullet}) \circ \left[\frac{\Gamma^{-1}}{w_{i,j}}\right]^{\mathrm{T}} \circ \left(\boldsymbol{\mu}^{\bullet,s}_2\right)^{\frac{1}{2}} + \boldsymbol{\mu}^{\bullet,s}_1\\[4pt]
&\left[\frac{\Gamma^{-1}}{w_{i,j}}\right]^{\mathrm{T}}_{\Gamma\times\Upsilon} = \begin{bmatrix} 1/w_{1,1}\Gamma & \cdots & 1/w_{\Upsilon,1}\Gamma \\ \vdots & \ddots & \vdots \\ 1/w_{1,\Gamma}\Gamma & \cdots & 1/w_{\Upsilon,\Gamma}\Gamma \end{bmatrix}\\[4pt]
&\left[\frac{L^{-1}}{\Delta\boldsymbol{\eta}^k}\right]^{\mathrm{T}}_{1\times L} = \left[\frac{1}{\Delta\eta^k_{1,1,s}L} \quad \frac{1}{\Delta\eta^k_{2,1,s}L} \cdots \frac{1}{\Delta\eta^k_{\Upsilon,1,s}L} \cdots \frac{1}{\Delta\eta^k_{1,t,s}L} \quad \frac{1}{\Delta\eta^k_{2,t,s}L} \cdots \frac{1}{\Delta\eta^k_{\Upsilon,t,s}L} \cdots \frac{1}{\Delta\eta^k_{1,T,s}L} \cdots \frac{1}{\Delta\eta^k_{\Upsilon,T,s}L}\right]
\end{aligned}
\right.
$$

(23)

In equations (17)–(22), the designed key–lock quasi-Newton optimizing approach is used to derive the Hessian matrix $\mathbf{H}(\boldsymbol{\eta}^k)$ of the rain-generating simulated LSE as the advanced functional analytic solution composited by logic or tangent hyperbolic functions, in which terms $2[\mathbf{r}^k + \boldsymbol{\kappa}^k]^{\mathrm{T}}$, $\left[\frac{\boldsymbol{\iota}}{1 + \boldsymbol{\alpha}_{\bullet} e^{-\mathbf{B}_{\bullet}\Pi(\boldsymbol{\chi})}}\right]^{\mathrm{T}} \cdot \left[\frac{\boldsymbol{\alpha}_{\bullet} e^{-\mathbf{B}_{\bullet}\Pi(\boldsymbol{\chi})}}{1 + \boldsymbol{\alpha}_{\bullet} e^{-\mathbf{B}_{\bullet}\Pi(\boldsymbol{\chi})}}\right]$, $\boldsymbol{\iota} - \left[\frac{e^{\mathbf{B}\Pi(\boldsymbol{\chi})} - e^{-\mathbf{B}\Pi(\boldsymbol{\chi})}}{e^{\mathbf{B}\Pi(\boldsymbol{\chi})} + e^{-\mathbf{B}\Pi(\boldsymbol{\chi})}}\right]^{\mathrm{T}}\left[\frac{e^{\mathbf{B}\Pi(\boldsymbol{\chi})} - e^{-\mathbf{B}\Pi(\boldsymbol{\chi})}}{e^{\mathbf{B}\Pi(\boldsymbol{\chi})} + e^{-\mathbf{B}\Pi(\boldsymbol{\chi})}}\right]$, $(\mathbf{B}_{\bullet} - \mathbf{b}_{\bullet}) \cdot \left[\frac{\Gamma^{-1}}{w_{i,j}}\right]^{\mathrm{T}}$, and $\left[\frac{L^{-1}}{\Delta\boldsymbol{\eta}^k}\right]^{\mathrm{T}}_{1\times L}$ are derived to calculate the second-order derivative of the objective function and combined with term $\mathbf{a}_{\bullet} e^{\boldsymbol{\theta}\boldsymbol{\gamma}^k\Pi(\boldsymbol{\chi})}_{\mathrm{Mx}\Gamma}$ to remove the atmospheric rain-generating error caused by an over-estimated Hessian from the Jacobian matrix inter-product in the conventional quasi-Newtons. The sum structure of the derived advanced high-order functional analytical solution $\mathbf{H}(\boldsymbol{\eta}^k)$ in equation (22) is a symmetric rank-four matrix.

To accelerate convergence and escape from the local minimum, this study uses the vectorized limited switchable step size $\boldsymbol{\alpha}^k = [\alpha^k_l|_{l=1\sim L}]$ to inversely identify the rain-making threshold and induced precipitation generated by various atmospheric causes at each time and observation station. To solve the problem that the sensitivity matrix used by the conventional quasi-Newton to approximate the Hessian (e.g., $\mathbf{H} \approx 2\mathbf{J}^{\mathrm{T}}_{\mathrm{D}}\mathbf{J}_{\mathrm{D}}$) often overestimates $\left|r_m\frac{\partial^2 r_m}{\partial\eta_i\partial\eta_j}\right| \ll \left|\frac{\partial r_m}{\partial\eta_i}\frac{\partial r_m}{\partial\eta_j}\right|$ for accurate calculation $\left|r_m\frac{\partial^2 r_m}{\partial\eta_i\partial\eta_j}\right| =$

$$
\left| \left[(\mathbf{B} - \mathbf{b}) \cdot \left[\frac{\Gamma^{-1}}{w}\right]^{\mathrm{T}} \circ (\boldsymbol{\mu}_2)^{\frac{1}{2}} + \boldsymbol{\mu}_1\right]^{\mathrm{T}}_{L\times 1} \cdot 2[\mathbf{r}^k + \boldsymbol{\kappa}^k]^{\mathrm{T}} \cdot N^{-1}\left(\mathbf{a}e^{\boldsymbol{\theta}\boldsymbol{\gamma}^k\Pi(\boldsymbol{\chi})}_{\mathrm{Mx}\Gamma} \cdot \left[\frac{\boldsymbol{\iota}}{\boldsymbol{\iota} + \boldsymbol{\alpha}e^{-\mathbf{B}\Pi(\boldsymbol{\chi})}}\right]^{\mathrm{T}} \cdot \left[\frac{\boldsymbol{\alpha}e^{-\mathbf{B}\Pi(\boldsymbol{\chi})}}{\boldsymbol{\iota} + \boldsymbol{\alpha}e^{-\mathbf{B}\Pi(\boldsymbol{\chi})}}\right] \cdot \left[(\boldsymbol{\mu}_2)^{\frac{-1}{2}} \cdot \mathbf{w}\right]^{\mathrm{T}}_{\Gamma\times 1}\right) \cdot \left[\frac{L^{-1}}{\Delta\boldsymbol{\eta}^{k-}}\right]^{\mathrm{T}}_{1\times L} \cup \right.
$$

$$
\left. \left[(\mathbf{B} - \mathbf{b})\left[\frac{\Gamma^{-1}}{w}\right]^{\mathrm{T}} \circ (\boldsymbol{\mu}_2)^{\frac{1}{2}} + \boldsymbol{\mu}_1\right]^{\mathrm{T}}_{L\times 1} \cdot 2[\mathbf{r}^k + \boldsymbol{\kappa}^k]^{\mathrm{T}} \cdot N^{-1}\left(\mathbf{a}e^{\boldsymbol{\theta}\boldsymbol{\gamma}^k\Pi(\boldsymbol{\chi})}_{\mathrm{Mx}\Gamma} \cdot \left(\boldsymbol{\iota} - \left[\frac{e^{\mathbf{B}\Pi(\boldsymbol{\chi})} - e^{-\mathbf{B}\Pi(\boldsymbol{\chi})}}{e^{\mathbf{B}\Pi(\boldsymbol{\chi})} + e^{-\mathbf{B}\Pi(\boldsymbol{\chi})}}\right]^{\mathrm{T}}\left[\frac{e^{\mathbf{B}\Pi(\boldsymbol{\chi})} - e^{-\mathbf{B}\Pi(\boldsymbol{\chi})}}{e^{\mathbf{B}\Pi(\boldsymbol{\chi})} + e^{-\mathbf{B}\Pi(\boldsymbol{\chi})}}\right]\right) \cdot \left[(\boldsymbol{\mu}_2)^{\frac{-1}{2}} \cdot \mathbf{w}\right]^{\mathrm{T}}_{\Gamma\times 1}\right) \cdot \left[\frac{L^{-1}}{\Delta\boldsymbol{\eta}^{k-}}\right]^{\mathrm{T}}_{1\times L} \right|
$$

$= \left|\mathbf{H}(\boldsymbol{\eta}^k, \Delta\boldsymbol{\eta}^{k-})\right|$, detect and approach the global optimum solution, and solve nonlinear ill-posed problems, this study describes a rain-generating simulator using composite tangent hyperbolic and logistic functions as high-order continuous differentiable functions, coupled with the designed key–lock quasi-Newton optimizing approach [equations (17)–(22)] for deriving the analytical solution of multi-order derivatives for a typhoon's rainfall causal decomposition. This design can not only effectively calculate an accurate, positive definite, and numerically stable Hessian in equation (22) and parameter correction in equation (22) but also overcome the approximate overestimated problems, high computational cost, and slow convergence, only to the local minimum, and difficulty in meeting the curvature secant conditions in Jacobian, LMA, and BFGS quasi-Newtons by introducing a multi-order derivative approaching structure and solving the constrained nonlinear parameter optimization problem.

$$
\Delta\boldsymbol{\eta}^{k+} = \boldsymbol{\eta}^{k+1} - \boldsymbol{\eta}^k = -\boldsymbol{\alpha}^{k+} \circ \left\{\left[\mathbf{H}(\boldsymbol{\eta}^k, \Delta\boldsymbol{\eta}^{k-})\right]^{-1} \cdot \left(\mathbf{J}^{\mathrm{T}}_{\mathrm{D}}\right)^k \cdot \mathbf{r}(\boldsymbol{\eta}^k)\right\}, k \in \mathbb{N} \tag{24}
$$

Equations (22) are the derived constraints that satisfy Newton's equational conditions, in which the candidate solutions $\Delta\boldsymbol{\eta}^{k-}$ of 1~4 sets of parameter correction vectors can be solved using equation (23a), and equation (22) can solve one set of candidate solutions $\Delta\boldsymbol{\eta}^{k-}$. Since the higher-order term (HOT) when using Taylor expansion to approximate $J_{\mathrm{T}}(P_{\mathrm{sim}}(\boldsymbol{\eta}^{k+1}, \boldsymbol{\chi}), P_{\mathrm{obs}})$ or $P^{\mathrm{TE}}_{\mathrm{sim}}(\boldsymbol{\eta}^{k+1}, \boldsymbol{\chi})$ can be omitted, the relationship between simulated precipitation $P_{\mathrm{sim}}(\Pi(\boldsymbol{\eta}^k), \cdot)$ and its derivative $P'_{\mathrm{sim}}(\Pi(\boldsymbol{\eta}^k), \cdot) = \frac{dP_{\mathrm{sim}}(\Pi(\boldsymbol{\eta}^k), \cdot)}{d\boldsymbol{\eta}^k}$ derived using the composite function has some error at the incipient iteration, and the identified simulation model parameters $(\mathbf{w}、\boldsymbol{\theta}、\mathbf{a}、\boldsymbol{\gamma}、\boldsymbol{\alpha}、\mathbf{B}、\boldsymbol{\gamma})$ based on the typhoon's atmospheric rain-making observation data has uncertainty; thus, the candidate solution $\Delta\boldsymbol{\eta}^{k-,\omega}$ solved by mass conservation equation (22) after substituting into equation (22) may not be completely subject to the valued square matrix condition $\begin{bmatrix} 1 & \cdots & 1 \\ \vdots & \ddots & \vdots \\ 1 & \cdots & 1 \end{bmatrix}$ but only to the approximate state. The candidate solution $\Delta\boldsymbol{\eta}^{k-,\varepsilon}$ solved by the energy conservation equation (22) after

substituting into equation (22) may not be completely equal to the state of $[0, 0, ..., 0]$. The candidate solution that is approximately subject to the conditional constraints in equations (22), $\Delta \boldsymbol{\eta}^{k^-} \in \left\{ \Delta \boldsymbol{\eta}^{k^-,\omega}, \Delta \boldsymbol{\eta}^{k^-,\varepsilon} \middle| \begin{matrix} \omega = 1 \sim 4 \\ \varepsilon = 1 \end{matrix} \right\}$, (key) is acceptable to enter equations (22) or (22) for calculating the Hessian analytic matrix $\mathbf{H}(\boldsymbol{\eta}^k, \Delta \boldsymbol{\eta}^{k^-})$ (lock) presented as an advanced function and subsequently in equation (30) for calculating the relationship equation between the optimized parameter correction vector/direction and referenced step size vector $\Delta \boldsymbol{\eta}^{k^-} = -\boldsymbol{\alpha}^{k^-} \circ \{ [\mathbf{H}(\boldsymbol{\eta}^k, \Delta \boldsymbol{\eta}^{k^-})]^{-1} \cdot (\mathbf{J}_D^{\mathrm{T}})^k \cdot \mathbf{r}(\boldsymbol{\eta}^k) \}$, including Taylor expansion error, derivative approximation error, and model parameter uncertainty. Therefore, up to five sets of referenced step size vectors $\boldsymbol{\alpha}^{k^-} \in \left\{ \boldsymbol{\alpha}^{k^-,\omega}, \boldsymbol{\alpha}^{k^-,\varepsilon} \middle| \begin{matrix} \omega = 1 \sim 4 \\ \varepsilon = 1 \end{matrix} \right\} = [\alpha_l^{k^-,\omega}, \alpha_l^{k^-,\varepsilon}|_{l=1 \sim L}]$ can be solved using entry-wise division between $\Delta \boldsymbol{\eta}^{k^-}$ and $\{ [\mathbf{H}(\boldsymbol{\eta}^k, \Delta \boldsymbol{\eta}^{k^-})]^{-1} \cdot (\mathbf{J}_D^{\mathrm{T}})^k \cdot \mathbf{r}(\boldsymbol{\eta}^k) \}$. According to the combination of inversely calculated referenced step size vector $\boldsymbol{\alpha}^{k^-}$, the maximum and minimum step sizes ($\boldsymbol{\alpha}_{\mathrm{UB}}^{k,\kappa} = [\alpha_{\mathrm{UB},l}^{k,\kappa}] = Max\left\{ \boldsymbol{\alpha}^{k^-,\omega}\left(\boldsymbol{\iota} + 3(\boldsymbol{\mu}_2)^{\frac{1}{2}}\right), \boldsymbol{\alpha}^{k^-,\varepsilon}\left(\boldsymbol{\iota} + 3(\boldsymbol{\mu}_2)^{\frac{1}{2}}\right) \right\}$ and $\boldsymbol{\alpha}_{\mathrm{LB}}^{k,\kappa} = Min\left\{ \boldsymbol{\alpha}^{k^-,\omega}\left(\boldsymbol{\iota} - 3(\boldsymbol{\mu}_2)^{\frac{1}{2}}\right), \boldsymbol{\alpha}^{k^-,\varepsilon}\left(\boldsymbol{\iota} - 3(\boldsymbol{\mu}_2)^{\frac{1}{2}}\right) \right\}$) that approximately satisfies Newton's conditional equations (22) and (22) can be estimated to efficiently identify the optimal vectorized step size $\boldsymbol{\alpha}^{k^+}$ (described in section 2.6) and the corresponding optimal parameter correction vector $\Delta \boldsymbol{\eta}^{k^+}$ calculated using equation (24), where $\pm 3(\boldsymbol{\mu}_2)^{\frac{1}{2}}$ is the normalized independent variable anomaly of the sample's cumulative probability density equaling 99 % in a standard normal distribution.

2.6. Vectorized step size optimization using key–lock quasi-Newton analytical solved advanced functional double-bracketing approach

This study identifies the typhoon's rain-generating threshold and the produced precipitation by individual rain-making causes using a designed key–lock quasi-Newton optimizing approach with vectorized limited switchable step size corresponding to various atmospheric rain-making parameters. To adjust the searching direction, scale the correction vector, accelerate convergence, reduce the difference among heterogeneous parameters, and achieve a small error in the estimated parameter $\boldsymbol{\eta}^{k+1}$ and rapid convergence of the objective function $J(P_{\mathrm{sim}}(\boldsymbol{\eta}^{k+1}, \cdot), P_{\mathrm{obs}})$, this study proposes the key–lock quasi-Newton analytical derivation to solve the candidate solution $\Delta \boldsymbol{\eta}^{k^-}$ and the referenced step size $\boldsymbol{\alpha}^{k^-}$ using an advanced functional multi-order-derivative precise double-bracketing approach, which can ensure convergence and determine the vectorized step size.

For more complex vectorized step size root-finding problems, the double-bracketing false-position approach, which typically only determines a scalar step size but can ensure convergence [40], is re-written in the following algebraic form: determine $\boldsymbol{\alpha}^k \in [\boldsymbol{\alpha}_+^{k,\kappa}|_{\kappa=1 \sim \Sigma}]$ during iterations κ such that $J'(\cdot, \boldsymbol{\alpha}_+^{k,\kappa}) = 0$ and the known conditions are $J'(\cdot, \boldsymbol{\alpha}_{\mathrm{LB}}^{k,\kappa}) = \mathbf{b_1}$ and $J'(\cdot, \boldsymbol{\alpha}_{\mathrm{UB}}^{k,\kappa}) = \mathbf{b_2}$. If $J'(\cdot, \boldsymbol{\alpha}_+^{k,\kappa})$ is a non-linear continuous function and there are two vectors $\boldsymbol{\alpha}_{\mathrm{LB}}^{k,\kappa}$ and $\boldsymbol{\alpha}_{\mathrm{UB}}^{k,\kappa}$ such that each corresponding element of $J'(\cdot, \boldsymbol{\alpha}_{\mathrm{LB}}^{k,\kappa})$ and $J'(\cdot, \boldsymbol{\alpha}_{\mathrm{UB}}^{k,\kappa})$ has opposite signs, then according to the intermediate value theorem, the function $J'(\cdot, \boldsymbol{\alpha}_+^{k,\kappa})$ has the root $\boldsymbol{\alpha}_+^{k,\kappa}$ in the interval $[\boldsymbol{\alpha}_{\mathrm{LB}}^{k,\kappa}, \boldsymbol{\alpha}_{\mathrm{UB}}^{k,\kappa}]$. The vectorized bisection, Illinois, and Anderson–Björk algorithms use the systematic technique $\mathbf{m_p}$ to calculate the midpoint vector $\boldsymbol{\alpha}_{\mathrm{MP}}^{k,\kappa}$ to approach $\boldsymbol{\alpha}_+^{k,\kappa}$, as shown in equations (25), respectively. If $J'(\boldsymbol{\alpha}_{\mathrm{MP}}^{k,\kappa})$ has the same sign as $J'(\boldsymbol{\alpha}_{\mathrm{UB}}^{k,\kappa})$, the new bracketing interval is updated to $[\boldsymbol{\alpha}_{\mathrm{LB}}^{k,\kappa+1}, \boldsymbol{\alpha}_{\mathrm{UB}}^{k,\kappa+1}] = [\boldsymbol{\alpha}_{\mathrm{LB}}^{k,\kappa}, \boldsymbol{\alpha}_{\mathrm{MP}}^{k,\kappa}]$. This study modifies the traditional scalar double-bracketing method using the multi-order derivatives of the objective function and the analytically derived reference step size distributions satisfying Newton's conditions to calculate the halving shrinkage vector $\mathbf{m}$ and bracketing step size midpoint vector $\boldsymbol{\alpha}_{\mathrm{MP}}^{k,\kappa} = [\alpha_{\mathrm{MP},l}^{k,\kappa}|_{l=1 \sim L}]$, as shown in equation (25).

$$\alpha_{\text{MP},l}^{k,\kappa} = \frac{\zeta_l \cdot \left[\boldsymbol{\alpha}_{\text{LB}}^{k,\kappa} \circ \nabla J\left(\cdot, \boldsymbol{\alpha}_{\text{UB}}^{k,\kappa}\right) - \mathbf{m_p} \circ \boldsymbol{\alpha}_{\text{UB}}^{k,\kappa} \circ \nabla J\left(\cdot, \boldsymbol{\alpha}_{\text{LB}}^{k,\kappa}\right)\right]}{\zeta_l \cdot \left[\nabla J\left(\cdot, \boldsymbol{\alpha}_{\text{UB}}^{k,\kappa}\right) - \mathbf{m_p} \circ \nabla J\left(\cdot, \boldsymbol{\alpha}_{\text{LB}}^{k,\kappa}\right)\right]}$$

Vectorized Illinois

$$\text{Vectorized false} - \text{position method}: \mathbf{m_1} = \begin{bmatrix} 1 \\ \vdots \\ 1 \end{bmatrix}_{L \times 1}, \quad \text{algorithm}: \mathbf{m_2} = \begin{bmatrix} 1/2 \\ \vdots \\ 1/2 \end{bmatrix}_{L \times 1}$$

Vectorized Anderson − Bjork

$$\text{algorithm}: \mathbf{m_3} = \begin{bmatrix} 1 - \dfrac{\zeta_1 \cdot \nabla J\left(\cdot, \boldsymbol{\alpha}_{\text{MP}}^{k,\kappa}\right)}{\zeta_1 \cdot \nabla J\left(\cdot, \boldsymbol{\alpha}_{\text{UB}}^{k,\kappa}\right)} \\ \vdots \\ 1 - \dfrac{\zeta_L \cdot \nabla J\left(\cdot, \boldsymbol{\alpha}_{\text{MP}}^{k,\kappa}\right)}{\zeta_L \cdot \nabla J\left(\cdot, \boldsymbol{\alpha}_{\text{UB}}^{k,\kappa}\right)} \end{bmatrix}_{L \times 1} \quad if \quad m > 0, \quad \mathbf{m_3} = \begin{bmatrix} 1/2 \\ \vdots \\ 1/2 \end{bmatrix}_{L \times 1} \quad else \tag{25}$$

Proposed key − lock shaping quasi − Newton analytical derivation − based vectorized double false − position method :

$$\mathbf{m_4} = \frac{J\left(\boldsymbol{\eta}^k, \boldsymbol{\alpha}_{\text{LB}}^{k,\kappa}\right)}{J\left(\boldsymbol{\eta}^k, \boldsymbol{\alpha}_{\text{UB}}^{k,\kappa}\right)} \cdot \begin{bmatrix} 1 \\ \vdots \\ 1 \end{bmatrix}_{L \times 1}, \mathbf{m_5} = \begin{bmatrix} \varpi_1 \\ \vdots \\ \varpi_l \\ \vdots \\ \varpi_L \end{bmatrix}_{L \times 1}, \varpi_l \in \left[\frac{\alpha_l^{k^-,\omega}}{\alpha_{\text{UB},l}^{k,\kappa}}, \frac{\alpha_l^{k^-,\varepsilon}}{\alpha_{\text{UB},l}^{k,\kappa}}, 1/2, 1\right]$$

where ζ_l is the lth unit vector; $\mathbf{m_1}$, $\mathbf{m_2}$, and $\mathbf{m_3}$ are the halving vectors of the vectorized traditional double-bracketing false-position approach, Illinois algorithm, and Anderson–Björk algorithm, respectively; $\mathbf{m_4}$ is the halving vector of the zero-order derivative double-bracketing approach; $\mathbf{m_5}$ is the proposed double-bracketing halving vector based on the referenced step size distributions

2.7. Dimensional reduction and characterization of rain-making causes and feature components

This study considers the swarm composite rain-generating function of 11 types of atmospheric rain-making causes to simulate the spatiotemporal patterns of typhoon precipitation. To characterize the causal rain-generating mechanisms and feature components, this study uses multi-rank loading scores of rainfall spatiotemporal patterns calculated through SVD to project the various rain-making observations into the dimension-reduced component/classification j (* $\rightarrow j = 1 \sim \Gamma$) and to establish the precipitation simulator under interactive response using the devised composite function ($\left[\mathbf{a}_* \circ e_{\text{M} \times \Gamma}^{\boldsymbol{\theta}_* \circ \boldsymbol{\gamma}_*^k \circ \Pi(\boldsymbol{\chi}^k)} \cdot \left(\frac{\mathbf{K}_*}{\mathbf{1} + \boldsymbol{\alpha}_* \circ e^{-\mathbf{B}_* \circ \Pi(\boldsymbol{\chi}^k)}}\right)_{\Gamma \times M}^{\text{T}}\right]$ or $\mathbf{a}_* e^{\boldsymbol{\theta}_* \circ \boldsymbol{\gamma}_*^k \Pi(\boldsymbol{\chi}^k)} \cdot \left(\frac{\mathbf{B}_* e^{\Pi(\boldsymbol{\chi}^k)} - \mathbf{B}_* e^{-\Pi(\boldsymbol{\chi}^k)}}{\mathbf{B}_* e^{\Pi(\boldsymbol{\chi}^k)} + \mathbf{B}_* e^{-\Pi(\boldsymbol{\chi}^k)}}\right)^{\text{T}}$). Extending equation (24), $\Delta \boldsymbol{\eta}^{k^+} = -\boldsymbol{\alpha}^{k^+} \circ \left\{[\mathbf{H}(J(P^{\text{sim}}(\boldsymbol{\eta}^k), P^{\text{obs}}), \Delta \boldsymbol{\eta}^{k^-})]^{-1} \cdot \left(\frac{\partial P^{\text{sim}}}{\partial \eta_l}\right)^k \cdot \mathbf{r}(P^{\text{sim}}(\boldsymbol{\eta}^k), P^{\text{obs}})\right\}$; thus, the SVD-calculated multi-rank loading scores from the precipitation space-time matrix $\text{SVD}\left(P_{t_s,s}^{\text{obs}} \middle| \begin{matrix} t_s = 1 \sim T_s \\ s = 1 \sim S \end{matrix}\right)$ can not only characterize the rain-making causes and classify rain-generating mechanisms but also approximate a more accurate Hessian matrix while significantly reducing the number of simulations.

Before SVD, the average precipitation a_s and standard deviation ε_s of the sth observation station are used to normalize the precipitation space–time matrix $[P_{t,s}^{\text{obs}}]$. The analyzed matrix $\overline{\mathbf{X}}$ can be expressed in equation (26a):

$$\overline{\mathbf{X}} = \begin{bmatrix} \left(\mathbf{P}_{1,\bullet}^{\text{obs}} - \mathbf{a}\right)^{\text{T}} \\ \left(\mathbf{P}_{2,\bullet}^{\text{obs}} - \mathbf{a}\right)^{\text{T}} \\ \vdots \\ \left(\mathbf{P}_{T_s,\bullet}^{\text{obs}} - \mathbf{a}\right)^{\text{T}} \end{bmatrix} | \bullet \rightarrow s = 1 \sim S \cdot \begin{bmatrix} 1/\varepsilon_1 & 0 & \cdots & 0 \\ 0 & 1/\varepsilon_2 & 0 & \vdots \\ \vdots & 0 & \ddots & 0 \\ 0 & \cdots & 0 & 1/\varepsilon_S \end{bmatrix} \tag{26a}$$

where $\mathbf{a} = \boldsymbol{\mu}_1 \in \left\{a_s = \frac{1}{T_s} \sum_{t_s=1}^{T_s} P_{t_s,s}^{\text{obs}}\right\}$ is the average vector composed of s number of elements and

$(\boldsymbol{\mu}_2)^{\frac{1}{2}} \in \left\{ \varepsilon_s = \sqrt{\frac{1}{(T_s-1)}\sum_{t_s=1}^{T_s}\left(P_{t_s,s}^{\mathrm{obs}}-a_s\right)^2} \right\}$ is the standard deviation vector. This study decomposes the deviation of the observed precipitation space-time matrix $\mathbf{X} = [(\mathbf{P}_{t_s,\bullet}^{\mathrm{obs}} - \mathbf{a})^{\mathrm{T}}|_{t_s=1\sim T_s}]$ into a series of rain-generating components using SVD, as expressed in equation (26b):

$$\mathbf{X} = \mathbf{U}\boldsymbol{\Sigma}\mathbf{V}^{\mathrm{T}} \tag{26b}$$

where the row vector of $\mathbf{U}(= T_s \times S)$ is an orthonormal left singular vector $\{\mathbf{u}_{1,\bullet},...,\mathbf{u}_{T_s,\bullet}\}$, that is, eigenvector $\mathbf{U}^{\mathrm{T}}\mathbf{U} = \mathbf{I}$; $\boldsymbol{\Sigma} = \mathrm{diag}(\sigma_1,...,\sigma_S)$, $\sigma_1 \geq ... \geq \sigma_S \geq 0$ is the singular value, where σ_j can calculate the eigenvalue $\tau_j = \frac{1}{T_s-1}\sigma_j^2 = (\mathbf{F}_{j,\bullet}^{\mathrm{T}})\cdot(\mathbf{F}_{j,\bullet})$; and the row vector of $\mathbf{V}(= S \times S)$ is an orthonormal right singular vector $\{\mathbf{v}_{1,\bullet},...,\mathbf{v}_{S,\bullet}\}$, $\mathbf{V}\mathbf{V}^{\mathrm{T}} = \mathbf{V}^{\mathrm{T}}\mathbf{V} = \mathbf{I}$. Let $\varphi_{j,s}$ be the correlation coefficient between the observed precipitation at the sth station and jth principal component (PC) coefficient, called factor loading, and its set is the $S \times S$-order matrix $\mathbf{F} = [\varphi_{j,s}]$. Since $\overline{\mathbf{X}}$ contains standardized data, using the following substitutions $\overline{\mathbf{X}} = \mathbf{X}\mathbf{D}^{-1}$, $\boldsymbol{\Lambda}^{1/2} = \frac{1}{\sqrt{T_s-1}}\boldsymbol{\Sigma}$, $\mathbf{C} = \mathbf{X}\mathbf{V}\boldsymbol{\Lambda}^{-1/2}$, and $S = \frac{1}{T_s-1}\mathbf{X}^{\mathrm{T}}\mathbf{X} = \mathbf{V}\boldsymbol{\Lambda}\mathbf{V}^{\mathrm{T}}$, the below calculations in equation (27) can be derived:

$$\mathbf{F} = \frac{1}{T_s-1}\overline{\mathbf{X}}^{\mathrm{T}}\mathbf{C} = \frac{1}{T_s-1}\left(\mathbf{D}^{-1}\mathbf{X}^{\mathrm{T}}\right)\left(\mathbf{X}\mathbf{V}\boldsymbol{\Lambda}^{-1/2}\right) = \mathbf{D}^{-1}S\mathbf{V}\boldsymbol{\Lambda}^{-1/2} = \mathbf{D}^{-1}\left(\mathbf{V}\boldsymbol{\Lambda}\mathbf{V}^{\mathrm{T}}\right)\mathbf{V}\boldsymbol{\Lambda}^{-1/2}$$
$$= \mathbf{D}^{-1}\mathbf{V}\boldsymbol{\Lambda}\boldsymbol{\Lambda}^{-1/2} = \mathbf{D}^{-1}\mathbf{V}\boldsymbol{\Lambda}^{1/2} = \frac{1}{\sqrt{T_s-1}}\mathbf{D}^{-1}\mathbf{V}\boldsymbol{\Sigma} \tag{27}$$

Principal component analysis is applied to construct a rain-generating descriptive model for the observed spatiotemporal precipitation matrix associated with the atmospheric rain-making factors. The spatiotemporal deviation matrix $\mathbf{X}$ can be decomposed into multiple temporal feature components (factor score $\mathbf{C}$) and the spatial variable (loading $\mathbf{F}$), as derived in equation (28):

$$\mathbf{X} = \begin{bmatrix} P_{1,1}^{\mathrm{obs}}-a_1 & \cdots & P_{1,s}^{\mathrm{obs}}-a_s & \cdots & P_{1,S}^{\mathrm{obs}}-a_S \\ \vdots & \ddots & \vdots & \ddots & \vdots \\ P_{t_s,1}^{\mathrm{obs}}-a_1 & \cdots & P_{t_s,s}^{\mathrm{obs}}-a_s & \cdots & P_{t_s,S}^{\mathrm{obs}}-a_S \\ \vdots & \ddots & \vdots & \ddots & \vdots \\ P_{T_s,1}^{\mathrm{obs}}-a_1 & \cdots & P_{T_s,s}^{\mathrm{obs}}-a_s & \cdots & P_{T_s,S}^{\mathrm{obs}}-a_S \end{bmatrix} = \mathbf{U}\boldsymbol{\Sigma}\mathbf{V}^{\mathrm{T}} = \mathbf{U}\boldsymbol{\Sigma}\mathbf{V}^{\mathrm{T}}\mathbf{D}^{-1}\mathbf{D} = \sqrt{T_s-1}\,\mathbf{U}\left(\frac{1}{\sqrt{T_s-1}}\mathbf{D}^{-1}\mathbf{V}\boldsymbol{\Sigma}\right)^{\mathrm{T}}\mathbf{D} = \mathbf{C}\mathbf{F}^{\mathrm{T}}\mathbf{D}$$

$$= \begin{bmatrix} \vartheta_{1,1} & \cdots & \vartheta_{j,1} & \cdots & \vartheta_{\Gamma,1} \\ \vdots & \ddots & \vdots & \ddots & \vdots \\ \vartheta_{1,t_s} & \cdots & \vartheta_{j,t_s} & \cdots & \vartheta_{\Gamma,t_s} \\ \vdots & \ddots & \vdots & \ddots & \vdots \\ \vartheta_{1,T_s} & \cdots & \vartheta_{j,T_s} & \cdots & \vartheta_{\Gamma,T_s} \end{bmatrix} \begin{bmatrix} \phi_{1,1} & \cdots & \phi_{1,s} & \cdots & \phi_{1,S} \\ \vdots & \ddots & \vdots & \ddots & \vdots \\ \phi_{j,1} & \cdots & \phi_{j,s} & \cdots & \phi_{j,S} \\ \vdots & \ddots & \vdots & \ddots & \vdots \\ \phi_{\Gamma,1} & \cdots & \phi_{\Gamma,s} & \cdots & \phi_{\Gamma,S} \end{bmatrix} \begin{bmatrix} \varepsilon_1 & 0 & \cdots & 0 \\ 0 & \varepsilon_2 & 0 & \vdots \\ \vdots & 0 & \ddots & 0 \\ 0 & \cdots & 0 & \varepsilon_S \end{bmatrix} \tag{28}$$

$$= \left\{ \begin{bmatrix} \vartheta_{1,1}\phi_{1,1} & \cdots & \vartheta_{1,1}\phi_{1,s} & \vartheta_{1,1}\phi_{1,S} \\ \vdots & \ddots & \vdots & \vdots \\ \vartheta_{1,t_s}\phi_{1,1} & \cdots & \vartheta_{1,t_s}\phi_{1,s} & \vartheta_{1,t_s}\phi_{1,S} \\ \vdots & \ddots & \vdots & \vdots \\ \vartheta_{1,T_s}\phi_{1,1} & \cdots & \vartheta_{1,T_s}\phi_{1,s} & \vartheta_{1,T_s}\phi_{1,S} \end{bmatrix} + \cdots + \begin{bmatrix} \vartheta_{j,1}\phi_{j,1} & \cdots & \vartheta_{j,1}\phi_{j,s} & \vartheta_{j,1}\phi_{j,S} \\ \vdots & \ddots & \vdots & \vdots \\ \vartheta_{j,t_s}\phi_{j,1} & \cdots & \vartheta_{j,t_s}\phi_{j,s} & \vartheta_{j,t_s}\phi_{j,S} \\ \vdots & \ddots & \vdots & \vdots \\ \vartheta_{j,T_s}\phi_{j,1} & \cdots & \vartheta_{j,T_s}\phi_{j,s} & \vartheta_{j,T_s}\phi_{j,S} \end{bmatrix} + \cdots + \begin{bmatrix} \vartheta_{\Gamma,1}\phi_{\Gamma,1} & \cdots & \vartheta_{\Gamma,1}\phi_{\Gamma,s} & \vartheta_{\Gamma,1}\phi_{\Gamma,S} \\ \vdots & \ddots & \vdots & \vdots \\ \vartheta_{\Gamma,t_s}\phi_{\Gamma,1} & \cdots & \vartheta_{\Gamma,t_s}\phi_{\Gamma,s} & \vartheta_{\Gamma,t_s}\phi_{\Gamma,S} \\ \vdots & \ddots & \vdots & \vdots \\ \vartheta_{\Gamma,T_s}\phi_{\Gamma,1} & \cdots & \vartheta_{\Gamma,T_s}\phi_{\Gamma,s} & \vartheta_{\Gamma,T_s}\phi_{\Gamma,S} \end{bmatrix} \right\} \begin{bmatrix} \varepsilon_1 & 0 & \cdots & 0 \\ 0 & \varepsilon_2 & 0 & \vdots \\ \vdots & 0 & \ddots & 0 \\ 0 & \cdots & 0 & \varepsilon_S \end{bmatrix}$$

$$= \left\{ \left(\mathbf{C}_{1,\bullet}\right)\left(\mathbf{F}_{1,\bullet}^{\mathrm{T}}\right) + \cdots + \left(\mathbf{C}_{j,\bullet}\right)\left(\mathbf{F}_{j,\bullet}^{\mathrm{T}}\right) + \cdots + \left(\mathbf{C}_{\Gamma,\bullet}\right)\left(\mathbf{F}_{\Gamma,\bullet}^{\mathrm{T}}\right) \right\} \mathbf{D}_{\bullet}\Big|_{\bullet\to s=1\sim S}^{\to t_s=1\sim T_s} = \boldsymbol{\Psi}_{1,\bullet,\bullet}^{\mathrm{T}} + \cdots + \boldsymbol{\Psi}_{j,\bullet,\bullet}^{\mathrm{T}} + \cdots + \boldsymbol{\Psi}_{\Gamma,\bullet,\bullet}^{\mathrm{T}}$$

The element of $\boldsymbol{\Psi}_{j,\bullet,\bullet}^{\mathrm{T}}$ is calculated from the score $(\mathbf{C}_{*,\bullet})$ and loading $(\mathbf{F}_{*,\bullet}^{\mathrm{T}})$ decomposed by SVD $\left(P_{t,s}^{\mathrm{obs}}\Big|_{s=1\sim S}^{t=1\sim T_s}\right)$, as shown in equation (28), and $\mathbf{D}_{\bullet} = \mathrm{diag}(\varepsilon_1,...,\varepsilon_S)$ is the diagonal standard deviation matrix. In this study, model parameters $\boldsymbol{\mu}_1^{:s}$, $(\boldsymbol{\mu}_2^{:s})^{\frac{1}{2}}$, $\mathbf{w}_{:,*}^{\mathrm{T}}$, and $\mathbf{b}_*$ are used to project multiple rain-making factors into the dimension-reduced rainfall spatiotemporal feature unit $\boldsymbol{\Psi}_{j,\bullet,\bullet}^{\mathrm{T}}$ for establishing the composite swarm rain-generating simulation functions, and the analytically derived $\mathbf{H}(\boldsymbol{\eta}^k, \Delta\boldsymbol{\eta}^{k^-}) =$

$$\left\{ \begin{array}{l} \left[(\mathbf{B}-\mathbf{b})\cdot\left[\dfrac{\boldsymbol{\Gamma}^{-1}}{w}\right]^{\mathrm{T}}\circ(\boldsymbol{\mu}_2)^{\frac{1}{2}}+\boldsymbol{\mu}_1\right]_{\mathrm{Lx1}}^{\mathrm{T}}\cdot 2[\mathbf{r}^k+\boldsymbol{\kappa}^k]^{\mathrm{T}}\cdot N^{-1}\left(\mathbf{a}e_{\mathrm{Mx\Gamma}}^{\theta\gamma^k\Pi(\boldsymbol{\chi})}\cdot\left[\dfrac{\boldsymbol{\iota}}{\boldsymbol{\iota}+\boldsymbol{\alpha}e^{-\mathbf{B}\Pi(\boldsymbol{\chi})}}\right]^{\mathrm{T}}\cdot\left[\dfrac{\boldsymbol{\alpha}e^{-\mathbf{B}\Pi(\boldsymbol{\chi})}}{\boldsymbol{\iota}+\boldsymbol{\alpha}e^{-\mathbf{B}\Pi(\boldsymbol{\chi})}}\right]\cdot\left[(\boldsymbol{\mu}_2)^{\frac{-1}{2}}\cdot\mathbf{w}\right]_{\Gamma x1}^{\mathrm{T}}\right)\cdot\left[\dfrac{L^{-1}}{\Delta\boldsymbol{\eta}^{k^-}}\right]_{\mathrm{1xL}}^{\mathrm{T}}\cup \\[4ex] \left[(\mathbf{B}-\mathbf{b})\left[\dfrac{\boldsymbol{\Gamma}^{-1}}{w}\right]^{\mathrm{T}}\circ(\boldsymbol{\mu}_2)^{\frac{1}{2}}+\boldsymbol{\mu}_1\right]_{\mathrm{Lx1}}^{\mathrm{T}}\cdot 2[\mathbf{r}^k+\boldsymbol{\kappa}^k]^{\mathrm{T}}\cdot N^{-1}\left(\mathbf{a}e_{\mathrm{Mx\Gamma}}^{\theta\gamma^k\Pi(\boldsymbol{\chi})}\cdot\left(\boldsymbol{\iota}-\left[\dfrac{e^{\mathbf{B}\Pi(\boldsymbol{\chi})}-e^{-\mathbf{B}\Pi(\boldsymbol{\chi})}}{e^{\mathbf{B}\Pi(\boldsymbol{\chi})}+e^{-\mathbf{B}\Pi(\boldsymbol{\chi})}}\right]^{\mathrm{T}}\left[\dfrac{e^{\mathbf{B}\Pi(\boldsymbol{\chi})}-e^{-\mathbf{B}\Pi(\boldsymbol{\chi})}}{e^{\mathbf{B}\Pi(\boldsymbol{\chi})}+e^{-\mathbf{B}\Pi(\boldsymbol{\chi})}}\right]\right)\cdot\left[(\boldsymbol{\mu}_2)^{\frac{-1}{2}}\cdot\mathbf{w}\right]_{\Gamma x1}^{\mathrm{T}}\right)\cdot \\[4ex] \left[\dfrac{L^{-1}}{\Delta\boldsymbol{\eta}^{k^-}}\right]_{\mathrm{1xL}}^{\mathrm{T}} \end{array} \right\}$$

is used to calculate the approximated Hessian matrix and explore multiple local minima locations.

2.8. Application

Spanning a total area of 36,188 km^2, Taiwan is located at the junction of Northeast and Southeast Asia, bordered by the Pacific Ocean to the east, the Taiwan Strait to the west, the Bashi Strait to the south, and Okinawa to the northeast. The terrain comprises mountains, plains, and hills/basins/tablelands, accounting for 31.5 %, 31.3 %, and 37.2 % of the total area. From east to west, the
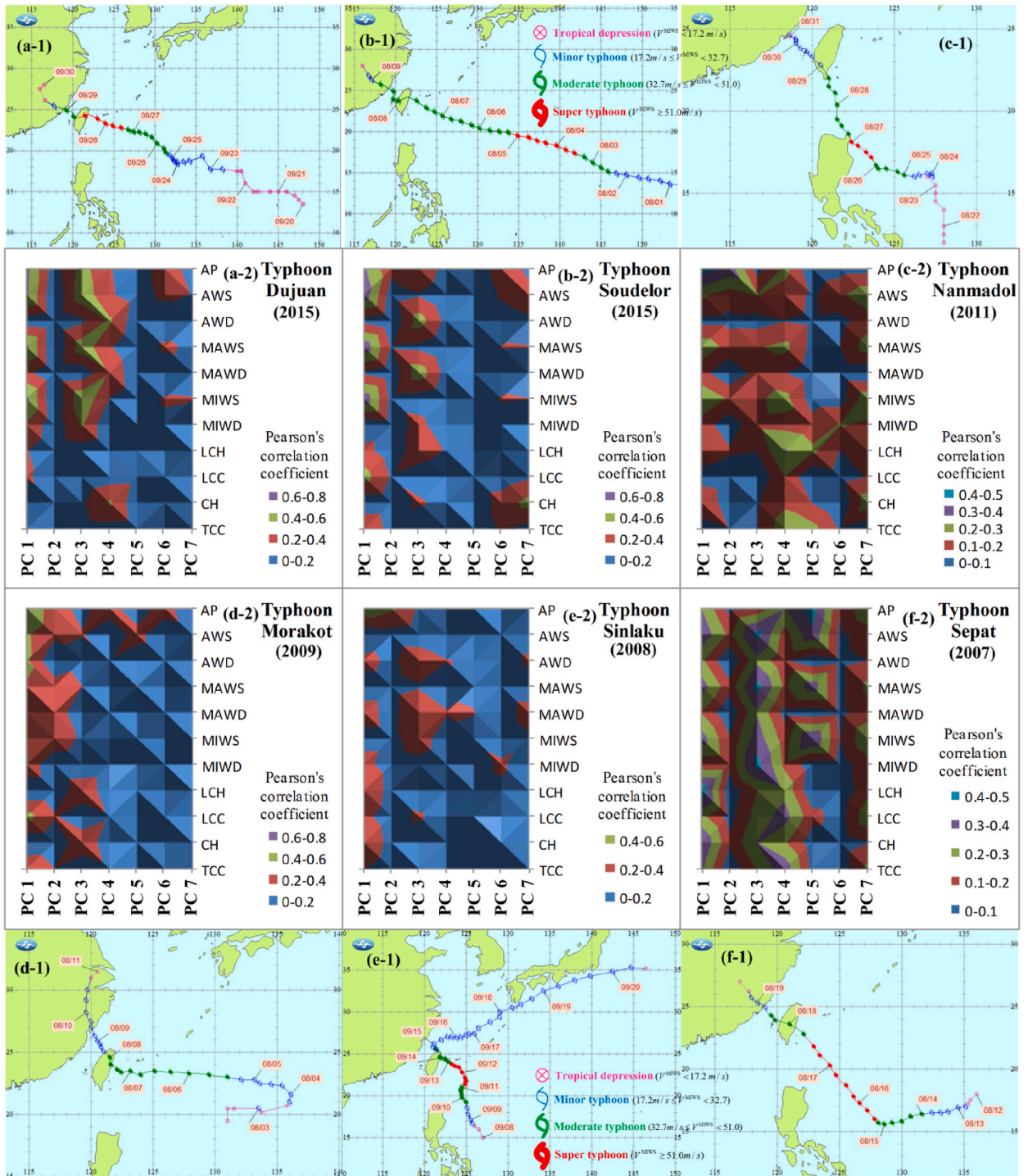

Fig. 3. Rain-making DNAs of category 1 typhoons in Taipei: PC rank versus cause (−2) related to the moving path (−1) of typhoons (a) Dujuan, (b) Soudelor, (c) Nanmadol, (d) Morakot, (e) Sinlaku, and (f) Sepat.

mountains can be divided into Coast, Central, Snow, Yushan, and Alishan mountain ranges, as shown in Fig. 2. The Tropic of Cancer (23.5°N) passes through middle-southern Taiwan. According to the Köppen classification, the Taiwanese climate is divided into four types: southern tropical monsoon, northern humid and warm, western humid and hot summer, and mountainous humid and cool summer climates. Meteorological development in Taiwan originated from the Japanese ruling the country in 1896, who first built seven official observatories for weather forecasts and storm warnings. The northeast monsoon prevailing between October and April is strong due to the enormous pressure gradient. The southwest monsoon prevails between May and September, with relatively low wind spend. June to October marks the typhoon season, often triggering rainstorms, floods, and landslides. The annual average rainfall is approximately 2467 mm, unevenly distributed in time and space, with nearly 78 % concentrated from May to October. Considering the completeness of atmospheric rain-generating factorial observations during typhoons, this study selected seven representative meteorological observatories to identify rain-making causes and quantity. Among these, Taipei and Taichung belong to the basin topography, Hualien and Taitung to coastal hills/tablelands, Chuzihu to mountains, and Yilan and Kaohsiung to plains.
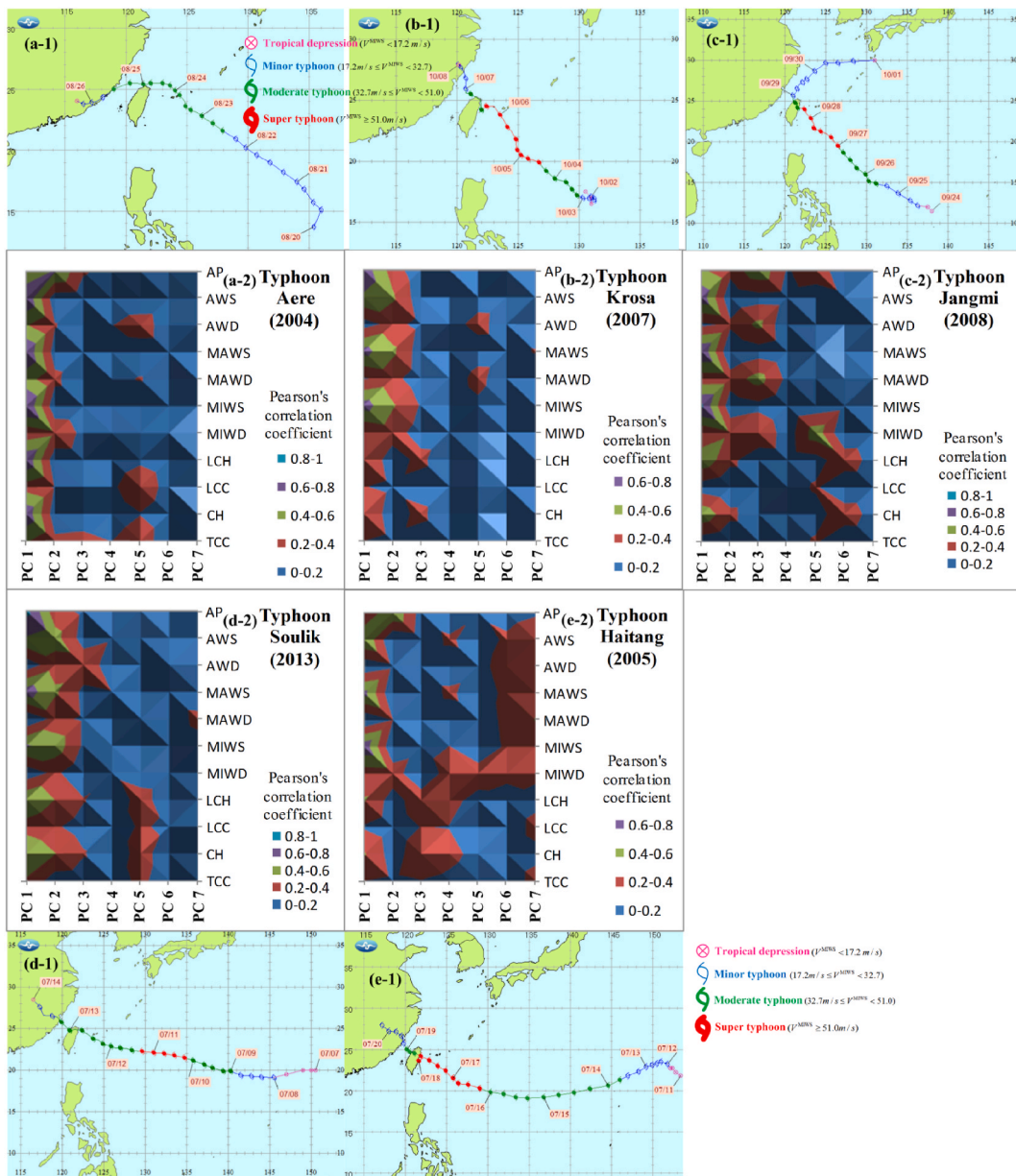
Fig. 4. Rain-making DNAs of category 2 typhoons in Taipei: PC rank *versus* cause (−2) related to the moving path (−1) of typhoons (a) Aere, (b) Krosa, (c) Jangmi, (d) Soulik, and (e) Haitang.

3. Results and discussion

3.1. Adopted typhoon events for analysis

Considering the observed spatiotemporal integrity of the typhoon atmospheric and weather observatories, 11 super typhoons that hit Taiwan and caused heavy rains were selected for rain-generating simulation and rain-making factorial identification-optimization. The event information is provided in Table S1; the typhoon duration ranged between 53 and 96 h.

3.2. Classified typhoon categories using fuzzy c-means clustering

The present study uses fuzzy c-means clustering [48] to analyze the associated characteristics of moving paths, atmospheric structures, and rainfall patterns of historical typhoons. The classified factors included the observed time series of the typhoon's central location, 11 atmospheric rain-making factors, and rainfall hydrographs in Taipei and Kaohsiung. Figs. S1(a–c) shows the spatio-temporal distribution of the moving trajectories and average near-center maximum wind speed (MAWS) for each category. Based on this, the rain-making factor-induced rainfall patterns can be divided into two categories, and typhoon wind/rain prediction may improve accuracy derived from the azimuth-wind field-rainfall analyzed results. While hitting Taiwan, the moving direction of typhoons in category 1 did not change much (between 272° and 339°), and after passing through Taiwan, the moving path turned to head between 318° and 32°. Before hitting Taiwan, typhoons in category 2 were generally heading northwest (between 296° and 323°) and turned to head west at landfall. After passing through the Central and Snow mountain ranges, 63 % turned to head between 285° and 6°. Crossing the five major mountain ranges seriously damaged the typhoon's structure and intensity. Since the average moving speed of the typhoons in category 1 (17.3 km h^{-1}) was significantly faster than that of typhoons in category 2 (11.7 km h^{-1}), the weakening damage of the structural wind speed for category 1 was relatively slight. After crossing the mountains, the MAWS (39 m s^{-1}) of typhoons in category 1 was moderately stronger than those in category 2 (32 m s^{-1}).

3.3. Identified rain-making DNAs of typhoons in the characteristic categories

We performed SVD on the spatiotemporal rainfall patterns of typhoons characteristically classified in section 3.2. Then we calculated Pearson's correlation coefficients between each component and rain-making variable to determine the causative rain-making DNAs (−2), which are associated with paths of typhoons (−1) in categories 1 and 2 in Taipei are shown in Fig. 3(a–f) and Fig. 4(a–e), respectively and those in Kaohsiung are shown in Fig. S2(a–f) and S3 (a–e), respectively. Analytical results show that the different typhoons were unique in their observatory's rain-making DNA, and the identified multi-rank rain-generating components from each specific wind/cloud factor can improve prediction accuracy in rainfall patterns and causal parameters. Specifically, DNAs for category 1 typhoons in Taipei were mainly concentrated in PCs 1, 3, 4, and 7, which DNAs of typhoons Dujuan and Soudelor, Nanmadol and Sepat as well as of Morakot and Sinlaku were very similar. Comparison of paths reveals that the more similar the rain-making DNA, the more similar the moving direction and trajectory. The rainfall features of category 2 typhoons in Taipei were concentrated on PCs 1, 2, and 5; specifically, the DNAs of typhoons Aere, Soulik, and Haitang were approximately similar, and those of Krosa and Jangmi were partially similar; for these typhoons, causal components on PC1 were related to wind speed and cloud distribution (LCH and CH); those on PC2 were related to specific wind factors; and those on PC5 were mostly generated by cloud cover distribution (LCH, LCC, CH, and TCC).

For category 1 typhoons in Kaohsiung, the rain-making DNAs in multi-rank components were more diverse than those in Taipei. Specifically, the DNAs of typhoons Dujuan and Soudelor were very similar; moreover, their moving path and direction were very similar, with rainfall features mainly concentrated on PC1 and PC3, closely related to wind factors. Further, the DNAs of typhoons Nanmadol and Morakot were similar, with rain-making factors concentrated on PCs 1, 2, and 4, which were closely related to wind force/direction. The two typhoons moved in a similar direction during their landing in Taiwan. However, Nanmadol, which invaded southern Taiwan, lacked the rain-making source on PC6, compared to Morakot, which invaded the north. Additionally, the DNAs of Sinlaku, which crossed northern Taiwan, were more abundant than those of Sepat, which crossed the south, indicating rather diverse rain-making sources. In Kaohsiung, the DNA features and moving directions of category 2 typhoons Aere, Jangmi, and Krosa were similar before invading Taiwan. Their rain-making factors for wind force/direction and cloud cover were distributed on PC1. In particular, high-rank components for Aere, which traveled westward after invading Taiwan, were mainly concentrated on PCs 2 and 5; those for Jangmi, which traveled northwest, were concentrated on PCs 2 and 6; and those for Krosa, which traveled east, were concentrated on PCs 2, 3, and 5. The moving directions and DNAs of Soulik and Haitang were very similar, with primary factors concentrated on PCs 1 and 2 and secondary on PC4 and PC5. Overall, for category 2 typhoons in Kaohsiung, wind force and direction triggered more rainfall than cloud cover distribution.

3.4. Rain-generating modeling results and discussion

Given that the number of simulation model parameters in this study is not more than the number of observations with no risk of occurring ill-posed problem, BFGS quasi-Newton and CG algorithms [37] were used with cross-validation to identify rain-generating model parameters for typhoons with similar rain-making DNAs in section 3.3. Comparison of simulated and observed rainfall hydrographs after model calibration for the Taipei and Kaohsiung observatories are presented in Figs. S4 and S5, respectively, in which the shown typhoon events occurred during heavy rains at the corresponding observatories. For rainfall during typhoons Soudelor and
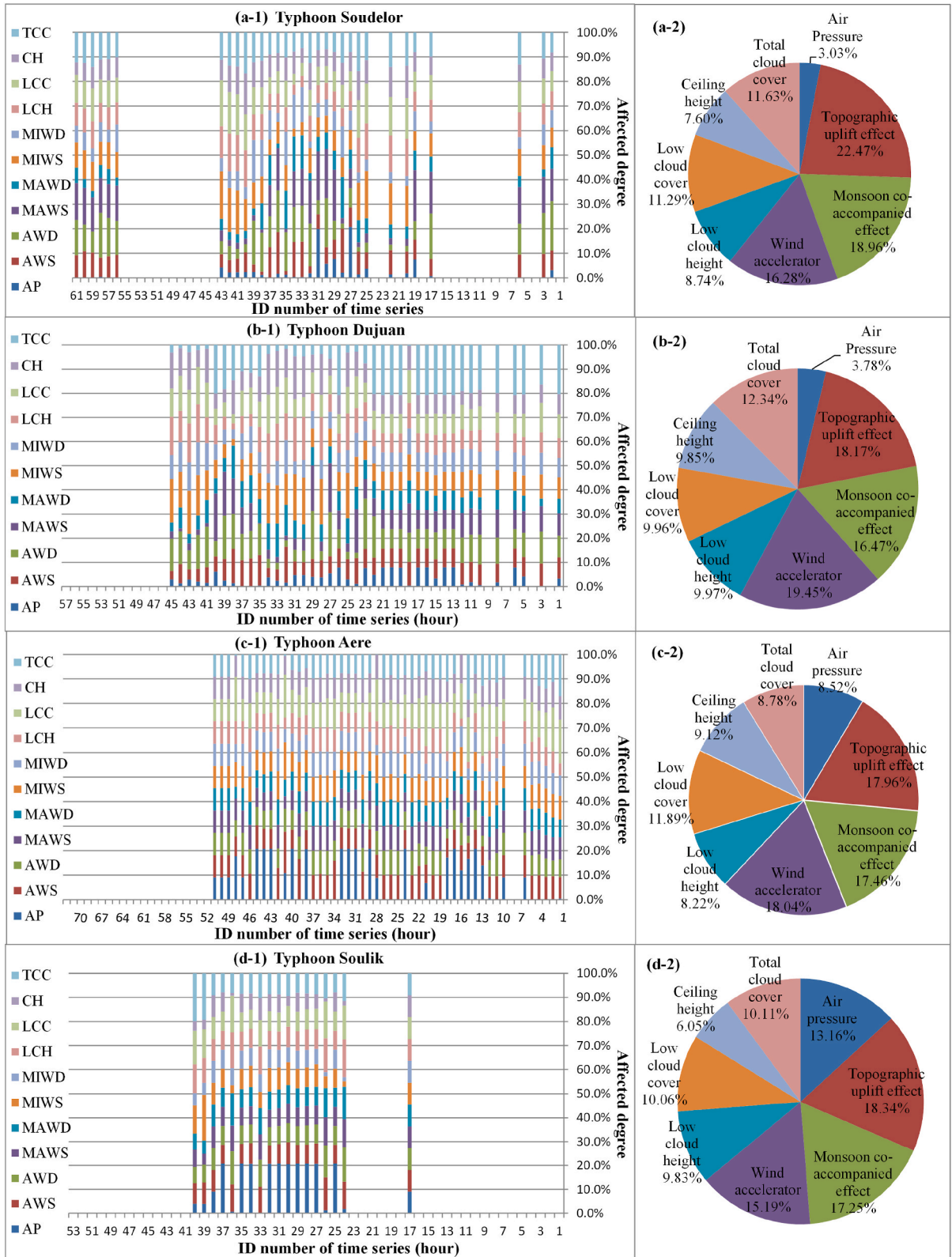
Fig. 5. Identified temporal patterns (−1) and overall averaged charts (−2) of causal rainfall-making degree composition for typhoons (a) Soudelor, (b) Dujuan, (c) Aere, and (d) Soulik in Taipei.

Dujuan in Taipei, simulated MAE values are 2.132 and 3.066 mm h^{-1}, and CC values are respectively 0.936 and 0.696. For Aere and Soulik, simulated MAEs are respectively 1.802 and 1.273 mm h^{-1}, and CCs are respectively 0.905 and 0.734. The changing trends of simulated and observed rainfall hydrographs are similar, indicating that the selected rain-making factors could realistically simulate the generated rainfall. For rainfall during typhoons Soudelor, Dujuan, Morakot, Sepat, Haitang, and Jangmi in Kaohsiung, simulated MAEs are respectively 1.549, 0.239, 3.098, 0.489, 1.261, and 1.028 mm h^{-1} and CCs are respectively 0.915, 0.876, 0.922, 0.925, 0.950, and 0.933. Overall, the established rain-generating model with the designed swarm response functions could effectively simulate fluctuating trajectories and yield accurate rainfall hydrographs under various rain-making factorial interactions with different invasive paths, structures, intensity, and cloud cover distribution.

3.5. Identified multi-causal rain-making thresholds during typhoons

By identifying the distribution of various causal rain-making thresholds while invading Taipei and Kaohsiung using the designed key–lock quasi-Newton optimization, as shown in Fig. S6(1–10) and S7 (1–10), the rain-generating mechanisms and characteristics of various typhoon's atmospheric conditions are illustrated. The induced rainfall with occurrence timing may predict more accurately according to these identified threshold parameters and observed/simulated atmospheric variables. While invading Taipei, the results for typhoons Aere and Soulik were as follows. (1) The rain-making thresholds for MAWS, MIWS, CH, and TCC presented a steady state, and the ranges of MAWS were respectively 10.20–10.53 and 7.83–8.11 m s^{-1} (2) Thresholds for the angle between AWD and geomorphic notch axis, angle between MAWD and monsoon, LCH, and LCC presented an approximate steady-state; ranges of the converging accompanied maximum angle of monsoon were respectively 51.16°–53.20° and 49.62–51.42°, and the thresholds for LCC were respectively 9.07–9.26 and 7.70–7.88. (3) Thresholds for AP and AWS presented a similar steady-state; AP threshold ranges were 996.99–999.44 and 993.47–998.39 hPa, respectively. These characteristics can be attributed to small changes in the moving direction of Aere and Soulik while invading Taiwan, paths not passing through the mountain ranges, and small damage to the wind/cloud structure. In contrast, when hitting Taipei, only the TCC of Soudelor and Dujuan presented a similar steady-state, whereas the remaining variables were unsteady, even with a gradual transition. For these typhoons, ranges of rain-making thresholds for MAWS were respectively 11.23–15.35 (average = 12.73) m·s^{-1} and 8.38–11.92 m s^{-1}; those of monsoon's co-accompanying maximum angle were respectively 54.59°–66.88° (average = 58.19°) and 48.89°–61.09°; those of LCC were 7.27–8.64 and 8.54–9.80; and those of AP were 994.36–999.38 and 1000.92–1004.26 hPa. These changes in rain-making thresholds when invading Taiwan can be attributed to significant changes in moving direction and paths crossing towering mountains, resulting in severe damage to the atmospheric structure. Overall, the fluctuating and multi-peak rain types of Soudelor and Dujuan were more obvious than those of Aere and Soulik.

As opposed to the trends in Taipei, when hitting Kaohsiung, the rain-making thresholds for AWS, the angle between AWD and mountainous vertical axis, MAWS, the angle between MAWD and monsoon, MIWS, LCH, LCC, CH, and TCC of typhoons Dujuan, Haitang, Jangmi, and Sepat were steady (Fig. S7(1–10)). For these typhoons, the rain-making thresholds for monsoon's co-accompanying maximum angles were respectively 46.51°, 50.87°, 79.36°, and 44.14°; those for MAWS were respectively 8.53, 8.57, 4.76, and 5.87 m s^{-1}; and those for LCC were respectively 9.26, 8.23, 7.71, and 6.91. The thresholds for Jangmi were overall lower than those for the other three typhoons because it carried a large cloud cover and high wind speed while traveling between northwest and north-northwest, introducing strong monsoon airstreams. The rain-making thresholds for AP were as follows. (1) For Morakot and Haitang, AP presented an unsteady gradual transition, with thresholds of respectively 985.43–1006.34 and 990.06–1001.79 hPa, because of severe topographical damage to the wind/cloud structure and large atmospheric environmental changes during typhoons. (2) For Dujuan, Jangmi, and Sepat, AP presented a steady-state, with thresholds of 1001.60, 1002.12, and 996.34 hPa. Except for LCH, the other 10 rain-making factors for Soudelor showed a similar steady-state, and the thresholds for monsoon's co-accompanying maximum angle, MAWS, LCC, and AP were respectively 58.06°, 6.70 m s^{-1}, 5.07, and 991.21–995.24 hPa, because of the strong and rarely damaged wind/cloud structure and linear moving path at the time of invading Taiwan. Morakot differed from the other typhoons in that all rain-making factorial distributions of this typhoon showed large gradient transitions and were unsteady; specifically, thresholds for monsoon's co-accompanying maximum angle, MAWS, and LCC were respectively 38.72°–59.22°, 7.90–11.04 m s^{-1}, and 6.48–8.74. When crossing from the north of Kaohsiung at a slow speed and traveling between northwest and north-northwest, southwest monsoon airflow was introduced, and the multi-layer cloud cover was very abundant and thick, which triggered the largest typhoon rainfall event in history [31].

3.6. Spatiotemporal rain-making causal composition

The identified time distributed composition (−1) of causal rain-making degree and event-based space–time–integrated affected percentages (−2) for four typhoons that caused heavy rainfalls in Taipei, namely Soudelor, Dujuan, Aere, and Soulik, are presented in Fig. 5(a–d). These meticulously analyzed results can enhance the causal understanding of rain-generating processes and rain-making hot zones with detailed magnitude by each factor. The range of monsoon co-accompanying rain-making percentage was 16.47%–18.96 %, with a relatively unsteady distribution and intermittent producing characteristics because the rain-making amount is related to wind direction and the angle between typhoon and monsoon. The terrain uplift rain-making degree was between 17.96 % and 22.47 %, and rain-making was related to the angle between the wind field and the mountain axis. Since the mountainous ridgeline is fixed, but the monsoon's direction/intensity is time-varying, the rain-making distribution of terrain uplift was relatively stable and uniform. The affected degree of LCC and wind accelerator (MIWS + MIWD) was related to the observatory on the windward or leeward side. Overall, after crossing mountains, rainfall within the storm radius produced by LCC and wind accelerator was slightly higher than that at peripheral circulation before invading Taiwan. Figs. S8(a–g) shows the identified causal rain-making degree of the remaining
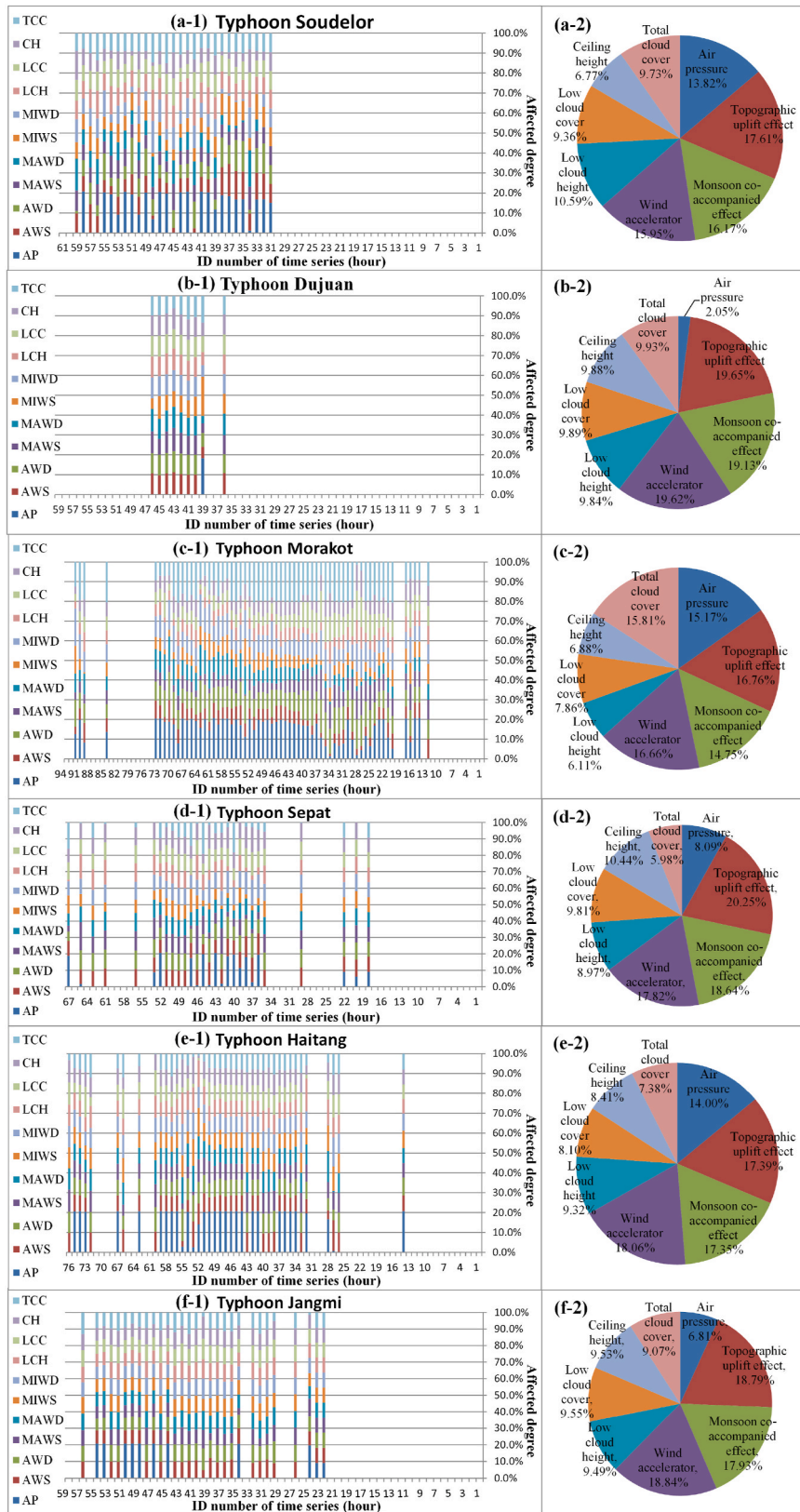
(caption on next page)

Fig. 6. Identified temporal patterns (−1) and overall averaged charts (−2) of causal rain-making degree composition for typhoons (a) Soudelor, (b) Dujuan, (c) Morakot, (d) Sepat, (e) Haitang, and (f) Jangmi in Kaohsiung.

typhoons (Nanmadol, Sepat, Morakot, Sinlaku, Haitang, Jangmi, and Krosa) that caused low rainfall in Taipei, illustrating the rain-making percentage of the monsoon's co-accompanying effect, terrain uplift effect, LCC, and wind accelerator (12.81%–18.96 %, 13.30%–22.47 %, 7.23%–11.29 %, and 14.05%–20.72 %, respectively).

Fig. 6(a–f) shows the identified causal rain-making composition and event-based average affected degree for typhoons Soudelor, Dujuan, Morakot, Sepat, Haitang, and Jangmi that caused heavy rains in Kaohsiung, illustrating the rain-making percentages of monsoon's co-accompanying and terrain uplift effects (14.75%–19.13 % and 16.76%–20.25 %, respectively); among these, distribution during Dujuan, Sepat, Haitang, Jangmi tended to be uniform. When crossing between the west-northwest and north-northeast of Kaohsiung, rainfall produced by the monsoon's convergent effect tended to increase because the above typhoons stably traveled between west-northwest and north-northwest at the time of invading Taiwan without major structural damage after crossing the mountains. During Soudelor and Morakot, large atmospheric changes led to the sharp turning of the moving path; thus, the rain-making hydrograph showed a non-uniform distribution. For the above six typhoons, the rain-making degree of LCC and wind accelerator ranged from 7.86 % to 9.89 % and from 15.95 % to 19.62 %, respectively; as such, the rain-making distribution between LCC and TCC and that between LCH and CH showed a mutual exchange, indicating strong horizontal convection and vertical exchange of cloud cover. In addition, when Sepat, Morakot, and Soudelor crossed the mountains, the atmospheric structure near the storm radius was disturbed, damaged, and pulled by the terrain. The rain-making supply of the wind accelerator was temporarily weakened but resumed after crossing the mountains and reorganization. Figs. S9(a–e) shows the event-averaged causative rain-making percentages of monsoon's co-accompanied effect, terrain uplift effect, LCC, and wind accelerator for the remaining typhoons (Nanmadol, Sinlaku, Krosa, Soulik, and Aere) that caused light rains in Kaohsiung were 14.96%–20.80 %, 15.77%–20.83 %, 9.16%–13.21 %, and 15.39%–20.20 %, respectively.

Furthermore, to explore in detail the causal relationships of the various rain-generating evolutional characteristic distributions with atmospheric, geomorphic, and oceanic environmental distributions, this study elaborately analyzed the spatiotemporal rain-making degree patterns of the terrain uplift effect, monsoon's co-accompanied effect, wind accelerator, and LCC during category 1 and 2 typhoons in Taipei and displayed rain-making hot zones with mechanisms, as shown in Figs. S10, S11, S12, and 7. As shown in Fig. S10(1-a – 1-f) and S10 (2-a – 2-e), when traveling between the northeast and south-southeast of Taipei, the multi-layer rainy cloud cover entrained by the wind field was transmitted along the Tamsui River Valley to the windward-sided Taipei Basin of the Snow Mountains, subsequently condensing moisture and producing rainfall, as observed in the case of typhoons Soudelor, Dujuan, Sepat, Sinlaku, Haitang, Krosa, and Aere. Additionally, when these typhoons were located in the hot zone between the west-southwest and north-northwest of Taipei, the rainy cloud airflow carried by the counterclockwise cyclone was transmitted along the Dahan Valley to the windward side of the Yangming Mountain, thereby producing heavy rainfall. Moreover, from event-based spatiotemporal rain-making distributions of MAWD shown in Fig. S11(1-a – 1-f) and S11 (2-a – 2-e), when the typhoons were located between the east-northeast and southwest of Taipei, their wind fields converged with gradient and geostrophic winds to transport airflow clouds and produce significant rainfall. Moreover, when Morakot, Haitang, and Aere were located between the west-southwest and north-north-west of Taipei, their wind fields converged with the southwest monsoon to introduce cloudy airflow and produce heavy rains. Furthermore, when located between the east-southeast and south-southeast of Taipei, the autumn typhoons Krosa, Jangmi, and Dujuan were in the northeast monsoon's co-accompanied rain-making hot zones. Furthermore, as shown in Fig. S12(1-a – 1-f) and S12 (2-a – 2-e), before the landfall of the center in Taiwan, the rain-making degree of MIWS was the largest, with a stable supply. While crossing mountains, the wind structure and cloud distribution are damaged; thus, the rainfall produced by MIWS after the typhoon leaves Taiwan is significantly lower than that at the time of landfall (e.g., for Soudelor, Dujuan, Soulic, Krosa, and Aere). Alternatively, Morakot, Sepat, Haitang, and Jangmi assume an unstably broken reforming state (e.g., Morakot, Sepat, Haitang, and Jangmi). Similarly, as shown in Fig. 7(1-a – 1-f) and 7 (2-a – 2-e), the rain-making degree of LCC before the landfall of the storm radius and at the time of invading Taiwan was significantly greater after crossing the mountains and heading toward the Taiwan Strait. All events indicated that cloudy rainbands were blocked by mountains when landing in and crossing Taiwan, and produced rain. The damaged wind field and cloud structure after crossing Taiwan were reorganized, which greatly reduced rain-making by LCC.

Contrary to the trends observed in Taipei, when traveling between the northwest and northeast of Kaohsiung, multi-layer clouds with rainbands carried by the typhoons' wind fields were transmitted along the Kaoping River Estuary to the windward Kaohsiung of Yushan Mountains, carrying condensed water vapor to produce rainfall, as observed in the case of Soudelor, Dujuan, Morakot, Sepat, Sinlaku, Jangmi, and Krosa (Fig. S13). In addition, when located between the west-southwest and northeast of Kaohsiung, the wind fields of typhoons converged with the southwest monsoon to introduce airflow with rainbands, causing its hot zone to have a particularly high monsoon's co-accompanied rain-making degree, as observed in the case of Soudelor, Morakot, Sepat, Haitang, and Aere (Fig. S14). When crossing between east-southeast and southwest of Kaohsiung, the wind fields of typhoons converged with gradient and geostrophic winds or the northeast airflow and carried cloudy rainbands to the catchment to produce heavy rains, as observed in the case of Nanmadol and Sepat. Furthermore, three trigger scenarios with hot zones can be illustrated from the Kaohsiung rain-making spatiotemporal distribution of MIWS in Fig. S15(1-a – 1-f) and S15 (2-a – 2-e). (1) After crossing the mountains, the cloud structure and rain-making intensity weakened, and after traveling toward the Taiwan Strait and reorganizing, the rain-making intensity of MIWS increased again, as in the case of Nanmadol, Sepat, Morakot, and Aere. (2) The intensity did not weaken significantly after crossing Taiwan and continued to supply rain-making amounts until the storm radius left Kaohsiung, as in the case of Soudelor, Haitang, and Jangmi. (3) Rain-making supply was available only during landfall in Taiwan and ceased after leaving the country, as in
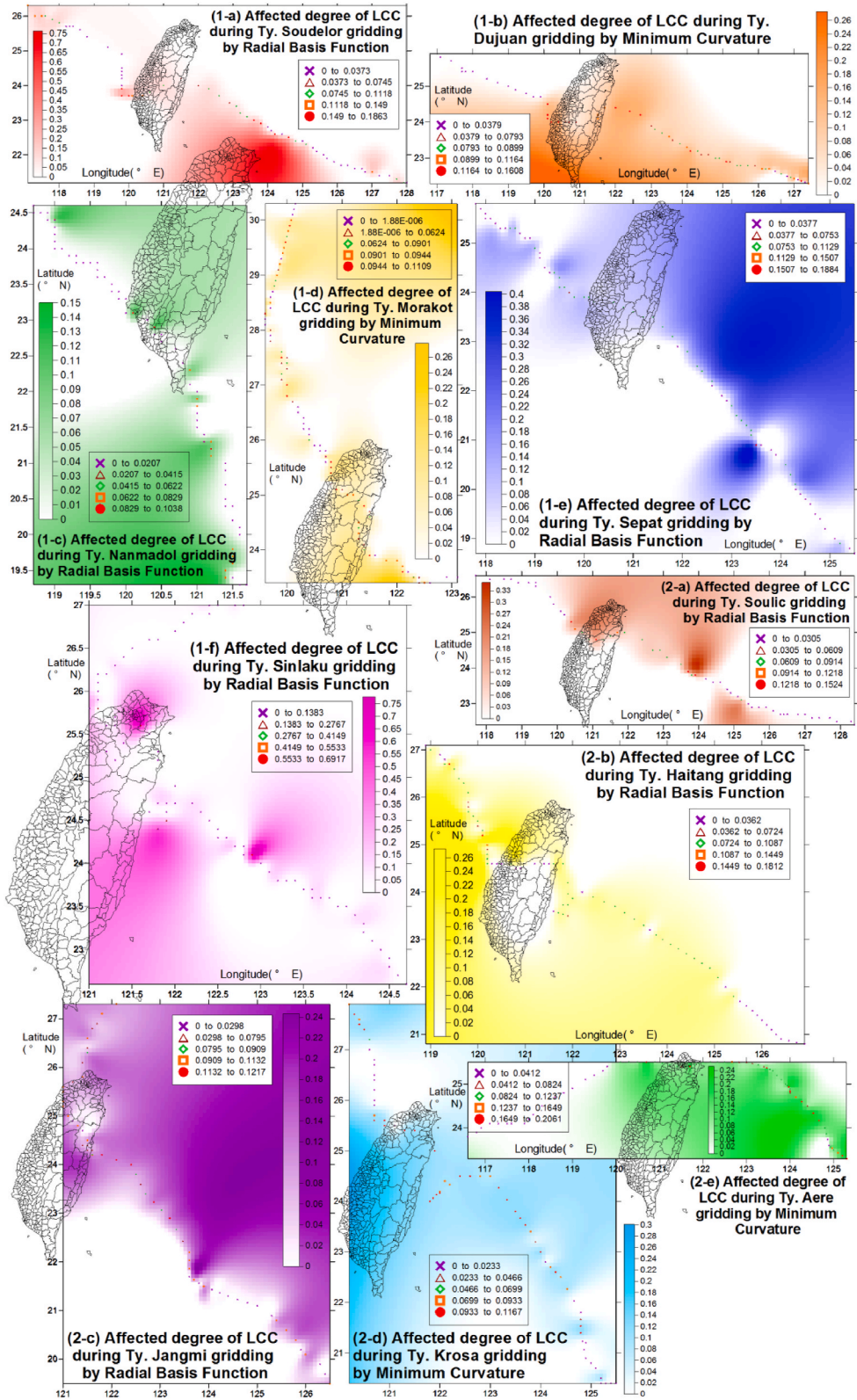
Fig. 7. Identified rain-making degree spatiotemporal patterns of LCC for category (1-) typhoons Soudelor (-a), Dujuan (-b), Nanmadol (-c), Morakot (-d), Sepat (-e), Sinlaku (-f) and category (2-) typhoons Soulic (-a), Haitang (-b), Jangmi (-c), Krosa (-d), Aere (-e) in Taipei.
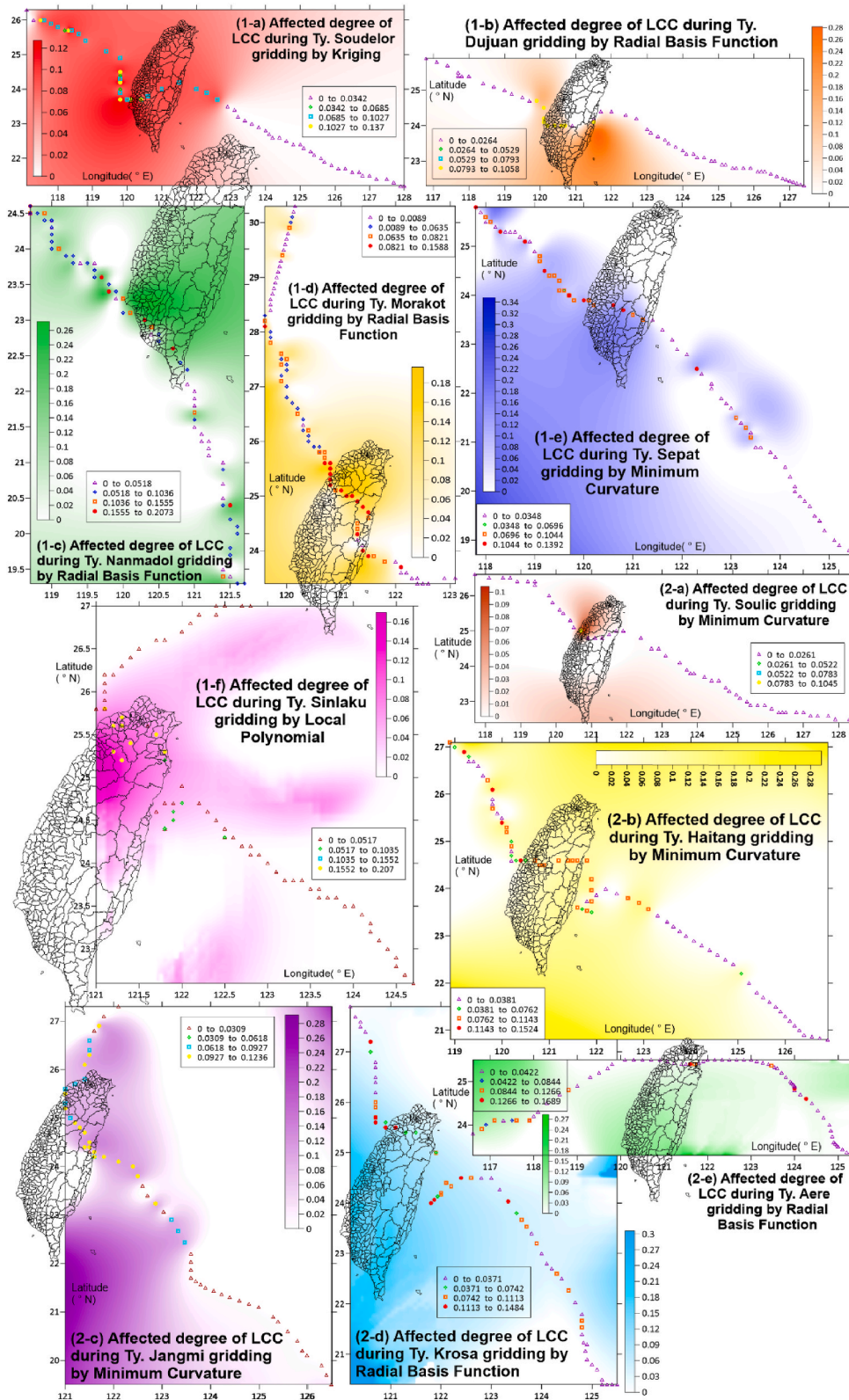
Fig. 8. Identified rain-making spatiotemporal patterns of LCC for category (1-) typhoons Soudelor (-a), Dujuan (-b), Nanmadol (-c), Morakot (-d), Sepat (-e), Sinlaku (-f) and category (2-) typhoons Soulic (-a), Haitang (-b), Jangmi (-c), Krosa (-d), Aere (-e) in Kaohsiung.

the case of Dujuan, Sinlaku, Soulic, and Krosa. Similarly, from the rain-making spatiotemporal distribution of LCC in Kaohsiung shown in Fig. 8(1-a – 1-f) and 8 (2-a – 2-e), three stochastic hot types can be illustrated. (1) The cloud structure was not damaged by the terrain when crossing the mountains, and after crossing, LCC continued to supply stable rainfall until the storm radius left, as in the case of Soudelor, Sepat, and Jangmi. (2) When landing in Taiwan, the rain-making degree of LCC increased and subsequently peaked. The cloud structure was moderately damaged when crossing the mountains, greatly weakening rain-making after moving toward the Taiwan Strait and showing intermittent supply and unstable reorganization, as in the case of Nanmadol, Morakot, Haitang, Krosa, and Aere. (3) LCC only caused rain during landfall in Taiwan. When crossing the mountains, the cloud structure was severely damaged and intercepted, and after moving toward the ocean, LCC could not produce rainfall in Kaohsiung, as in the case of Dujuan, Sinlaku, and Soulic.

4. Conclusions

Accurate spatiotemporal identification of typhoons' co-evolving rain-making causes and parameters with diverse dynamics is difficult. To precisely approximate the Hessian matrix, solve the nonlinear ill-posed problem, and reduce the simulated computational cost, this study uses composite logical tangent hyperbolic functions as systematic nonlinear advanced algebraic equations to construct the rain-generating simulation model, combined with a designed key–lock quasi-Newton optimizing derivation based on mathematical analysis to derive the Hessian matrix of high-dimensional multi-order derivatives of the objective function for rainfall cause decomposition into advanced functionalized algebraic analytical solution (lock) and constrained equations that satisfy Newton's condition. Specifically, the rank-two approximate structure of the LM and BFGS quasi-Newton algorithms are modified as that a symmetric rank-four structure, which could efficiently calculate an accurate, positive definite, and numerically stable Hessian, solve the constrained nonlinear optimization problem of rain-making threshold parameters, and quantify the rain-generating amount of every cause. The functional module specifically projects the observed variables of various atmospheric rain-making factors (e.g., multi-layer cloud height/cover, monsoon co-accompanied effect, terrain uplift effect, and ceiling height, among others) into multi-rank rain-loading scores calculated through SVD to classify rain-generating causes/mechanisms and characterize feature components under dimension reduction. To accelerate directional convergence, detect and escape the local minimum, approach the global optimum, and modify the search direction, this study devises vectorized limited switchable step size combined with a derived multi-order analytical solution to solve the rain-making cause threshold, reduce the difference of heterogeneous parameters, and eliminate the Hessian element value overestimated by the conventional quasi-Newtons. The candidate parameter correction vector (key) and the reference step-size distributed bounds solved by the analytically derived Newton's conditional constraints combined with an advanced functional precise double-bracketing approach could rapidly optimize the vectorized step size configured with various rain-making factors. Inputting the candidate solution into the Hessian analytical solution allow for calculating a Hessian that precisely satisfies Newton's conditions and determining the referenced parameter correction direction, including Taylor expansion error, derivative approximate error, and parameter uncertainty. Particularly, DNAs of various typhoons are identified to characterize the associated structure of moving tracks and rain-making causal degrees using fuzzy c-means clustering.

This study selects Taipei, Kaohsiung, and five other stations for typhoons' rain-making causal identification. Fuzzy c-means clustering revealed that the triggered rainfall could be characterized by two categories. The invasive angle of category 1 typhoons ranged from $272°$ to $339°$, and their paths turned between the north-northwest and north-northeast after crossing Taiwan. For category 2 typhoons, this angle was between $296°$ and $323°$ before invading Taiwan, and their path turned 63 % toward the north-northwest after crossing mountains. The identified rain-making DNAs revealed that typhoons with similar DNAs move in similar directions and show a close correlation with specific factorial components; for instance, in Taipei, rainfall DNAs of category 1 typhoons were concentrated on PCs 1, 3, 4, and 7, which were related to wind and cloud height, while those of category 2 typhoons were concentrated on PCs 1, 2, and 5, which were related to cloud-cover distribution. Moreover, in Kaohsiung, the diverse rain-making DNAs of category 1 typhoons were concentrated primarily on PCs 1 and 3 and secondarily on PCs 2 and 4, which were correlated with wind force/direction. The calibrated rain-generating simulation model illustrated that the CCs between simulated and observed rainfall among training and validation at Taipei and Kaohsiung were 0.696–0.936 and 0.876–0.950, respectively, indicating that the designed swarm response functions could effectively simulate the changing trends of rainfall for different typhoons. The identified Taipei rain-making thresholds of typhoons with a constant direction and structure demonstrated steady-state; specifically, the thresholds for MAWS, monsoon convergent maximal angle, and LCC were 7.83–10.53 m s^{-1}, $49.62°$–$53.20°$, and 7.70–9.26, respectively. Meanwhile, typhoons with changed direction and damage, which produced multi-peak rainfall hydrographs, showed unsteady thresholds; specifically, their thresholds for MAWS, monsoon convergent maximal angle, and LCC were 8.38–15.35 m s^{-1}, $48.89°$–$66.88°$, and 7.27–9.80, respectively. In contrast, 83 % of the typhoons in Kaohsiung with introduced southwest airflow showed steady but lower thresholds (4.76–8.57 m/s, $44.14°$–$58.06°$, and 5.07–9.26, respectively).

The identified causal rain-making composition showed during typhoons in Taipei (Kaohsiung), the affected degree for the monsoon convergent effect, terrain uplift effect, LCC, and wind accelerator was 12.81%–18.96 % (14.75%–20.80 %), 13.30%–22.47 % (15.77%–20.83 %), 7.23%–11.89 % (7.86%–13.21 %), and 14.05%–20.72 % (15.39%–20.20 %), respectively. The monsoon convergent effect was the largest when the typhoons crossed between west-northwest and north-northeast of Kaohsiung, and the time-varying angle between the typhoon and monsoon caused a non-uniform rain-making distribution, with LCC, TCC, LCH, and CH showing strong horizontal convection and vertical exchange. The rain-generating causal time–space evolving analysis showed that in Taipei, rains were produced when the typhoons traveled (1) between northeast and south-southeast of Taipei, where the rainy clouds carried by the wind field were transmitted along the Tamsui River valley; (2) between west-southwest and north-northwest, where the cloud cover carried by the counterclockwise cyclone was transported to the windward Taipei along the Dahan Valley; and (3) between

east-northeast and southwest, where the wind field converged with the gradient and geostrophic winds. In contrast, rains occurred in Kaohsiung when the typhoons traveled (1) between northwest and northeast, where the wind field carried cloudy rainbands along the Kaoping River Estuary; (2) between west-southwest and northeast, where the typhoon merged with the southwest monsoon to introduce rainbands; and (3) between east-southeast and southwest, where the typhoon merged with gradient and geostrophic winds or northeast airflow. MIWS and LCC showed three stochastic patterns in Kaohsiung: (1) undamaged structure when crossing the mountains continued rain-making until the storm radius left; (2) rain-making was the highest before crossing the mountains, but subsequently, structural and rain-making intensity weakened after the storm left (same as that in Taipei); and (3) rain-making only occurred at the time of landfall, because the cloud structure was damaged and intercepted by the mountains.

Future studies should use more advanced three-dimensional high-resolution cloud cover/height, wind speed/field, and other typhoon atmospheric remote sensing data in the simulation-optimization calculation to improve the accuracy of key–lock quasi-Newton multi-order computation and reduce the limitations of high-dimensional rainstorm causal decomposition.

Funding

Data availability statement

The data that has been used is confidential.

CRediT authorship contribution statement

Chien-Lin Huang: Conceptualization, Formal analysis, Investigation, Methodology, Resources, Software, Validation, Visualization, Writing – original draft, Writing – review & editing. **Nien-Sheng Hsu:** Conceptualization, Funding acquisition, Methodology, Resources, Supervision, Writing – review & editing. **Chun-Hao Yao:** Data curation, Investigation, Project administration, Resources. **Wei-Chun Lo:** Data curation, Investigation, Project administration, Resources.

Declaration of competing interest

The authors declare the following financial interests/personal relationships which may be considered as potential competing interests:Chien-Lin Huang reports financial support was provided by National Science and Technology Council, Taiwan.

Acknowledgements

Appendix A. Supplementary data

Supplementary data to this article can be found online at https://doi.org/10.1016/j.heliyon.2023.e20478.

References

[1] C.P. Chang, Y.T. Yang, H.C. Kuo, Large increasing trend of tropical cyclone rainfall in taiwan and the roles of terrain, J. Clim. 26 (12) (2013) 4138–4147.
[2] C.M. Patricola, M.F. Wehner, Anthropogenic influences on major tropical cyclone events, Nature 563 (7731) (2018) 339–+.
[3] K.S. Cheng, et al., Assessing the impact of climate change on annual typhoon rainfall-a stochastic simulation approach, Paddy Water Environ. 7 (4) (2009) 333–340.
[4] A.A. Kafy, et al., Predicting changes in land use/land cover and seasonal land surface temperature using multi-temporal landsat images in the northwest region of Bangladesh, Heliyon 7 (7) (2021).
[5] M.A. Chowdhury, et al., Climate change impacts and adaptations on health of Internally Displaced People (IDP): an exploratory study on coastal areas of Bangladesh, Heliyon 6 (9) (2020).
[6] C.C. Wu, T.S. Huang, K.H. Chou, Potential vorticity diagnosis of the key factors affecting the motion of Typhoon Sinlaku (2002), Mon. Weather Rev. 132 (8) (2004) 2084–2093.
[7] Y.L. Lin, et al., Orographic influences on rainfall and track deflection associated with the passage of a tropical cyclone, Mon. Weather Rev. 130 (12) (2002) 2929–2950.
[8] G.Y. Kim, S. Lee, Prediction of extreme wind by stochastic typhoon model considering climate change, J. Wind Eng. Ind. Aerod. 192 (2019) 17–30.
[9] D.S. Nolan, B.D. McNoldy, J. Yunge, Evaluation of the surface wind field over land in WRF simulations of hurricane wilma, Part I: Model Initialization and Simulation Validation. Monthly Weather Review 149 (3) (2005) 679–695, 2021.
[10] Y.S. Na, B. Na, S. Son, Near real-time predictions of tropical cyclone trajectory and intensity in the northwestern Pacific Ocean using echo state network, Clim. Dynam. 58 (3–4) (2022) 651–667.
[11] D.S. Nolan, et al., Evaluation of the surface wind field over land in WRF simulations of hurricane wilma, Part II: Surface Winds, Inflow Angles, and Boundary Layer Profiles. Monthly Weather Review 149 (3) (2005) 697–713, 2021.

[12] W.B. Chen, W.C. Liu, M.H. Hsu, Predicting typhoon-induced storm surge tide with a two-dimensional hydrodynamic model and artificial neural network model, Nat. Hazards Earth Syst. Sci. 12 (12) (2012) 3799–3809.

[13] Y.L. Tsai, et al., Discrepancies on storm surge predictions by parametric wind model and numerical weather prediction model in a semi-enclosed bay: case study of typhoon haiyan, Water 12 (12) (2020).

[14] S. Kim, et al., A real-time forecast model using artificial neural network for after runner storm surges on the Tottori coast, Japan, Ocean Eng. 122 (2016) 44–53.

[15] C.C. Wei, Simulation of operational typhoon rainfall nowcasting using radar reflectivity combined with meteorological data, J. Geophys. Res. Atmos. 119 (11) (2014) 6578–6595.

[16] G.F. Lin, B.C. Jhong, C.C. Chang, Development of an effective data-driven model for hourly typhoon rainfall forecasting, J. Hydrol. 495 (2013) 52–63.

[17] M.H. Yen, et al., Application of the deep learning for the prediction of rainfall in Southern Taiwan, Sci. Rep. 9 (2019).

[18] C.C. Wei, RBF neural networks combined with principal component analysis applied to quantitative precipitation forecast for a reservoir watershed during typhoon periods, J. Hydrometeorol. 13 (2) (2012) 722–734.

[19] L. Chen, et al., An improved genetic programming to SSM/I estimation typhoon precipitation over ocean, Hydrol. Process. 25 (16) (2011) 2573–2583.

[20] C.K. Yu, L.W. Cheng, Distribution and mechanisms of orographic precipitation associated with typhoon Morakot (2009), J. Atmos. Sci. 70 (9) (2013) 2894–2915.

[21] X.K. Han, et al., Temporal and Spatial Variations in Stable Isotopic Compositions of Precipitation during the Typhoon Lekima (2019), China, Science of the Total Environment, 2021, p. 762.

[22] C.S. Lee, L.R. Huang, D.Y.C. Chen, The modification of the typhoon rainfall climatology model in Taiwan, Nat. Hazards Earth Syst. Sci. 13 (1) (2013) 65–74.

[23] H. Van Nguyen, Y.L. Chen, High-resolution initialization and simulations of typhoon Morakot (2009), Mon. Weather Rev. 139 (5) (2011) 1463–1491.

[24] S. Medina, E. Sukovich, R.A. Houze, Vertical structures of precipitation in cyclones crossing the Oregon cascades, Mon. Weather Rev. 135 (10) (2007) 3565–3586.

[25] C.C. Wu, et al., Rainfall simulation associated with typhoon herb, Taiwan Part I: The topographic effect. Weather and Forecasting 17 (5) (1996) 1001–1015, 2002.

[26] Y.M. Kuo, H.J. Chu, T.Y. Pan, Temporal precipitation estimation from nearby radar reflectivity using dynamic factor analysis in the mountainous watershed - a case during Typhoon Morakot, Hydrol. Process. 28 (3) (2014) 999–1008.

[27] C.Y. Huang, I.H. Wu, L. Feng, A numerical investigation of the convective systems in the vicinity of southern Taiwan associated with Typhoon Fanapi (2010): formation mechanism of double rainfall peaks, J. Geophys. Res. Atmos. 121 (21) (2016) 12647–12676.

[28] C.C. Wang, The more rain, the better the model performs-the dependency of quantitative precipitation forecast skill on rainfall amount for typhoons in taiwan, Mon. Weather Rev. 143 (5) (2015) 1723–1748.

[29] W.M. Frank, E.A. Ritchie, Effects of environmental flow upon tropical cyclone structure, Mon. Weather Rev. 127 (9) (1999) 2044–2061.

[30] C.C. Wu, et al., Uncertainty and predictability of tropical cyclone rainfall based on ensemble simulations of typhoon Sinlaku (2008), Mon. Weather Rev. 141 (10) (2013) 3517–3538.

[31] C.C. Wang, et al., High-resolution quantitative precipitation forecasts and simulations by the cloud-resolving storm simulator (CReSS) for typhoon Morakot (2009), J. Hydrol. 506 (2013) 26–41.

[32] E. Couto, et al., Evaluation of High Rate Ponds Operational and Design Strategies for Algal Biomass Production and Domestic Wastewater Treatment, Science of the Total Environment, 2021, p. 791.

[33] E.J. Quinto, et al., Bayesian modeling of two- and three-species bacterial competition in milk, Food Res. Int. 105 (2018) 952–961.

[34] V.K. Juneja, H. Marks, H. Thippareddi, Predictive model for growth of Clostridium perfringens during cooling of cooked uncured beef, Food Microbiol. 25 (1) (2008) 42–55.

[35] M. Haouari, M. Mhiri, A particle swarm optimization approach for predicting the number of COVID-19 deaths, Sci. Rep. 11 (1) (2021).

[36] M.M. Yahaya, et al., Alternative structured spectral gradient algorithms for solving nonlinear least-squares problems, Heliyon 7 (7) (2021).

[37] J. Nocedal, S. Wright, Numerical Optimization, Springer, New York, 2006.

[38] C. Kanzow, N. Yamashita, M. Fukushima, Levenberg-Marquardt methods with strong local convergence properties for solving nonlinear equations with convex constraints, J. Comput. Appl. Math. 173 (2) (2005) 321–343.

[39] F.E. Curtis, X. Que, A quasi-Newton algorithm for nonconvex, nonsmooth optimization with global convergence guarantees, Mathematical Programming Computation 7 (4) (2015) 399–428.

[40] G. Dahlquist, Å. Björck, Numerical Methods, Dover Publications, 2003.

[41] H.L. Yu, et al., Analysis of space-time patterns of rainfall events during 1996-2008 in Yilan County (Taiwan), Stoch. Environ. Res. Risk Assess. 29 (3) (2015) 929–945.

[42] B.F. Chen, R.L. Elsberry, C.S. Lee, Origin and maintenance of the long-lasting, outer mesoscale convective system in typhoon fengshen (2008), Mon. Weather Rev. 142 (8) (2014) 2838–2859.

[43] M. Marzen, et al., Impact of severe rain storms on soil erosion: experimental evaluation of wind-driven rain and its implications for natural hazard management, Sci. Total Environ. 590 (2017) 502–513.

[44] A. Navale, C. Singh, Topographic sensitivity of WRF-simulated rainfall patterns over the North West Himalayan region, Atmos. Res. (2020) 242.

[45] Y. Zhang, et al., Mesoscale modeling study of severe convection over complex terrain, Adv. Atmos. Sci. 33 (11) (2016) 1259–1270.

[46] M.D. Fang, et al., Seasonality of diffusive exchange of polychlorinated biphenyls and hexachlorobenzene across the air-sea interface of Kaohsiung Harbor, Taiwan, Sci. Total Environ. 407 (1) (2008) 548–565.

[47] W.W.G. Yeh, Review of parameter-identification procedures in groundwater hydrology - the inverse problem, Water Resour. Res. 22 (2) (1986) 95–108.

[48] A.Y. Gunawan Rustam, M. Kresnowati, Data dimensionality reduction technique for clustering problem of metabolomics data, Heliyon 8 (6) (2022).